DOI:10.1130/B36489.1

Nick M W Roberts[ID]https://orcid.org/0000-0001-8272-5432
†thomas.lamont@bristol.ac.uk
GSA Bulletin; Month/Month 2022; v. 134; no. X/X; p. 000–000;
https://doi.org/10.1130/B36xxx.1; 14 figures; 2 tables; 4 supplemental files.
[1]Supplemental Material. Further method details and complete results for granite geochemistry, Sr-Nd isotope and U-Pb geochronology. Please visit https://doi.org/10.1130/GSAB.S.XXXX to access the supplemental material, and contact editing@geosociety.org with any questions.
SCIENCE EDITOR: MIHAI DUCEA
ASSOCIATE EDITOR: KATHRYN CUTTS
MANUSCRIPT RECEIVED 20 FEBRUARY 2022
REVISED MANUSCRIPT RECEIVED 20 JULY 2022
MANUSCRIPT ACCEPTED ___ MONTH 2022
Printed in the USA

Contemporaneous crust-derived ‘I- and S-type’ granite magmatism and normal faulting on Tinos, Delos and Naxos, Greece: constraints on Aegean orogenic collapse

Thomas N Lamont[1,2,3,†], Nick M W Roberts[4], Michael P Searle[2], Nicholas J Gardiner[1], Phillip Gopon[2,5], Yu-Te Hsieh[2], Philip Holdship[2] and Richard W White[1]
[1]*School of Earth and Environmental Sciences, University of St Andrews, St Andrews, KY169AL, UK*
[2]*Department Earth Sciences, University of Oxford, South Parks Road, Oxford OX13AN, UK*
[3]*Now at: School of Earth Sciences, Wills Memorial Building, University of Bristol, Bristol, BS81RL, UK*
[4]*Geochronology and Tracers Facility, British Geological Survey, Environmental Science Centre, Nottingham, NG12 5GG, UK*
[5]*Now at: Department of Applied Geosciences and Geophysics, Montan Universität Leoben, Peter-Tunner-Straße 5, 8700 Leoben, Austria*

ABSTRACT

Exposed on the Cycladic Islands of Greece are granitoids of varying mineralogy, including both hornblende-bearing ‘I-types’ and garnet ± muscovite-bearing ‘S-types’, suggesting heterogeneous magma sources. In this contribution, we present new field observations, major and trace element geochemistry, Sr–Nd isotopes, and U–Pb geochronology of granitoids from Tinos, Delos and Naxos that provide insight into these magma sources, along with the timing of adjacent extensional structures. I-type (biotite and hornblende-biotite) granites have initial $^{87}Sr/^{86}Sr$ = 0.70956–0.71065 and εNd(t) = −6.3 to −9.3, and S-type (garnet ± tourmaline-muscovite) leucogranites have overlapping initial εNd(t) (−7.5 to −10.1), with initial $^{87}Sr/^{86}Sr$ overlapping as well as extending to higher values (0.70621–0.73180). These isotope signatures are comparable to those of the Variscan-age Cycladic basement, but not the Hellenic arc. We suggest that both I- and S-type granites were derived via crustal anatexis of variable sources, dominantly metaigneous and metasedimentary, respectively, during the climax of Barrovian metamorphism between ca. 17–12 Ma, and critically, are not related to the Hellenic subduction zone. I-type granitoids are likely derived from dehydration melting of igneous Variscan or Cademonian aged basement protoliths, whereas S-type leucogranites formed by muscovite dehydration melting of sedimentary protoliths. Top-to-(N)NE shear zones on Naxos and Tinos were active from ca.

20–15 Ma and are folded and cut by later low and high angle normal faults. S-type leucogranites at Livada Bay, Tinos, dated at ca. 14 Ma, are cut by domino-style normal faults, placing a maximum age on the timing of extension. This is similar to ca. 15–14 Ma dates from NNE–SSW horizontally boudinaged S-type granites on Naxos. We propose that the concurrent intrusion of both I- and S-type granitoids with the onset of normal faulting, marks the transition from an overall compressional to an extensional stress field associated with orogenic collapse at ca. 15 Ma.

1. INTRODUCTION

Whether they formed via extensive crystal fractionation or via partial melting, granitic rocks provide a record of their magmatic source and the conditions of their formation (e.g., Clemens et al., 2009, Clemens, 2012); and therefore, they provide critical insight to our understanding of orogenic processes. Although there are numerous granite classification schemes, the alphabet scheme, originally limited to I- and S-types (Chappell and White, 1974), still offers some merit. The original scheme was based on the premise that I-types have (meta-)igneous source rocks, and S-types have more aluminous sources, i.e., (meta-) sedimentary rocks. Mineralogically, hornblende-bearing granitoids are typically described as I-type, and granitoids with muscovite ± aluminous phases such as garnet and cordierite are described as S-type. The role of fractionation versus partial melting in the formation of I-types, including the voluminous arc-related batholiths that are the building blocks of the continental crust, is the subject of continued debate (e.g., Ducea et al., 2015; Hämmerli et al., 2018; Clemens et al., 2020; Collins et al., 2020b; Moyen et al., 2021). The original S-type definition was based on examples from the Lachlan Orogen, SE Australia (Chappell and White, 1974, 2001; Chappell, 1984), which typically have mixed sources that include aluminous sedimentary protoliths (Keay et al., 1997; Healy et al., 2004). Type examples of pure S-type melts formed during regional Barrovian metamorphism are leucogranites from the Himalaya (Le Fort et al., 1987; Harris and Massey, 1994; Hopkinson et al., 2017).

Although some orogens show a transition of granite types during their evolution, i.e., the Lachlan I-A-S trilogy (Collins et al., 2020a), rarely in the geological record do both I- and S-type granites form in the same location at the same time. One such location where this phenomenon occurs is in the Cyclades, Greece. Here, 'I- and S-type' granites, which have been distinguished mineralogically by previous authors, intrude metamorphic core complexes adjacent to normal faults and ductile shear zones that are responsible for exhumation of rock from mid-crustal conditions. The garnet-muscovite-biotite 'S-type' leucogranites are interpreted to have been derived from partial melting of Varsican paragneiss and its metasedimentary cover at the deepest exposed levels of the Cyclades (Pe-Piper, 2000; Pe-Piper et al., 1997, 2002; Pe-Piper and Piper, 2005) however, the origin of the adjacent hornblende-biotite 'I-type' granites remains unclear.

Three end-member models have been proposed for the formation of the Cyclades 'I-type' granites: (1) they are derived from crustal melts that mixed with mantle- derived mafic magma (Altherr et al., 1982, 1988; Altherr and Siebel, 2002; Pe-Piper et al., 2002, Pe-Piper and Piper, 2005); (2) they were derived from a hydrated mantle wedge and emplaced above the retreating Hellenic subduction zone (Fytikas et al., 1984; Stouraiti et al., 2010, 2018); or (3) they are entirely crustally-derived magmas that resulted from melting an older, presumably igneous, source during high-grade metamorphism (Searle and Lamont, 2022). Previous geochronology shows that 'S-type' magmatism exposed on the Cyclades (ca. 18–13 Ma; Keay et al., 2001; Beaudoin et al., 2015; Lamont, 2018) slightly pre-dates, or is coeval with, 'I-type' granite crystallization (ca. 15–11 Ma; Brichau et al., 2007, 2008; Iglseder et al., 2009; Bolhar et al., 2010; Beaudoin et al., 2015). However, both granite types coincide with the timing of regional sillimanite-grade metamorphism and partial melting at the deepest levels of the Cyclades (ca. 20–14 Ma; Keay et al., 2001; Ring et al., 2018; Lamont et al.,

2019) and are contemporaneous with rapid cooling, normal faulting and exhumation between ca. 15–8 Ma (Hejl et al., 2002; Ring et al., 2003; Brichau et al., 2007; Seward et al., 2009; Mancktelow et al., 2016; Lamont et al., 2019).

Constraining the origin of 'I- and S-type' granites and their intimate relationship with normal faults, can therefore provide new insights into the timing of Aegean extension and deep crustal tectono-magmatic processes. In this contribution we aim to address two key questions: (1) are both 'I- and S-type' granites in the Cyclades formed from melting of different crustal source rocks at the same time? and (2) are both granite types the end product of amphibolite-granulite facies metamorphism, without the requirement of subduction and slab rollback? To answer these questions, we present new field relationships, trace element geochemistry, Sr and Nd isotopes and U–Pb zircon geochronology from granitoids on Tinos, Delos, and Naxos. Our findings lead to an improved understanding of the origin and timing of granitic magmatism, and constrain the timing of ductile shearing and normal faulting that are linked to the onset of regional Aegean extension.

2. GEOLOGICAL SETTING

The Cycladic islands in the Aegean Sea belong to the Attico-Cycladic Massif (ACM), which lies in a back arc position to the north of the NE dipping Hellenic subduction zone. The area is typically regarded a type locality of continental extension associated with metamorphic core complexes, low and high angle normal faults and 'I- and S-type' granites. However, prior to extension, the ACM comprises a series of thrust sheets that were stacked during the 'Aegean Orogeny' (Jansen and Schuiling, 1976; Papanikolaou, 1984a,b, 2013; Searle and Lamont, 2022). This mountain building event resulted in NE–SW crustal shortening and closure of an ocean (Vardar Ocean) to the NE of Tinos and Andros in present day coordinates (Lamont et al., 2019, 2020a, 2020b), followed by collision between Eurasia with Greater Adria-Apulia which was followed by subsequent post-orogenic extension. From structurally high to low these nappes include: the Upper Unit that includes the ca. 162 Ma Tsiknias Ophiolite, representing a fragment of relict ocean basin to the NE of the Cyclades (Katzir et al., 1996; Lamont et al., 2020a), underlain by a metamorphic sole that comprises mafic and pelagic lithologies representing the interface of the subducting plate (Lamont et al., 2020a; Searle and Lamont, 2022). The metamorphic sole represents the timing of intra-oceanic subduction initiation and SW-directed ophiolite obduction, constrained by U–Pb dating at ca. 74 Ma (Lamont et al., 2020a). The Upper Unit is tectonically underlain by a series of normal sensed ductile shear zones such as the North Cycladic Detachment System (Tinos, Mykonos) and the Naxos-Paros Detachment System (Naxos and Paros) (see below). The Lower Unit represents the NE-directed subducting Adriatic plate and includes the Cycladic Blueschist Unit (CBU). The CBU comprises oceanic crust and the NE leading edge of the Adria-Apulia continental margin. The CBU comprises several high-pressure (HP) tectonostratigraphic subunits that were metamorphosed at ca. 53–45 Ma (Tomaschek et al., 2003; Lagos et al., 2007; Bulle et al., 2010; Dragovic et al., 2012, 2015; Gorce et al., 2021; Tual et al., 2022; Lamont et al., in press). At structurally high levels, serpentine-bounded mélanges of eclogite and blueschist that represent the subducted oceanic crust (e.g., Kampos subunit on Syros), are underlaid by eclogite-blueschist facies rocks that represent the distal Greater Adria-Apulia continental margin, including the Chroussa and Poisanda sub-units on Syros (Keiter et al., 2011; Laurent et al., 2016) and the Kionnia sub-unit on Tinos (Bulle et al., 2010; Lamont et al., 2020b). These are underlain by blueschist-greenschist facies proximal continental margin rocks that reached lower P–T conditions including the Zas Unit in Naxos (Lamont et al., 2019; Peillod et al., 2017) and the Sostis sub-unit on Tinos (Lamont et al., 2020b). Structurally beneath the CBU on Naxos are a sequence of kyanite-sillimanite grade Barrovian metamorphic rocks that represent the proximal Mesozoic shelf carbonate cover and the underlying Variscan basement of the Adria-Apulia continental margin

(Koronos and Core Units on Naxos; Lamont et al., 2019, in press). These rocks are possibly equivalent to the Gavaro Tripolizia units on mainland Greece and experienced muscovite dehydration anatectic conditions at the deepest structural levels on Naxos at ca. 20–15 Ma (the Core Unit on Naxos; Keay et al., 2001; Lamont et al., 2019).

Several low-angle normal faults cross-cut the ACM and were responsible for large scale extension and exhumation. These include: (1) the North Cycladic Detachment System (NCDS) that crops out along the northern coastlines of Andros, Tinos and Mykonos and is associated with top-to-NE shear sense indicators (Jolivet et al., 2010). (2) The Naxos-Paros Detachment System (NPDS) that cross-cuts the kyanite and sillimanite grade metamorphic structures and earlier 'extensional' fabrics in the Naxos metamorphic core complex and has top-to-NNE kinematic indicators (Urai et al., 1990; Buick, 1991b; Cao et al., 2013; Lamont et al., 2019); (3) The West Cycladic Detachment System (WCDS) that outcrops on the islands of Serifos, Kea and Kythnos and Attica and displays top-to-SW kinematic indicators (Grasemann et al., 2012). Together these low-angle normal fault systems were active at the same time during the late Miocene-Pliocene (ca. 15–8 Ma) and caused bivergent exhumation of the ACM. Granite plutons (Fig. 1) intrude adjacent to these normal faults and are either cut by the faults or cross-cut ductile shear zones, suggesting that the location of intrusion may have been controlled by the normal faulting, or vice versa (Rabillard et al., 2018).

Although the ACM has undoubtably been extending since ca. 10 Ma, the timing of when extension commenced remains highly controversial and two competing models exist:

(1) Prolonged Aegean extension since the Eocene–Oligocene (Jolivet and Brun, 2010; Jolivet et al., 2013; 2015). This is based on: (i) the apparent episodic shift of 'I-type' magmatism southward across the Aegean throughout the Cenozoic, which is interpreted to represent migration of the volcanic arc due to slab roll-back on the Hellenic subduction zone (Le Pichon and Angelier, 1979, 1981; Fytikas et al., 1984; Lister et al., 1984; Pe-piper and Piper, 1989; Royden, 1993; Le Pichon et al., 2002; Jolivet and Brun, 2010; Jolivet et al., 2010, 2013, 2015). (ii) the presence of 'extensional' S–C' shear fabrics in exhumed blueschist-amphibolite facies metamorphic rocks within metamorphic core complexes which span the Eocene-Miocene (Lister et al., 1984; Avigad and Garfunkel, 1989; Lee and Lister, 1992; Urai et al., 1990; Buick, 1991a,b; Jolivet, 2001; Jolivet et al., 2004, 2010; Mehl et al., 2005; Jolivet and Brun, 2010). (iii) The presence of Miocene shallow marine sediments with Aquitanian to Early Burdigalian faunas (Angelier,1978; ca. 23–19 Ma) within the Upper Unit in the hangingwall of the low-angle normal faults.

(2) Aegean extension commencing at ca. 15 Ma (Lamont et al., 2019; Searle and Lamont, 2022; Kokkalas et al., 2006; Boronkay, 1995; Mastrakas and St. Seymour, 2000). This is based on: (i) the timing of a constrictional stress field recorded at the center of Naxos metamorphic core complex, (ii) The emplacement of Late Miocene granitoid plutons under a compressional to strike-slip stress regime (Mastrakas and St. Seymour, 2000; Koukouvelas and Kokkalas, 2003; Kokkalas et al., 2006; Faucher et al., 2021); (iii) the relative timing regional E–W shortening that refolded the core complex rocks and the overlying Miocene marine and continental sediments (Dermitzakis et al., 1979). (iv) the prograde clockwise P–T path of kyanite-sillimanite grade Barrovian facies metamorphic rocks from Naxos that require burial and compression that reached thermal climax at ca. 20–15 Ma. (v) After ca. 15 Ma, rocks from Naxos record exhumation and cooling associated with normal faulting on the NPDS that cross-cuts the internal metamorphic fabrics and migmatite dome (Lamont et al., 2019, in press; Searle and Lamont, 2019).

To provide further constraints on the Aegean geodynamics, in what follows we give a systematic description of new structural cross-cutting field relationships of 'I- and S-type granites', and low-angle and high-angle normal faults on the islands of Tinos, Naxos and Delos, that will be used to link the geochemistry and age of crystallization to the timing of ductile shear and brittle deformation. A summary of field relations and petrography of granitoid samples are tabulated in Table 1.

3. FIELD RELATIONSHIPS

3.1 Tinos: 'I- and S-type' Granites and the North Cycladic Detachment System

A series of granite plutons, dacite dykes and garnet-muscovite leucogranites intrude the North Cycladic Detachment System (NCDS; Jolivet et al., 2010) on Tinos that can be used to constrain the timing of deformation. The NCDS crops out along the northern coastline of Tinos and continues on Mykonos to the east (e.g., Avigad and Garfunkel, 1989, 1991; Lee and Lister, 1992; Jolivet, 2001; Jolivet et al., 2004, 2010; Mehl et al., 2005; Menant et al., 2013), and Andros to the northwest (e.g., Jolivet et al., 2010; Gerogiannis et al., 2019). The NCDS is interpreted to represent a crustal-scale low-angle normal fault that accommodated ~100 km of extension during the Miocene (Jolivet et al., 2010; Jolivet and Brun, 2010), assuming that all the exhumation was accommodated on the same structure and continues with a similar geometry at depth. The NCDS on Tinos, Andros and Mykonos comprises several shear zones and normal faults.

The Tinos Shear Zone (TSZ; referred to as the Tinos Detachment by Jolivet et al., 2010) (Fig. 2a) is interpreted as the structurally deepest component of the NCDS. It is exposed in several locations on the North Coast of Tinos and characterized by greenschist-facies top-to-NE shear fabrics that separate the Upper Unit (Tsiknias Ophiolite, and metamorphic sole) from the Lower Unit (Cycladic Blueschist Unit). The structure is folded about the NW-SE trending dome axis running down the center of Tinos (Lamont et al., 2020a,2020b) and is exposed at Kionnia peninsular on the south coast. The TSZ truncates structures within the Upper and Lower Units, suggesting that it post-dates *HP* metamorphic conditions and deformation in the CBU and metamorphic sole to the Tsiknias Ophiolite (Bröcker et al., 1993; Brichau et al., 2007; Lamont et al., 2020a,2020b). Top-to-NE shearing occurred concomitantly with greenschist-facies conditions in the Lower Unit (Cycladic Blueschists), dated at ca. 21 Ma by Rb–Sr geochronology (Bröcker and Franz, 1998; Zeffren et al., 2005) (Fig. 2). This blueschist-greenschist facies tectono-metamorphic event has not been detected in the Upper Unit (Patzak et al., 1994), which originated at much higher crustal level and has been subsequently downthrown against the Lower Unit by the TSZ (Lamont et al., 2020a,2020b).

The Tinos hornblende-biotite monzogranite pluton intrudes both the Upper and Lower Units and cross-cuts the TSZ in northern Tinos (Fig. 2) and has a U–Pb age of 14.6 ± 0.2 Ma (Brichau et al., 2007), constraining movement on the TSZ to ca. 21–14 Ma. The monzogranite is mineralogically I-type and comprises plagioclase (35%), quartz (31%), K-feldspar (17%) biotite (16%), hornblende (3%) and titanite (2%). The pluton is largely undeformed and exhibits magmatic textures (Faure et al., 1991), with a magmatic foliation defined by weakly aligned euhedral K-feldspar crystals, plagioclase, biotite, hornblende and quartz. However, near the structurally highest exposed parts of the monzogranite and along the southwestern margin, the magmatic foliation dips ~20° toward the NE. Here, a NE-stretching lineation is defined by prismatic K-feldspars, polycrystalline ribbons and elongate quartz grains which show features consistent with dynamic recrystallization and grain boundary migration (Fig. 3j; Brichau et al., 2007). In a few localities, the monzogranite displays a solid-state foliation associated with top-to-NE shear when in contact with the host Lower Unit meta-psammites (Fig. 3i) (Lamont et al., 2020b), suggesting localized top-to-NE shearing occurred during granite crystallization. Brittle deformation overprints localized ductile fabrics over a range of scales, from km-scale to micro-scale normal faults. A later generation of undeformed biotite leucogranite dykes (17TL100; N37.610512, E25.236602) intrude the pluton at Livada Bay. The dykes are 1–20 cm in diameter and intrude along an azimuth of ~95–108° (Fig. 3f) but cannot be traced into the adjacent country rock (metamorphic sole amphibolites). This observation also implies the monzogranite must have been in a solid-state at the time the leucogranite dykes intruded.

A metamorphic aureole to the Tinos monzogranite has been described by Bröcker and Franz, (1994, 2000), who noted kinked metamorphic biotite which yielded a Rb–Sr age of 10–8 Ma. In contrast, Lamont et al., (2020a), interpreted the high-grade amphibolites and pelagic metasediments in the Upper Unit (previously described as part of this metamorphic aureole), represent part the metamorphic sole structurally beneath the Tsiknias Ophiolite. The metamorphic sole has an inverted metamorphic field gradient (in contrast to the right way up gradient expected by contact metamorphism) and top-to-SW shear fabrics that formed at ca. 74 Ma (Lamont et al., 2020a). Lamont et al., 2020a suggest only a minor textural overprint is associated with the granite intrusion including diopside rims on pre-existing amphibole, and coarse-grained well-annealed amphibole-titanite microstructures that cross-cut the earlier top-to-SW obduction related shear fabrics (Lamont et al., 2020a).

Dacite dykes cross-cut the Upper and Lower Units on Tinos and occur at: (1) Kionnia Bay in south Tinos, where a dyke cross-cuts high-pressure top-to-SW fabrics associated with the Kionnia Thrust (17TL05); (2) NE of Kolimpithra Bay in North Central Tinos within the metamorphic sole amphibolites and Tsiknias Ophiolite (TLT64); and (3) across the Tsiknias sequence of alternating gabbros and peridotites on the eastern side of Mt Tsinkias in eastern Tinos, interpreted as the ophiolite Moho Transition Zone (17TL36) (Figs. 2 and 3a,b,c,h); Avigad et al., 1998, Lamont et al., 2020). The dyke mineralogy comprises plagioclase (61%), biotite (18%), and hornblende (10%), in a fine-grained groundmass with quartz (<10%) and titanite (3%) in common with 'I-type' granites. Some dykes have been classified as latites and lamprophyres (Melidonis, 1980); however, we question this interpretation based on their mineralogy, CPIW normative calculation and geochemistry discussed below. All dykes are ~10 m wide, are orientated at moderate dips and appear to emanate from the interior of the island (the center of the NW-SE trending fold axis) and have K–Ar dates of ca. 12–11 Ma (Avigad et al.,1998). Most dykes are undeformed and intrude both Upper and Lower Units, and therefore cross-cut the TSZ and post-date pervasive ductile top-to-NE shearing.

The Livada Detachment structurally overlies the TSZ and Tinos monzogranite but is poorly exposed on Tinos. It is possible that the structure cuts the Tsiknias Ophiolite and causes top-to-NE ductile shear fabrics in gabbroic mylonites (Fig. 2; Lamont et al., 2020a). On Mykonos, the Livada Detachment (Fig. 4c) truncates the roof of the 13.3 Ma Mykonos granite (Brichau et al., 2008; Jolivet et al., 2010) and juxtaposes amphibolites from the metamorphic sole of the Tsiknias Ophiolite against the granite. The Mykonos granite is affected by solid state mylonitization, suggesting shearing occurred shortly after the pluton crystallized (post-13.3 Ma; Jolivet et al., 2010; Menant et al., 2013). At Livada Bay on Tinos (Figs. 2, 3k,l,m), brittle domino-style normal faults inferred to structurally overlie and potentially root into the Livada Detachment (Fig. 2b,c) crosscut and offset metamorphic sole amphibolites and offset a series of garnet and muscovite bearing leucogranite sills by 1–10 m (Figs. 2b,c and 3k,l,m). The leucogranites occur as a branching network of sills, between 10's cm to several meters wide (Figs. 2b,c and 3k,l) and intrude parallel to the amphibolite sole obduction-related foliation (Lamont et al., 2020a). They are characterized by plagioclase (45%), quartz (35%), and K-feldspar (7%) with <300 µm diameter euhedral garnets (4%), muscovite (6%), and minor tourmaline and biotite suggesting they are mineralogically 'S-type'.

Although many garnet-muscovite leucogranite sills are truncated by the brittle NW–SE trending normal faults, some show minor curvature into alignment with the faults (Fig. 3k,l), suggesting that they had only just crystallized as faulting commenced. Within the leucogranites, a weak tectonic foliation and NE-directed lineation is expressed by stretched quartz aggregates forming polycrystalline ribbons that display undulose extinction and grain boundary migration, suggesting that NE–SW directed ductile deformation occurred immediately following granite crystallization. Garnet is mostly euhedral and shows straight faces consistent with crystallization from melt (Fig. 3m). The presence of garnet and muscovite suggests the leucogranites are mineralogically distinct from the adjacent monzogranite pluton and cross-cutting dykes. Keay (1998) reported a U–Pb zircon age of ca. 14 Ma from one of these leucogranites; however, no structural context or geochemistry was provided with this age.

The Mykonos Detachment is the structurally highest component of the NCDS. It is a brittle low-angle normal fault that overlies the Livada Detachment on Mykonos, but is not exposed on Tinos. On Mykonos, the Mykonos Detachment places silicified Miocene sediments over the metamorphic sole amphibolites with a series of brittle faults rooting into it (Fig. 4a) (Jolivet et al., 2010; Menant et al., 2013). Barite dykes and veins locally cross-cut the structure, suggesting shearing seized shortly after intrusion of the Mykonos Granite (ca. 13.3 Ma).

3.2 Naxos: 'I- and S-type' Granites, Koronos and Zas Shear Zones and the Naxos-Paros Detachment System

The island of Naxos provides the most complete cross-section through the ACM (Jansen and Schuiling, 1976) and has previously been regarded as a metamorphic core complex, interpreted to have formed during regional Aegean extension (Lister et al. 1984; Buick, 1991a,b; Urai et al., 1990; Vanderhaeghe, 2004; Jolivet et al., 2010; Kruckenberg et al., 2011; Ring et al., 2010, 2018). The large-scale structure of the island indeed comprises a high-grade metamorphic footwall, separated from a relatively un-metamorphosed and ophiolitic hanging-wall by a low-angle brittle-ductile normal fault, associated with crustal extension (The Naxos-Paros Detachment System; NPDS; Cao et al., 2013, 2017; Lamont et al., 2019). However, within the metamorphic footwall, rocks of contrasting tectono-thermal histories are juxtaposed against each other, preserving an extremely condensed series of right way-up metamorphic isograds (Lamont et al., 2019; in press). Structurally high levels of the metamorphic footwall reflect an early subduction stage associated with blueschist facies metamorphism of the CBU at ca. 50–38 Ma (Wijbrans and McDougall, 1988; Peillod et al., 2017; Lamont et al., in press). These are structurally underlaid by kyanite-sillimanite grade Barrovian facies rocks that reached muscovite dehydration anatectic conditions in the structurally deepest rocks at ca. 20–15 Ma (Keay et al., 2001; Ring et al., 2018) producing migmatites and leucogranites, and the formation of a migmatite dome and subdomes (Vanderhaeghe, 2004; Kruckenberg et al., 2011; Lamont et al., 2019). The cause of Barrovian metamorphism remains controversial. The classic interpretation involves isobaric heating during regional Aegean extension (Lister et al., 1984; Buick and Holland, 1989; Peillod et al., 2021). However, garnet in kyanite-grade gneisses and migmatites has been shown to grow with increasing pressure and temperature, in a clockwise, prograde P–T–t path from ca. 6 kbar and 550 °C to ca. 10–11 kbar and 670–730 °C, suggesting heating occurred during burial and compression (Lamont et al., 2019, in press).

Within the metamorphic footwall, two major top-to-NNE shear zones are responsible for the juxtaposition of different tectono-stratigraphic units that experienced different tectono-thermal histories. (1) The Zas Shear Zone (ZSZ) places the Zas Unit (retrogressed high-pressure rocks of the Cycladic Blueschist Unit) in the hanging-wall against the Koronos Unit (kyanite-grade Barrovian metamorphic rocks) in the footwall. (2) The Koronos Shear Zone (KSZ) accommodated shearing at >600 °C, marked by dynamic recrystallization via grain boundary migration of quartz and kyanite-sillimanite-grade microstructures, and places the Koronos Unit in the hangingwall against the Core Unit migmatites in the footwall (Lamont et a., 2019). The KSZ and ZSZ are both purely ductile features associated with pure shear flattening of right way-up metamorphic isograds and are concordant to the island scale foliation (Fig. 5), but are cut by the overlying NPDS (Lamont et al., 2019). The structural discordance between these internal structures (ZSZ and KSZ) and the overlying brittle-ductile NPDS suggests the KSZ and ZSZ pre-date movement on the NPDS (Lamont et al., 2019). The KSZ and ZSZ are folded around the migmatite dome suggesting they pre-date migmatite doming, E–W shortening and constrictional stress conditions (Lamont et al., 2019).

Garnet-biotite and garnet-tourmaline leucogranite dykes and sills that we refer to as 'S-types' intrude the migmatite dome (Core Unit; Lamont et al., 2019) and emanate into the overlying Koronos and Zas Units clearly cutting the KSZ (Figs. 5 and 6), particularly on the eastern margin of the migmatite dome. In contrast the leucogranites that reach higher structural levels in Western Naxos are affected by solid state recrystallization and are rotated and transposed into alignment with the overlying NPDS (Fig. 6a,c). Many of the leucogranites appear to emanate from regions of fertile lithologies (now stromatic migmatites and in places diatexite migmatites), however some others cross-cut low melt fraction domains. Existing geochemical studies suggest that the leucogranites are probably derived from remobilized Varsican Basement orthogneiss and paragneiss during the sillimanite grade thermal climax (Pe-Piper, 2000).

Within the core high strain zone (CHSZ) at the center of the migmatite dome (Figs. 6b,e), NNE–SSW and E–W trending upright isoclinal folds and leucogranite intrusions (TLN8) are affected by vertical boudinage associated with horizontal constrictional stresses. Rocks at higher structural levels are also refolded creating NNE–SSW trending upright folds, due to E-W shortening (Buick, 1991b, Urai et al., 1990; Lamont et al., 2019). Outcrop observations suggest constrictional stresses were followed by horizontal NNE–SSW extensional stresses associated horizontal NNE-SSW boudinage of the leucogranites (TLN10) (Lamont et al., 2019). The timing of leucogranite crystallization therefore places constraints on the timing of the Koronos and Zas shear zones and NPDS, and maximum ages of constrictional and extensional stress regimes. Zircon was dated in one sample of orthogneiss (TL57), thought to represent the basement to the island, and in seven samples of leucogranite intrusions (TL58, TL63, TL69, TL72, TLN8, TLN10).

The Naxos-Paros Detachment System (NPDS) is a brittle-ductile low-angle normal fault, that accommodated exhumation of Naxos during regional extension (Buick, 1991b; Urai et al., 1990). This low-angle normal fault truncates all compressional structures and peak metamorphic fabrics and the Koronos and Zas shear zones within the core complex (Fig. 5) and is gently folded along an NNE–SSW axis. The structure may bound the entire island if the outcrop at Moutsouna Peninsular on the east coast represents the same structure. The brittle fault (Moutsouna Detachment; Cao et al., 2013, 2017) is best exposed in NW and central Naxos (near the villages of Melanes and Galanado; Fig. 5) and on the eastern coastline at Moutsouna peninsular (Fig. 5). An 'I-type' hornblende-biotite granodiorite pluton dated at ca. 12.2 Ma (Keay, et al., 2001), intrudes the metamorphic sequence on the western side of the island associated with a ~300 m wide contact metamorphic aureole (Jansen, 1973), but in the north is cut by the NPDS, suggesting that the NPDS was active shortly after granodiorite crystallization (Lamont et al., 2019; Koukouvelas and Kokkalas, 2003). The granodiorite is mineralogically different from the migmatized Variscan orthogneiss basement exposed in the Koronos and Core Units (Fig. 5). On its eastern margin close to the NPDS, the granodiorite is mylonitized and affected by pseudotachylytes (Koukouvelas and Kokkalas, 2003; Lamont et al., 2019). Here, a steep easterly dipping N–S trending foliation overprints some of the more shallowly dipping mylonite fabrics and has been interpreted as a dextral NNE–SSW trending strike-slip fault (Koukouvelas and Kokkalas, 2003) and is associated with aplite dykes.

High-angle faults throughout the hangingwall of the NPDS root into a 20 m thick cataclasite and fault breccia zone defining the brittle detachment surface, which is structurally underlain by a ~500 m thick zone of ductile mylonites. On the west side of Naxos, brittle deformed cataclasites and sediments are juxtaposed against upper amphibolite-grade migmatites, producing an 'apparent' metamorphic field gradient of ca. 700 ˚C/km (Lamont et al., 2019). Although S–C' fabrics affect all structural levels of Naxos, the intensity of shearing increases upwards toward the NPDS. Quartz microstructures indicate dynamic recrystallization was followed by brittle deformation at temperatures <500 °C (Lamont et al., 2019). On the western side of Naxos, the NPDS steeply dips to the WNW away from the core complex at ca. 40–50˚ perpendicular to the NNE-trending shallowly (~10°) plunging lineation.

In central Naxos, between the villages of Galando and Kato Potamia/ Melanes the NPDS is folded into a gently north-plunging synform (Fig. 5), exposing the Upper Unit in a graben that is bounded by steep cross-cutting E–W trending normal and NE–SW and NW–SE trending oblique slip/strike slip faults (Fig. 5; Koukouvelas and Kokkalas, 2003), potentially associated with a transitional stress regime prior to the onset of regional extension (Kokkalas et al., 2006). The island scale doming of Naxos also affects the Pliocene-Pleistocene sedimentary successions within the hanging wall of the NPDS. It has also been argued a relatively recent component of E–W shortening is required during and after the NPDS was active to explain the ~30° westward dip of bedding away from the core complex and the steep folding of the detachment (Fig. 5 Lamont et al., 2019; Searle and Lamont, 2022). This E–W shortening was also responsible for gently folding the isograds and the development of minor N–S trending brittle thrust faults and is required to explain the upright N–S trending folds within the core complex (Fig. 5; Lamont et al., 2019; Virgo et al., 2018; Von Hagke et al., 2018).

3.3 Delos Biotite-Tourmaline Leucogranites

Delos Island also exposes some of the deepest structural levels of the ACM that experienced anatectic conditions. Biotite-tourmaline and two-mica leucogranite sills intrude along a gently dipp top-to-NE shear foliation in sillimanite-grade gneisses and migmatites. These metamorphic rocks are also intruded by an hornblende–biotite 'I-type' pluton (Mykonos monzogranite) dated at ca. 13.3 Ma (Brichau et al., 2008) (Fig. 4b,d). Delos leucogranites appear similar to the Naxos leucogranites (see below), as they appear to emanate from locally high-melt fraction migmatite (Jolivet et al., 2021; Lamont et al., 2019). There are no reported U–Pb ages from Delos leucogranites, but their age would place constraints on the timing of peak sillimanite-grade metamorphism and anatexis during deep crustal top-to-NE shearing.

4. ANALYTICAL METHODS

4.1 Whole Rock Geochemistry

Major elements were analyzed by X-ray Fluorescence (XRF) at the Department of Earth and Environment, Franklin and Marshall College, Pennsylvania, USA. Trace elements were measured using a PerkinElmer NexION 350D inductively coupled plasma mass spectrometer (ICP-MS) at the Department of Earth Sciences, University of Oxford. The full procedures are described in the supplementary material. Reported precision is less than ± 1% for major elements and ± 5% (2.S.D.) for trace elements. The results are presented in the supplementary files and combined with literature data Stouraiti et al., (2010, 2018), Altherr and Siebel, (2002), Pe-Piper, (2000); Pe-Piper and Piper (2005).

4.2 U–Pb Geochronology

U–Pb zircon geochronology was carried out at the Geochronology and Tracers Facility at the British Geological Survey (Nottingham, UK), following the method of Roberts et al. (2016). Analyses were performed on a Nu Attom single-collector ICP-MS coupled to a New Wave Research 193UC excimer laser ablation system fitted with a TV2 cell. All data and ages are shown and quoted at 2σ, include propagation of systematic uncertainties, and are common-lead corrected $^{206}Pb/^{238}U$ ages using a ^{207}Pb-based correction with Stacey and Kramers (1975) inferred initial lead compositions and assumed concordance (e.g., Chew et al., 2011), unless stated otherwise. Many samples exhibit a range of ages that are outside of uncertainty of a single population, which is common for crustal-derived granites due to the common occurrence of protracted melting and inclusion of antecrysts and xenocrysts (e.g., Lederer et al., 2013); therefore, outlying data from the main population are rejected from the weighted mean common-Pb corrected ages. We note that this approach is subjective; however, the timing of the youngest dates will generally provide the crystallization age (excluding lead-loss), and the crystallization age is the most useful for understanding cross-cutting field-relationships. Data are plotted and ages calculated using a combination of Isoplot v3 (Ludwig, 2011) and IsoplotR (Vermeesch, 2018), and are summarized in Table 2 and tabulated in the supplementary files.

4.3 Sr and Nd Isotope Geochemistry

Sr and Nd isotopic data were collected in the Department of Earth Sciences, University of Oxford, using a Nu Plasma multi-collector inductively plasma spectrometer (MC-ICP-MS). Detailed sample handling and preparation procedures are described in the supplementary material. The data are combined with granite and basement data from Stouraiti et al. (2010, 2018), Pe-Piper (2000), Pe-Piper et al., (1997), Altherr and Siebel., (2002), Pe-Piper and Piper (2005), McGrath et al., (2017), Briqueu et al., (1986), Bolhar et al., (2017) and Soder et al. (2016). Initial Sr and Nd isotope ratios for our new samples were calculated using the U–Pb magmatic ages calculated here and decay constants of $1.393*10e^{-11}$ for ^{87}Sr and $6.524*10e^{-12}$ for ^{147}Sm (Villa et al., 2020). Initial Nd isotope values are quoted as εNd(t) using the CHUR values of Bouvier et al. (2008). Two-stage Nd model ages were calculated using $^{147}Sm/^{144}Nd$ of 0.09, that of average continental crust (Taylor and McLennan, 1985), and a depleted mantle with a modern-day $^{143}Nd/^{144}Nd$ of 0.51315 and $^{147}Sm/^{144}Nd$ of 0.2135 (Pearson et al. 1995). The results are summarized in Table 2 and tabulated in the supplementary files.

5. RESULTS

We define our samples a I-type and S-type based on mineralogy, with biotite and hornblende-biotite granitoids as I-type, and garnet ± tourmaline ± muscovite-biotite granitoids as S-type.

5.1 Whole Rock Geochemistry

Both ‘I- and S-type’ granitoids display some degree of overlap on simple granite classification diagrams. On the CIPW normative Quartz-Plagioclase-K-Feldspar (QAPF) classification diagram (Fig. 7a), ’I-type’ granitoids span the monzogranite, granodiorite to quartz-monzodiorite fields, whereas ‘S-types’ plot within the monzogranite, granodiorite and tonalite fields. On the aluminum saturation index (ASI) [Al/(Ca-1.67P+Na+K)] vs A/NK [Al_2O_3/ (Na_2O+K_2O)] diagram (Fig. 7b), ‘I-type’ granites plot in the peraluminous field (ASI = 1.09–1.16, A/NK = 1.19–1.83), whereas ‘S-type’ granites show a smaller range in ASI (1.09–1.44) and a smaller range in A/NK (1.14–1.69) and are also entirely peraluminous. On the modified alkali lime index (MALI) [Na_2O+K_2O-CaO] vs SiO_2 diagram (Fig. 7c), ‘I-type’ granites have lower MALI and SiO_2 values than ‘S-type’ granites and plot as more calc-alkali to calcic. On the Fe-number [FeO^T/ (FeO^T + MgO)] vs SiO_2 diagram (Fig. 7d), the ‘I-type’ granites are mainly magnesian, whereas ‘S-type’ granites show a range from 0.64 to 0.90 and are mostly Ferroan. On the K_2O vs Na_2O diagram (Fig. 7e), the ‘I-type’ granites span the I-/ S-type divide, whereas petrologically ‘S-type’ granites plot solely within the I-type field as they have lower K_2O. ‘S-type’ granites are low to medium K, whereas ‘I-types’ are medium to high K. In the Rb/Ba vs Rb/Sr diagram of (Sylvester, 1998; Fig. 7 g) the two granite types form distinct populations, with ‘I-type’ granitoids having Rb/Sr ratios between 0.2 and 8.0 and Rb/Ba between 0.1 and 2.0, which overlaps with the calculated greywacke derived melt via biotite dehydration melting (Sylvester, 1998) and straddles the clay-poor to clay rich source divide. In contrast, ‘S-type’ granites have higher Rb/Sr ratios (8–120) and higher Rb/Ba ratios (3–100) indicative of a clay rich source. On the CaO/Na_2O vs Al_2O_3/TiO_2 diagram (Fig. 7h), which can be used to discriminate between pelite derived, psammite derived and basalt derived melts, ‘I-type’ granitoids have CaO/Na_2O ratios generally higher than ‘S-type’ granites (0.3–2.0 vs 0.1–0.7 respectively) and lower Al_2O_3/TiO_2 ratios (15–100 vs 70–2000 respectively). Jung and Pfänder, (2007) suggested that CaO/Na_2O ratios distinguish between pelite-derived melts (CaO/Na_2O <0.5) and melts derived from greywackes or igneous sources (CaO/Na_2O: 0.3–1.5), whereas Al_2O_3/TiO_2 ratios reflect the melting temperature. This suggests that ‘S-type’ granites are derived from a pelitic source, and ‘I-type’ granites are derived from a mafic-greywacke source. However, the ‘I-type’ granites also overlap with Cycladic basement values and are projected to be >50% pelite derived melt on the calculated pelite-basalt derived melt mixing line of Patiño Douce and Harris (1998).

Maficity (Molar Fe+Mg) versus oxide weight % plots (Fig. 8a-i) show that ‘I- and S-type’ granitoids form distinct populations and do not fit on the same fractionation trends. ‘I-type’ granitoids follow similar major element trends consistent with fractional crystallization of a similar parent magma and are characterized by slightly lower SiO_2 (60%–71%), higher TiO_2 (0.2%–1.0%), similar Al_2O_3 (14.0%–16.2%), variable $Fe_2O_3^T$ (0.8%–5.3%), negligible MnO (<0.1%), moderate Na_2O (2.5%–3.8%) and K_2O (2.5%–5.7%), and moderate P_2O_5 (0.05%–0.20%). In contrast, ‘S-type’ granites are characterized by higher SiO_2 (73%–76%), negligible TiO_2 (<0.1%) slightly lower Al_2O_3 (13.5%–16%) low $Fe_2O_3^T$ (0.2%–1%), variable MnO (0.03%–0.2%) low CaO (0.2%–1.1%) low MgO (<0.3%), and importantly moderate to high Na_2O (3.5%–5.8%) and highly variable K_2O (0.3%–5.0%) and low P_2O_5, suggesting they cannot be explained by fractional crystallization of the same parent magma as the ‘I-type’ granites.

‘Spider diagrams’ with trace elements arranged in order of compatibility (Fig. 9a-b), reveal complex patterns. ‘I-type’ exhibit similar convex-down patterns with increasing incompatibility relative to primitive mantle and chondrite (Sun and McDonough, 1989), with the exception of Zr and Hf, possibly due to crystallization of zircon. The ‘S-type’ leucogranites show lower concentrations in Ba, La, Ce, Pr, Sr and Eu (Fig. 9c), and higher concentrations in Ta, Nb and other high field strength elements (HFSE’s). The cross-cutting leucogranite dyke on Tinos (17TL100) is more enriched in all elements except P. The ‘I-types’ also show variable Nb depletion relative to Th, whereas the ‘S-types’ and cross-cutting dykes show little Nb depletion. Sample 17TL95 from Delos and sample 17TL106 from Naxos, display an intermediate trace element pattern lying between the signatures of the ‘S-type and I-type’ magmas. Incompatible heavy rare earth element (HREE) patterns (Fig. 8) reveal two distinct trends: (1) The ‘I-type’ granitoids show convex-down patterns relative to chondrite (Sun and McDonough, 1989), whereas (2) the ‘S-type’ leucogranites show convex-up patterns with significant depletion in Eu. Further granite discrimination diagrams and Harker diagrams are presented in the supplementary material.

5.2 U–Pb Geochronology

5.2.1 Tinos ‘I-Type’ Dacite Dykes

TLT64 is taken from a partially deformed dacite dyke that intrudes amphibolites of the metamorphic sole in the Upper Unit to the NE of Kolimpithra Bay and dips toward the southeast. TLT64 zircons are euhedral and interpreted to have a magmatic origin. Ablation of zircon rims constrains dyke emplacement and yields a weighted mean common-Pb corrected age of 14.65 ± 0.29 Ma and an MSWD of 1.7, with the data lying between 14.2 ± 0.4 Ma and 15.0 ± 0.5 Ma (Fig. 10a). This date is interpreted to give a lower age bracket for movement on the TSZ, as the dyke intrudes across it. However, because the dyke is affected by partial solid-state recrystallization of plagioclase and quartz, it suggests some localized ductile deformation was still occurring at this structural level of the Upper Unit. Ablation of zircon cores gives a consistent inheritance age of ca. 185 Ma (Fig. 10b), which is the same age as the protolith to the amphibolites of the metamorphic sole under the Tsiknias Ophiolite. This indicates incorporation of some country rock during dyke emplacement.

17TL36 is coarse-grained undeformed dacite dyke intrudes through the Moho Transition Zone sequence of alternating serpentinites and gabbros of the Tsiknias Ophiolite on the eastern flank of Mt Tsiknias. 17TL36 zircons are euhedral and core and rim common-Pb corrected dates of 14 data points span between 13.9 ± 0.5 Ma and 14.9 ± 0.5 Ma, with a weighted mean of 14.5 ± 0.3 Ma and an MSWD of 2.0 (Fig. 10a), which is interpreted to represent the timing of dyke emplacement. Because this dyke is completely undeformed, this date provides a minimum age for ductile deformation along the TSZ.

17TL05 is from a more evolved dyke that intrudes eclogite and blueschist facies rocks of the Kionnia Thrust (in the Lower Unit; Lamont et al., 2020b) at Kionnia Bay (N37.553558, E25.134661). The dyke dips moderately toward the NE and cross-cuts blueschist-facies thrust related top-to-SW fabrics, and retrograde greenschist facies top-to-NE fabrics (Lamont, 2018; Lamont et al., 2020b). 17TL05 Zircons are euhedral and common-Pb corrected U-Pb spot dates range between 14.0 ± 0.3 Ma and 15.4 ± 0.5 Ma, with 13 of 15 analyses yielding a weighted mean date of 14.4 ± 0.2 Ma with a MSWD of 1.0 (Fig. 10a). Two zircon cores give inheritance ages of ca. 167 Ma and 265 Ma, the first of which is similar to the protolith age of the Cycladic Blueschist metasediments, and the older age is similar to an inheritance age also recorded in basement rocks on Naxos (Fig. 10b).

5.2.2 Tinos 'I-Type' Monzogranite Pluton

TLTN36 is from the undeformed center of the monzongranite and shows no preferred alignment of hornblende and biotite, K-feldspar and plagioclase phenocrysts suggesting it postdates shearing on the TSZ. TLTN36 zircons are euhedral and interpreted as having a magmatic origin. Ablation of zircon cores and rims gives a range of ages between 15.8 ± 0.7 Ma and 13.6 ± 0.6 Ma; however, because zircon growth can occur over a prolonged period in the magmatic system prior to granite crystallization, an older group of dates were omitted from the population used to calculate the weighted mean. The remaining 18/25 spots were used to calculate a weighted mean of 14.2 ± 0.3 Ma with a MSWD of 1.4. This date is interpreted to constrain pluton emplacement that must cross-cut the TSZ with no subsequent deformation.

TLTN34 was taken from the southwestern margin of the monzogranite pluton and is highly foliated, with a shallowly NE-plunging lineation of plagioclase and quartz that form stretching fabrics toward the NE suggesting it crystallized synchronous with top-to-NE shearing on the TSZ. TLTN34 zircon crystals show magmatic textures (supplementary material). Ablation of both cores and rims yielded a spectrum of common-Pb corrected ages between 14.1 ± 0.7 and 15.8 ± 0.6 Ma. After removal of the older outlying datapoint, 31 of 32 analyses yields a weighted mean date of 14.8 ± 0.3 with an MSWD of 1.2. This date is marginally older than those of the undeformed granite (TLTN36) and dacite dykes. It possibly suggests the monzogranite may have firstly intruded from its southwestern margin coeval with top-to-NE shearing although the errors on this age substantially overlap.

TLT13 is a few centimeter-wide hornblende-biotite granite vein that intrudes into meta-cherts from the Mirsini Unit in the Upper Unit, likely related to the monzogranite a few hundred meters away. TLT13 zircon crystals are magmatic, and ablation of cores and rims give dates between 13.9 ± 0.4 Ma and 16.3 ± 0.7 Ma. A weighted mean common-Pb corrected date of 14.3 ± 0.3 with an MSWD of 1.8 is based on 15/16 analyses. This date is almost identical to that of sample TLTN36 (undeformed monzogranite), and thus constrains the latter stages of pluton emplacement. Inherited ages of ca. 233 and 1105 Ma were obtained. The youngest of these ages is similar to that reported in sample 17TL05, possibly representing inheritance from Cycladic basement rocks (Fig. 10b).

5.2.3 Tinos 'S-Type' Leucogranites

TLTN13 is from a garnet-muscovite leucogranite sill that intrudes parallel to the amphibolite country rock obduction related foliation, and is cross-cut by brittle high angle normal faults. TLTN13 Zircon shows complicated morphologies and therefore only zircon rims were analyzed to constrain the emplacement age of the sill. Common-Pb corrected spot dates range from 14.0 ± 0.4 Ma to 16.0 ± 0.4 Ma. The youngest of these dates constrains the timing of sill crystallization and therefore provides a maximum age for the timing of brittle normal faulting at Livada Bay (ca. 14 Ma).

TLTN15 is from an adjacent leucogranite sill that displays minor curvature into alignment with some of the normal faults (Fig. 3k,l), suggesting it crystallized shortly prior to normal faulting. TLTN15 zircons display complicated morphologies. Extraction of zircon rim data yield three common-Pb corrected dates between 13.9 ± 0.5 and 14.7 ± 0.3 Ma, with a weighted mean of 14.2 ± 0.9 Ma with a MSWD of 1.6 (Fig. 10a). This date constrains the onset of brittle normal faulting, although it has a larger uncertainty owing to fewer data points. Two zircon cores give inherited ages of ca. 174 Ma and 845 Ma; the youngest of these presumably represents the protolith age of the sole amphibolites (Lamont et al., 2020a), suggesting some incorporation of the host amphibolites during intrusion.

5.2.4 Tinos Cross-Cutting Leucogranite Dykes

17TL100 is from a biotite leucogranite vein swarm ~2–10 cm wide that intrudes the eastern margin of Tinos monzogranite pluton at Livada Beach which cross-cut the TSZ. The dykes strike ~109° and orientated subvertical and clearly intruded once the pluton was solid-state and cross-cut top-to-NE shear fabrics. 17TL100 zircons exhibit magmatic crystal habits and common-Pb corrected U–Pb dates of cores and rims range between 13.8 ± 0.5 Ma and 16.8 ± 0.7 Ma. A weighted mean date of 14.3 ± 0.1 Ma with an MSWD of 0.89 (Fig. 10a) is obtained from 17/18 analyses. The age of sample 17TL100 is within uncertainty of the undeformed monzogranite sample TLTN36, and therefore monzogranite pluton crystallization must have occurred between ca. 14.4 and 14.3 Ma, and the cross-cutting dyke must have intruded immediately after.

5.2.5 Delos Leucogranite

17TL95 biotite-tourmaline leucogranite sill intrudes parallel to the sillimanite-grade gneissic foliation on the eastern coast of Delos. The sill and the surrounding rocks locally exhibit complex relationships with hornblende-biotite granitoids that cross-cut the gneissic foliation and the leucogranites (Fig. 4b). 17TL95 zircon rims yielded two distinct age populations. An older population yielded a weighted mean common-Pb corrected age of 13.8 ± 0.2 Ma with an MSWD of 0.90, whereas a younger age population gave a weighted mean age 12.1 ± 0.2 Ma with an MSWD of 0.33. This bimodal age distribution is interpreted as two distinct periods of zircon rim growth. Based on field relationships, the older age must represent partial melting of the host sillimanite-grade gneisses, whereas the younger ca. 12 Ma presumably represents the intrusion of the adjacent 'I-type' hornblende-biotite granites and possibly remobilization and incorporation of the later magma (that could potentially be interpreted from the geochemistry). The hornblende-biotite granites are likely related to the adjacent Mykonos monzogranite which has a U–Pb age of ca. 13.3 Ma (~1 Myr older) suggesting 'I-type' magmatism occurred over >1 Myrs.

5.2.6 Naxos Aplite within Granodiorite

17TL106 is from an uprightly folded aplite within the interior of the Naxos I-type granodiorite (Fig. 6d). The sill is folded about a NE–SW trending axis with the host granodiorite. 17TL106 zircons display euhedral growth zoning, and ablation of rims yields common-Pb corrected data between 14.6 ± 0.4 Ma and 15.3 ± 0.5 Ma, and yields a weighted mean age of 14.8 ± 0.2 Ma with an MSWD of 1.19 (Fig. 10a). This age pre-dates the reported U–Pb age of the host granodiorite by ca. 2.5 Ma (12.2 Ma; Keay et al., 2001). The aplite therefore cannot represent a late stage fractionate melt of the granodiorite. Alternatively, it could represent an enclave or xenolith of an earlier melt derived from the adjacent metamorphic core complex, that was incorporated into the granodiorite during emplacement. With this latter explanation, the folding could be a result of either magmatic flow during granodiorite emplacement or from regional E–W shortening.

5.2.7 Naxos 'S-Type' Leucogranites

Zircon was dated in one sample of orthogneiss (TL57), thought to be the basement to the island, and in seven samples of leucogranite intrusions (TL58, TL63, TL69, TL72, TLN8, TLN10). The orthogneiss yielded significant zircon inheritance, with three highly discordant ages pointing to Proterozoic ages, a population of six analyses at ca. 600–550 Ma, and a population of seven ages at ca. 330–300 Ma. Two younger discordant points are probably mixed ages, and two sub-concordant (<15% discordance) young overlapping ages of 17.0 ± 0.8 and 16.8 ± 0.7 Ma.

Six leucogranite intrusions were dated, primarily with the aim of providing age constraints on cross-cutting relationships. Of these, four were dominated by zircon inheritance (Fig. 10a and supplementary material) and two yielded substantial populations of young ages associated with crystallization. Inheritance is dominated by populations at ca. 600 and 300 Ma, similar to the basement orthogneiss, but also features discordant ages up to 2873 Ma ($^{207}Pb/^{206}Pb$ ages). The range of Oligocene-Miocene dates in these samples ranges from ca. 19–13 Ma, and dates falling in between this age range and ca. 300 Ma probably reflect mixing between inherited cores and younger overgrowths (Fig. 10a-b). Estimates of crystallization age, based on the youngest zircon or group of zircon dates, are as follows:

TL58 is a garnet-biotite leucogranite dyke that clearly cross-cuts the kyanite-sillimanite top-to-NNE shar fabrics on the KSZ on the eastern side of the migmatite dome. The leucogranite can clearly be traced from the structurally deeper migmatites, and into the overlying Koronos Unit. TL58 zircon gives an age of 13.1 ± 0.3 Ma (weighted average with n = 3). Because the leucogranite cross cuts the KSZ and top-to-NNE kyanite grade shear fabrics, the age of granite crystallization therefore constrains final movement on the KSZ.

TL63 is a garnet-tourmaline leucogranite dyke that intrudes parallel to the steep westerly dipping foliation on the western margin of the migmatite dome associated with the NPDS, near the village of Kourachari. TL63 zircon provides a single date of 13.2 ± 0.5 Ma. Because the dyke locally cross cuts the KSZ metamorphic foliation in the country rock, but is affected by post-crystallization deformation along strike, the age brackets the ending of shearing on the KSZ but is synchronous with top-to-NNE shearing on the NPDS.

TL69 is a biotite-muscovite leucogranite from the western margin of the migmatite dome that is aligned parallel to the metamorphic foliation associated with the KSZ. Zircons give a single date of 17.6 ± 0.6 Ma, which constrains the timing of movement on the KSZ as the dyke is aligned parallel to the KSZ metamorphic top-to-NNE foliation.

TL72 is a deformed garnet-tourmaline leucogranite sill that intrudes metasediments and a thin slither of serpentinized periodite on the NW flank of the migmatite dome gives a single date of 12.7 ± 0.8 Ma. The granite intrudes from the migmatites through the KSZ into the overlying NPDS ductile shear zone on the western margin of the migmatite dome and has been boudinaged by strong top-to-NNE shearing associated NPDS. Because this dyke cuts the KSZ but is boundinaged and rotated into alignment with the NPDS, the age post-dates shearing on the KSZ, but places an upper bound for shearing on the NPDS.

TLN8 is a vertically orientated and boudinaged biotite-muscovite leucogranite dyke that intrudes marble in the CHSZ and yields an age of 14.4 ± 0.2 Ma (weighted average with n = 2). The boudinage appears to be syn granite crystallization, due to lobate margins on the granite. Because this dyke is vertically orientated and vertically boudinaged, the age constrains the timing of the horizonal constrictional stress field at the center of the migmatite dome, associated with a vertical extension direction (σ_3).

TLN10 garnet-biotite leucogranite dyke intrudes marble in the CHSZ at the center of the Naxos migmatite dome and is boudinaged along a NNE-SSW azimuth that appears to have occurred under solid state conditions. It yields a crystallization age of 13.3 ± 0.3 Ma (weighted average with n = 2), which serves as an upper bound for the timing NNE-SSW extension.

5.3 Sr and Nd Isotope Geochemistry

The new Sr and Nd isotope data is plotted in figure 11 alongside existing literature data from intrusive rocks, basement lithologies and volcanic rocks from recent Hellenic arc. ‘I-type’ intrusions on Tinos, Delos and Naxos show a narrow range of initial $^{87}Sr/^{86}Sr$ ratios from 0.70956 to 0.71065, and a range in εNd(t) of −6.5 to −8.1. The dacite dykes on Tinos have initial $^{87}Sr/^{86}Sr$ ratios of 0.70956–0.70178 and similar εNd(t) values of −6.5 to −8.1. ‘S-type’ granites display higher initial $^{87}Sr/^{86}Sr$ ratios, although with significant heterogeneity compared to the ‘I-type’ intrusions. On Tinos, garnet-muscovite leucogranites have initial $^{87}Sr/^{86}Sr$ ratios ranging from 0.70621 (TLTN15) to 0.71692 (TLTN13). On Naxos, the range in initial $^{87}Sr/^{86}Sr$ ratios is even greater varying from 0.71049 to a high initial $^{87}Sr/^{86}Sr$ ratio of 0.73180, with this latter value comparable to literature sample PA15 from the Paros basement (0.7622; Stouraiti et al., 2010). εNd(t) for the ‘S-type’ granites range from −6.8 to −9.6 on Naxos, and from −5.5 to −5.7 on Tinos and −9.3 on Delos. Metasedimentary (gneiss and schists) country rocks from Paros basement (Stouraiti et al., 2010; McGrath et al., 2017) have initial $^{87}Sr/^{86}Sr$ ratios ranging from 0.71498 to 0.72387 and εNd(t) of −8.4 to −9.6, whereas Variscan (Hercynian) basement on Naxos has initial $^{87}Sr/^{86}Sr$ ratios of ~0.7170 and εNd(t) of −5.3 to −7.4 (Pe-Piper, 2000). Contrastingly, the Paros (Kolombithres) biotite–granite (S-type), shows distinctly less radiogenic initial $^{87}Sr/^{86}Sr$ (0.71152–0.71184) that is similar to the ‘I-type’ granitoid population on Tinos, Mykonos, Naxos and Serifos. Amphibolites in the basement yield initial $^{87}Sr/^{86}Sr$ ratios of 0.7050–0.7100 and εNd(t) of 2.2 to −4.3 (Bolhar et al., 2017).

Two-stage Sm–Nd model ages were calculated for all granitoid samples and available literature data and presented in figure 11b. These consistently suggest crustal formation ages of ca. 1.4 Ga for all Cycladic ‘I- and S-type’ granites, indicating both granite types were derived from melting a similar aged lower-mid crustal source and are significantly older than model crustal formation ages from the old and recent Hellenic arc.

6. DISCUSSION

6.1 Magmatic Petrogenesis

Trace element geochemistry, Sr–Nd isotopes, and U–Pb geochronology demonstrate that the Cycladic ‘I- and S-type’ granites on Tinos, Delos and Naxos are significantly different from the Pliocene-present day Hellenic arc volcanics. The U–Pb crystallization ages overlap with peak Barrovian metamorphism dated at ca. 17–12 Ma (Keay et al., 2001; Ring et al., 2018; Lamont, 2018; Lamont et al., in press) and highly negative εNd(t) suggest that regionally, the amphibolite-granulite facies metamorphism and both ‘I- and S-type’ magmatism are inherently linked.

Trace elements imply that ‘I-type’ granites had a minimal subduction zone influence (Figs. 8–10). The low Ba/Th ratios (<90) (Fig. 7), overlapping geochemical signatures with that of Variscan basement lithologies, elevated and wide range of Sr, and high concentration of HFSE’s and Rb, and low Ce/Pb ratios, all suggest a crust-dominated source. Although occurrences of mafic xenoliths within the Cycladic plutons have been documented (Avigad et al., 1998; Denèle et al., 2011; Koukouvelas and Kokkalas, 2003; Laurent et al., 2015; Rabillard et al., 2018) and the Tinos and Serifos monzogranites exhibit some titanium enrichment, it has been argued these granitoids are derived from a significant mantle source component (Mastrakas and St. Seymour, 2000; Stouraiti et al., 2018). However, these features can also be explained by melting a crustal mafic source with high titanium contents.

All 'I-type' granites show similar trace element patterns and fall on the same major element vs maficity trend (Figs. 8 and 9). On Tinos, the dacite dykes were derived from the same parent magma as the adjacent monzogranite pluton, albeit less fractionated. All the 'I-type' granitoids across the Cyclades, also show peraluminous compositions, are calcic/ mildly calc-alkalic, magnesium and exhibit lower Rb/Sr and Rb/Ba (Fig. 7), suggesting they formed from low pressure partial melting of a meta-igneous source, likely a result of biotite and hornblende dehydration melting (Patiño Douce and Johnston, 1991; Patiño Douce, 1997; Patiño Douce and McCarthy, 1998).

The 'I-type' granitoids also display different trace elements, REE patterns, fractionation trends, and $^{87}Sr/^{86}Sr$ ratios compared to the 'S-type' granitoids. The 'I-type' granitoids show depleted HREE'S, and positive MREE/HREE ratios, whereas the 'S-types' display concave profiles (Fig. 9). This clearly reflects differences in amphibole versus garnet in the peritectic or residual/fractionated phase assemblage, and implies the two granite types did not evolve from the same parent magma. 'S-type' granites show minor geochemical and mineralogical variation (Figs. 7–10) and a range of Rb/Sr and Al_2O3/TiO_2 ratios between islands (Fig. 7h). This potentially reflects they are sourced from slightly different basement lithologies and/or variable contributions of metasedimentary units, a postulation also highlighted by the variability in $^{87}Sr/^{86}Sr$ diagram (Fig. 11a). The Naxos 'S-type' granites also show the greatest range of $^{87}Sr/^{86}Sr$ isotopic ratios and greatest range in maficity and K_2O and Na_2O contents (Fig. 8). Importantly, the Tinos and Naxos 'S-type' granitoids have higher $^{87}Sr/^{86}Sr$ ratios than the modern volcanic arc system, 'I-type' granitoids and also to that recorded by the Variscan orthogneiss basement. Although the 'S-type' leucogranites on Naxos and Delos were clearly sourced from magmas generated from within the continental crust, it is not obvious whether they were sourced from the peritectic products of migmatites exposed locally on the Naxos and Delos, or from deeper structural levels.

However, the 'S-type' leucogranites are strongly enriched in Rb, depleted in Ba, Sr, Zr, Sc, and REE, and have significant negative Eu anomalies and low K_2O contents (Fig. 8 and 9), similar to highly fractionated granites that have crystallized out significant plagioclase and k-feldspar (Chappell and White, 1992). In addition, the 'S-type' leucogranites have high rare-metal contents (Li, Be, Cs, Sn, and Ta) that are an order of magnitude or more enriched as compared with average upper continental crust (Fig. 8; Rudnick et al., 2003). This, combined with the presence of tourmaline and enrichments of Li, Cs, Sn, Ta, and Be strongly suggests the 'S-type' leucogranites experienced extensive fractional crystallization at lower temperature (London., 2016; Yang et al., 2019). Such extensive fractionation is also inconsistent with leucosome compositions in the Naxos migmatites, which were derived by low-degree (>20%) anatexis of metapelites by dominantly water saturated melting, followed by muscovite dehydration melting at ca. 690–730 °C (Lamont et al., 2019). It is argued that such low melt fractions cannot be easily extracted from the source due to interfacial energy and the relatively low metamorphic temperatures (Rosenberg and Handy, 2005), suggesting the magma is unlikely to have become highly fractionated. We therefore suggest that the 'S-type' leucogranites are not locally sourced from leucosomes exposed in the Naxos or Delos migmatites but are instead derived from muscovite and biotite dehydration melting of Variscan basement paragneiss and underplated metasediments at structurally deeper and hotter levels followed by fractionation of plagioclase and k-feldspar.

At Livada Bay on Tinos, 'S-type' garnet-muscovite leucogranites and cross-cutting biotite leucogranites within the monzogranite pluton are distinct from the adjacent 'I-type' dacite and plutonic rocks, and show similar trace element patterns to Naxos and Delos 'S-type' leucogranites. Although Mastrakas and Seymour (2000), suggested that the 'S-type' leucogranites formed by melting ~28% Tinos monzogranite, we interpret both leucogranites on Tinos as forming by the same mechanism as that proposed for Naxos, with their increased $^{87}Sr/^{86}Sr$ ratios falling on a similar trend line as the Naxos 'S-type' granites and the fact they exhibit much higher Rb/Sr ratios compared to the Tinos 'I-types'. The Tinos 'S-type' leucogranites also display similar mineralogy, major and trace element geochemistry, are depleted in HFSE's and have similar ages to the Naxos leucogranites (14.8–14.2 Ma vs 17–12.2 Ma). However, on Tinos, the source of the 'S-type' magmas is unclear from field relationships alone. Although no migmatites crop out on Tinos, based on Sr-Nd isotopes and the above fractionation arguments, the 'S-type' leucogranites are presumably derived from a similar deep seated Basement metasedimentary source to those on Naxos, and subsequently experienced extensive fractional crystallization (Fig. 11a).

Further insight into granite sources can be gleaned by considering whole-rock Sr–Nd isotopes. These show that the 'I-type' granitoids all have highly negative $\varepsilon Nd(t) = -5$ to -9 (Fig. 11) suggesting a negligible mantle contribution, which is not what would be expected if they were derived from the mantle wedge above the Hellenic slab (even considering significant crustal contamination). Instead, these subchondritic values suggest the parental melts were dominantly crustally-derived and sourced from a variety of igneous/greywacke or mafic protoliths from the Variscan basement. $^{87}Sr/^{86}Sr$ ratios and strongly negative $\varepsilon Nd(t)$ in the dacite dykes and monzogranites overlie previously reported data for the 'I-type' plutons (Altherr and Siebel, 2002; Stouraiti et al., 2010, 2018) and all have significantly more negative $\varepsilon Nd(t)$ to the current Hellenic volcanic arc.

Interestingly, the Sr–Nd isotopic signatures of both 'I- and S-type' granites are very similar (Fig. 11a), suggesting that both are unrelated to the Hellenic slab. Furthermore, the similar U-Pb ages and two-stage model Sm–Nd ages of ca. 1.4 Ga for both 'I and S-type' granitoids imply that both granite types have magma sources that were extracted from the mantle at broadly similar times (Fig. 11b). The Variscan granite basement also provides similar Sm–Nd two stage model ages of ca. 1.4 Ga and zircon inheritance ages (Flansburg et al., 2019). This implies that either the Miocene 'I and S-type' granitoids were derived solely from melting of the Variscan basement, or that both the Miocene granites and Variscan orthogneiss basement were derived from melting of a similar but even older crustal source, potentially Cademonian igneous and sedimentary rocks. To explain the contrasting granite types therefore requires a model whereby the lower-mid crust of the Cyclades comprises a mixture of metasedimentary and metaigneous source rocks that are isotopically similar in terms of the Sm–Nd system. Higher $^{87}Sr/^{86}Sr$ values in the 'S-types' imply a source that was enriched in Rb (i.e., LILE-enriched), which is compatible with a metasedimentary protolith (e.g., Andersen, 1997). We note that the crustal origin of both 'I- and S-type' magmatism has previously been shown in numerous other geochemical and isotopic studies (Pe-Piper, 2000; Altherr and Siebel., 2002) although not thoroughly discussed.

Crust-derived melting to produce 'I-type' magma is further supported by granitoids in Attica, from which ca. 11.2 Ma zircons display textures interpreted to be a result of granulite-facies metamorphism (Liati et al., 2009). Variscan orthogneisses and granites dominate the Cycladic basement (Keay et al., 2001; Lamont et al., 2019; Flansburg et al., 2019), and would be a likely source for 'I-type' magma and is consistent with the distribution of Variscan and older (up to ca. 2.8 Ga) inheritance ages and Sm–Nd two stage model ages of ca. 1.4 Ga (Fig. 10c and Fig. 11b). Post-collision metamorphism and remelting igneous source rocks has also been used to explain the post-collisional 'I-type' granites in the Variscan belt of NW Iberia (e.g., Orejana et al., 2012 and references therein), and several other 'I-type' granitoid and TTG terranes globally (Chappell and Stephens, 1988; Smithies et al., 2009).

The fact that both granite types are derived from partial melting of variable crustal-sources, implies that the entire mid-lower crust of the ACM experienced high-grade metamorphism, probably at amphibolite to granulite facies conditions. 'S-type' granites are also reported from Paros and Ikaria (Iglseder et al., 2009; Stouraiti et al., 2010; McGrath et al., 2017) further supporting this interpretation. Additionally, the previously suggested "thermal anomalies" of the Naxos and Ios metamorphic core complexes (e.g., Ring et al., 2010), are unlikely to be anomalies, but rather tectonic windows that expose the deepest structural levels of the ACM. Biotite and hornblende dehydration melting, required to form the granitoids requires lower crustal metamorphic temperatures >800 °C (Patiño Douce and Harris, 1998). Such high geothermal gradients could have developed by a combination of prolonged crustal thickening culminating in regional kyanite grade metamorphism (Lamont et al., in press), potentially followed by additional short time-scale heating associated with the onset of extension (Platt and England, 1994).

6.2 Timing of Intrusion and Deformation

Our field and U–Pb data suggest the deeper and purely ductile shear zones within the interior of Tinos and Naxos (TSZ, KSZ, ZSZ) are distinct from the overlying brittle-ductile low angle normal faults (NPDS, WCDS, NCDS). The timing of shearing on the structurally deeper shear-zones (TSZ, ZSZ and KSZ) also coincides with peak sillimanite-grade Barrovian metamorphism at ca. 20–14 Ma (Keay et al., 2001; Lamont, 2018), but pre-dates intrusion of the I-type granites. In contrast, the low and high angle normal faults at higher structural levels (NPDS, WCDS, NCDS) clearly cut the I-type granites and structurally deeper shear zones. This suggests that the two sets of structures formed at different times, have different deformation styles and therefore likely formed under two different stress regimes that are separated by the intrusion of 'I-type' granites. Interestingly, several structural studies have shown that the 'I-type' granites were emplaced under a strike-slip stress regime during the transition from compression to extension (Mastrakas and St. Seymour, 2000; Koukouvelas and Kokkalas, 2003; Kokkalas et al., 2006). In what follows we systematically link the crystallization ages of granite magmatism to constrain the timing of compressional and extensional deformation. A summary of the timing of different structures and intrusions is presented in Figure 12 and a tectonic cartoon to illustrate the sequence of tectonothermal events in the Cyclades in Figure 13.

6.2.1 Timing of Shearing and Extension on the KSZ, ZSZ on Naxos

Top-to-NNE movements on the KSZ and ZSZ bounding the migmatite dome (Core Unit) were responsible for the near isothermal decompression of rocks from kyanite to sillimanite-grade conditions (Lamont et al., 2019). Several leucogranites dykes (TL58, TL63, TL69, TL72) cross-cut the KSZ constraining the timing of top-to-NNE shearing as older than ca. 15.5 Ma. Because the KSZ, leucogranites and kyanite-grade fabrics are folded about NNE–SSW trending upright axes (Lamont et al., 2019), significant E–W shortening, and doming of migmatites must post-date top-to-NNE shearing on the KSZ and therefore be younger than ca. 15.5 Ma.

Vertically boudinaged leucogranite dykes from the CHSZ in the center of the migmatite dome (TLN8; Fig. 6b) have U–Pb zircon crystallization ages from at ca. 15.5–14 Ma. To explain the boudinage requires extension in the vertical direction (associated with a vertically orientated σ_3) and therefore a horizontal constrictional stress regime (E–W orientated σ_1 and N–S orientated σ_2) during, or shortly after, leucogranite crystallization. In contrast, NNE–SSW horizontally boudinaged leucogranites (TLN10; Fig. 6e) constrain the onset of horizontal NNE–SSW extension (NNE–SSW orientated σ_3) to be between ca. 15–13.3 Ma. U–Pb dates from a folded aplite sill within the Naxos granodiorite (17TL106; Fig. 6d) also suggest a phase of E–W shortening post-dating the granodiorite crystallization at ca. 12.2 Ma. Similar upright folds with NE–SW trending axes refold the TSZ on Tinos (Fig. 2), suggesting that E–W shortening was a regional tectonic strain (Menant et al., 2013; Virgo et al., 2018).

6.2.2 Timing of Shearing on the NPDS on Naxos

Garnet-Muscovite-Biotite leucogranites that intrude structurally high levels on the western side of Naxos have crystallization dates of ca. 13 Ma and are affected by solid state recrystallization and are rotated into alignment with the NPDS (TL63, TL72; Figure 6a, c). This suggests the NPDS was active shortly after the emplacement of Grt-Bt-Ms leucogranites, and the Hb-Bt pluton at ca. 12.2 Ma (Keay et al., 2001). Ductile deformation was overprinted by brittle deformation on the NPDS constrained by K–Ar ages of ca. 10.3–9.0 Ma from fault gauges (Mancktelow et al., 2016). These data place the timing of brittle faulting and ductile shearing on the NPDS as between 12.2 and 9 Ma. Apatite fission track ages further suggest exhumation through the 100 °C isotherm was complete by ca. 8–10 Ma (Seward et al., 2009). Several normal faults and strike slip faults, possibly associated with a transitional strike-slip stress regime (E–W σ_1 and NNE–SSW σ_3; Kokkalas et al., 2006; Kokkalas and Aydin, 2013), cross-cut the NPDS and the Naxos granodiorite (Koukouvelas and Kokkalas, 2003; Lamont et al., 2019), indicating strain became localized into the upper crust following pluton crystallization and was not purely extensional (Kokkalas et al., 2006).

6.2.3 Timing of Shearing on the TSZ on Tinos

On Tinos, dacite dykes intruded between ca. 14.6–14.4 Ma, immediately prior to, or coeval with, the adjacent I-type monzogranite (ca. 14.8–14.2 Ma), likely derived from melting a similar source. We suggest that the younger K–Ar dates of ca. 12–11 Ma (Avigad et al. 1998) reflect cooling rather than crystallization of the dykes. The range of dates from the I-type monzogranite suggest that pluton emplacement occurred over at least 600 k.y. Early ‘I-type’ monzogranite plutonism in the center of Tinos at ca. 14.8 Ma occurred during the end of localized ductile shearing on the TSZ (TLN34). However, a change in stress conditions following pluton emplacement formed a new extensional strain localization above the pluton roof in the overlying Upper Unit after 14.3 Ma, leaving the pluton interior mostly undeformed.

Ductile movement on the TSZ (NCDS) on Tinos is constrained to ca. 21–14.6 Ma by integrating U–Pb and the Rb–Sr greenschist facies deformation ages of samples close to the TSZ (Bröcker and Franz, 1998). The crystallization of the cross-cutting dacite dykes by ca. 14.6 Ma, and the undeformed interior of the monzogranite at ca. 14.3 Ma (which truncate the TSZ) implies the Upper and Lower Units on Tinos were juxtaposed by at least ca. 14.6 Ma. Pervasive ductile top-to-NE movements along the TSZ therefore pre-date ca. 14.6 Ma, although very minor localized shearing along the pluton margin (TLTN34) may have still been active at ca. 14.8 Ma. However, this deformation did not cause significant displacement, as the Tinos monzogranite pluton shows no offset across the TSZ.

It is unclear whether ductile shearing on the TSZ was related to overall crustal extension or whether it represents a passive roof fault, associated with extrusion processes (Searle and Lamont, 2019). Structural studies have shown the Tinos pluton intruded under firstly a compressional stress field followed by an extensional stress field (Mastrakas and St. Seymour, 2000). Because the TSZ pre-dates the Tinos pluton and the fact that the TSZ is steeply folded about NE–SW trending axes (Fig. 2; Lamont et al., 2020a,2020b), this would be consistent with the structure forming under a phase of regional compression and therefore the TSZ would represent a passive roof fault.

6.2.4 Timing of Shearing on the NCDS on Tinos and Mykonos

At Livada Bay, ‘S-type’ leucogranites are clearly offset by brittle normal faults and therefore constrain the onset of brittle normal faulting to be younger than ca. 14.2–14.0 Ma (TLTN13, TLTN15). These dates bracket a maximum age for the onset of NE–SW crustal extension on Tinos. Furthermore, no older brittle normal faults are preserved that can be rigorously demonstrated to be older than these dates anywhere in the Cyclades.

The Tinos ‘S-type’ leucogranite ages are also within analytical uncertainty of the I-type monzogranite and dacite dykes. This potentially implies that significant exhumation occurred over the time-scale of granite intrusions (300 k.y.), in order to explain how the close spatial and temporal relationship of ‘I- and S-type’ granites. Because leucogranites and brittle normal faults at Livada Bay are in the hangingwall of the TSZ and the Livada Detachment (i.e., the detachments structurally underlie the S-type leucogranites), we tentatively suggest these structures are not responsible for this exhumation. The TSZ and Livada Detachment are likely cut by a normal fault younger than 14.8 Ma, which was responsible for the remainder of the footwall exhumation, or by high-angle faulting to the south of Tinos and Andros that likely creates the prominent topography along the southern coastlines.

The timing of shearing and the development of different detachments associated with the NCDS must also vary along strike. The ca. 13.3 Ma Mykonos monzogranite (Figs. 1 and 4) is cut by a ductile shear zone that Jolivet et al., (2010) refer to as the Livada Detachment (Fig. 4a), suggesting it is younger than 13.3 Ma. However, this is unlikely to be the same structure exposed at Livada Bay on Tinos (also referred to as the Livada Detachment by Jolivet et al., 2010) (Fig. 2b). This is because pervasive shearing must have ceased by ca. 14.6 Ma on Tinos as it is cut by dacite dykes, Grt-Ms leucogranite sills and brittle high-angle faults.

At the highest structural levels on Mykonos, the Mykonos Detachment places silicified Miocene sediments above meta-basalts of the metamorphic sole to the Tsiknias Ophiolite (Fig. 4a). Cross-cutting barite veins derived from post-crystallization hydrothermal alteration on the margins of the granite, cut through both the Livada and Mykonos Detachments (Menant et al., 2013). The Mykonos Detachment therefore accommodated exhumation during the cooling of the Mykonos monzogranite after ca. 13.3 Ma (Brichau et al., 2008; Denèle et al., 2011; Rabillard et al., 2018). However, on Tinos and Andros, the Mykonos Detachment is not exposed. One possibility is that the Mykonos Detachment represents the cryptic fault forming higher in the crust projected further north offshore Tinos, and was responsible for the exhumation of Tinos.

6.3 Tectonics

6.3.1 Timing of E–W Shortening

Many of the ACM plutons are interpreted to have intruded during a strike-slip stress field involving a significant component of E–W shortening during the Late Miocene (Boronkay and Doutsos, 1994; Mastrakas and St. Seymour, 2000; Koukouvelas and Kokkalas, 2003; Kokkalas et al., 2006; Kokkalas and Aydin, 2013), therefore some further constraints can be made about the timing of E–W shortening. On Tinos, the ca. 14.6–14.4 Ma dacite dykes (TLT64,17TL05 and 17TL36) are oriented at steep-moderate angles converging toward the NW–SE dome axis trending down the center of the island. The dykes may have been rotated from their original geometry (assumed vertical). Similar observations can also be made on leucogranites emanating from the Core Unit and migmatite dome on Naxos, dated at ca. 16–12.8 Ma (TLN8, TL72; Fig. 6). Because the structurally deeper and purely ductile shear zones (TSZ, ZSZ and KSZ) on Tinos and Naxos are also folded about the major doming axis in a similar fashion to the dykes, it implies doming and NNE–SSW trending folds with vertical axial planes must post-date dyke intrusion, and hence be younger than ca. 14 Ma. The particularly steep east and west coastlines on Tinos and Naxos also could not have been related to isostatic rebound associated with regional extension, as the metamorphic foliation often dips away from both islands at up to ca. 50°. We postulate all these features require a regional phase of E–W shortening that was coeval with the intrusion of ‘I- and S-type’ granites and continued during movement on the structurally higher low-angle normal faults (NCDS, NPDS). On Naxos and Paros, the Miocene–Pliocene sediments are also folded and affected by east and west verging thrust faults (Dermitzakis et al., 1979; Angelier 1978, Meulenkamp et al., 1988). The NPDS and overlying sediments also dip away from the core complexes (rather than into the core complex/ NPDS), further suggesting that E–W shortening was an important component of the regional stress field (Searle and Lamont, 2019), presumably related to westward movement of Anatolia during the mid-late Miocene (e.g., Philippon et al., 2014).

6.3.2 Timing of Aegean Extension

It is highly debated when regional Aegean extension initiated. Many studies have argued for prolonged extension throughout the Cenozoic based on: (i) The apparent southward migration of magmatism across the Aegean, interpreted to represent the migration of the volcanic arc due to Hellenic slab roll-back (e.g., Fytikas et al, 1984; Jolivet and Brun, 2010; Jolivet et al., 2013). (ii) The presence of Miocene shallow-marine sediments with Aquitanian to Early Burdigalian faunas (Angelier,1978; ca. 23–19 Ma) in the Upper Unit, suggesting the crust had already thinned by the Miocene. (iii) The presence of ‘extensional’ S–C’ shear fabrics within metamorphic core complexes which yield a spectrum of Ar–Ar and Rb–Sr ages spanning Eocene–Miocene, interpreted to represent deep crustal extension (Lister et al., 1984; Jolivet and Brun, 2010).

Although prolonged Aegean extension can explain many geological phenomena in the ACM (Fig. 14a), this model fails to explain several key observations and data presented in this study: (i) The Hellenic volcanic arc has remained in a similar position since ca. 5 Ma, and no calc-alkaline extrusive volcanic rocks pre-date these since the Late Cretaceous volcanic and intrusive rocks on Anafi, which are in fact related to a previous subduction zone (e.g., Matsuda et al., 1999; Pe-Piper and Piper, 2005, Gerogiannis et al., 2019; Elburg and Smet, 2020; Koutsovitis et al., 2021). Pliocene volcanism associated with the Hellenic Arc is limited to Milos, Kimolos and Polyegos, and the Saronic Gulf including Aegina, Methana, Poros and Cromyonnia, and no arc-related volcanism has been found to pre-date these ages (Pe-Piper and Hatzipanagiotou, 1997; Francalanci et al., 2007; Elburg and Smet, 2020). Interpreting the ‘I-type’ granites as representing the deeper levels of the Hellenic volcanic arc is incompatible with our Sr–Nd isotopic data, which clearly show that the Cyclades ‘I-type’ granites are crustal derived and likely a product of regional metamorphism. The argument for the volcanic arc migrating southwards throughout the Cenozoic due to Hellenic slab roll-back (Fytikas et al, 1984; Jolivet and Brun, 2010) is therefore not supported by our data. (ii) The Miocene marine sediments within the Upper Unit are not necessarily related to crustal extension. It is equally possible these sediments were deposited to the south of the Cyclades corresponding to the Sea of Crete in present day coordinates (Dermitzakis et al., 1979; Kulheman, 2004). The Miocene sediments are also affected by folds with steep-vertical axial planes, and thrusting, and show a transgression to continental fluvial facies during the Miocene (Dermitzakis et al., 1979; Kuhleman et al., 2004). This suggests significant Miocene uplift, presumably from E–W compression, which is also affects structurally deeper Barrovian metamorphic rocks (Lamont et al., 2019; Searle and Lamont, 2019). (iii) The ‘extensional’ S–C’ shear fabrics exposed within many of the Cycladic Islands did not necessarily form due to overall crustal extension. As stated above, these microstructures also occur along passive roof faults (Means, 1989) in many compressional mountain belts such as the South Tibetan Detachment along the top of the Greater Himalayan Series (Law et al., 2006; Searle, 2010), and in exhumed subduction complexes due to extrusion processes. Extensional S–C’ fabrics alone therefore cannot be used independently as evidence for crustal or lithospheric extension (Searle and Lamont, 2019). (iv) It is also possible that Aegean extension arises from gradients of gravitational potential energy arising from variations in crustal thickness; (England et al., 2016) indicate that the tractions applied to the base of the lithosphere due to slab rollback are insignificant compared to stresses induced due to gravity.

Further constraints on the timing of extension can be interpreted from the cross-cutting granite - fault relations. At deep structural levels, amphibolite to greenschist-facies top-to-(N)NE shearing pre-dates 'I-type' magmatism and occurred on the structurally deeper ductile shear zones (KSZ, ZSZ and TSZ), between ca. 21–14.8 Ma for Tinos (Bröcker et al., 1993, 2004; Brichau et al., 2007) and ca. 20–15 Ma for Naxos (Keay et al., 2001; Lamont et al., 2019). The TSZ, ZSZ and KSZ are cut by the brittle-ductile low-angle normal faults (NCDS and NPDS) and are folded about NNE–SSW and WNW–ESE trending axes around Tinos Island and the Naxos migmatite dome (Lamont et al., 2019, 2020a,b). The doming and folding of the TSZ, ZSZ and KSZ suggest they pre-dated a phase of Miocene E–W shortening and horizontal constrictional stress, and therefore pre-date crustal extension. It is also possible these shear zones represent passive roof faults that formed above an extruding wedge of Barrovian metamorphic rocks under regional compression that refolds the structures (Lamont et al., 2019).

If, on the other hand, the TSZ, ZSZ and KSZ represent deeper structural levels of the crustal scale low-angle normal faults, we would expect these structures to coalesce into the overlying brittle-ductile structures (NCDS and NPDS). We may also expect strong conductive cooling of footwall rocks (England and Jackson, 1987). Both these predictions are not observed as the KSZ and ZSZ are cut by the later normal faults. Naxos Barrovian rocks also only experienced limited (<30 °C) cooling during their initial decompression from ca. 10–5 kbar (Lamont et al., 2019) associated with muscovite dehydration melting and shearing on the KSZ and ZSZ followed by migmatite doming that refolds the shear zones. In contrast, rapid core complex cooling occurred after ca. 15 Ma associated with the initiation of the NPDS (Seward et al., 2009; Mancktelow et al., 2016; Lamont et al., in press).

At Livada Bay on Tinos, normal-faults cross-cutting 'S-type' granites constrain a maximum age of brittle normal faulting of ca. 14.2 Ma, that represent the clearest evidence for an NNE–SSW horizontal minimum principal stress (σ^3) reflecting extensional strains in the ACM. Although this is only one normal fault outcrop, and caution must be taken applying this data to the rest of the ACM, this ca. 14.2 Ma age of extension is consistent with maximum extension ages from Naxos, based of NNE–SSW horizontally boudinaged 'S-type' granites and rapid core complex cooling due to the initiation of the NPDS after ca. 15 Ma (Lamont et al., 2019, in press; Searle and Lamont, 2019; Seward et al., 2009).

Additionally, the intrusion of large granite bodies into the upper crust from ca. 14.8 Ma may require a relaxation of compressional stress (Loucks, 2021). This may be consistent with the development of a strike-slip stress field during emplacement of the 'I-type' plutons during the transition from compression to extension (Kissel and Laij, 1988; Boronkay and Doutsos, 1994; Mastrakas and St. Seymour, 2000; Koukouvelas and Kokkalas, 2003; Kokkalas et al., 2006; Kokkalas and Aydin, 2013; Faucher et al., 2021).

ACM extension commencing at ca. 15 Ma would also be consistent with a twofold decrease in the Nubia-Eurasia convergence rate between ca. 18–13 Ma (DeMets et al., 2015). This decreased convergence rate would cause a reduction in horizontal deviatoric stresses and the regions with the thickest crust and highest topography to extend (Dalmayrac and Molnar, 1981). Alternatively, the decreased convergence rate could reflect: (1) The arrival of dense oceanic lithosphere at the subduction zone (Royden and Papanikolaou, 2011), which caused rollback of the Hellenic slab and extension in the overriding Aegean crust (Fig. 14a e.g., Schellart et al., 2004; Burchfiel et al., 2008; Papanikolaou and Vassilakis, 2010; van Hinsbergen and Schmid, 2012); or (2) Convective removal of the lithospheric mantle at ca. 15 Ma (Fig. 14b) resulting in an increase in gravitational potential energy causing a switch from compression to extension (England and Houseman, 1989; Platt and England, 1994;

Houseman and Molnar, 1997). Both geodynamic models could also potentially explain: (i) the potassic and ultra-potassic alkali magmatism in Western Turkey due to melting a lithospheric mantle source that also initiated at ca. 15 Ma (Soder et al., 2016; Caran, 2016). (ii) transient heating of the lower crust due advection of warmer asthenosphere (Platt and England, 1994), resulting in short time-scale granulite facies metamorphism and crustal derived magmatism coincident with the onset of regional extension.

7. CONCLUSIONS

1. The intrusion of 'I- and S-type' granites on Tinos, Delos and Naxos occurred contemporaneously between ca. 17–12 Ma (Fig. 10a), within the uncertainty of the U–Pb dates. Sr–Nd isotopes demonstrate both granite types have highly negative εNd(t) (−6.3 to −10.1) implying melting of an ancient crustal reservoir (Fig. 11a). This cannot be explained by their derivation from recent extraction of juvenile melts from the mantle wedge above the Hellenic subduction zone. Two stage Sm–Nd model ages of ~1.4 Ga for both granite types are comparable with Variscan basement model ages, and are significantly different to the Hellenic arc volcanics (Fig. 11b). The coeval nature of 'I- and S-type' magmatism is best explained by regional metamorphism resulting in extensive lower crustal melting of the ACM (Fig. 13). Coeval melting of lower crustal igneous source rocks including amphibolites and Variscan or Camedonian orthogneiss formed the hornblende-biotite bearing granitoids, and mid-crustal partial melting of meta-sedimentary sources formed the garnet-muscovite-biotite leucogranites. I Both granite types were likely sourced much deeper crustal levels than those exposed and have experienced extensive fractionation.

2. In terms of the classification of these granitoids, we propose that both granite types should be reconsidered as crust-derived granites. The differences in their geochemistry arise from melting of different crustal source rocks and experiencing different degrees of fractional crystallization, with the I- and S-types broadly reflecting the melting of metaigneous and metasedimentary protoliths, respectively.

3. The Tinos monzogranite pluton intruded between ca. 14.8–14.3 Ma, with dacite dykes derived from the same parent magma intruding between ca. 14.7–14.4 Ma, whereas the 'I-type' Mykonos monzogranite, Naxos granodiorite and Serifos granite crystallized at 13.3 Ma, 12.2 Ma and 11 Ma respectively. These dates constrain the initiation of the Aegean low angle normal faults which cut the plutons (NCDS, NPDS and WCDS). The TSZ was active between ca. 21–14.6 Ma and is cut by the Tinos monzogranite pluton that we believe intruded under a transitional strike slip stress regime. During the switch to regional extension, a new strain localization formed above the Tinos pluton roof and initiated the Livada and Mykonos Detachments which are younger than ca. 14.6 and 13.3 Ma respectively (Fig. 13). On Naxos, ductile shearing on the NPDS commenced after the granodiorite intruded at ca. 12.2 Ma and was responsible for rapid core complex cooling. The intrusion of granitoids immediately prior to, and during ductile shearing on low-angle normal faults suggest the NCDS, NPDS and WCDS acted as structural lids for magma to intrude into the upper crust during the onset of crustal extension.

4. Naxos leucogranites dated at ca. 15.5–14 Ma constrain the final movement on the KSZ and ZSZ, that were responsible for the exhumation of kyanite- and sillimanite- grade gneisses and migmatites from ca. 10–5 kbar (Lamont et al., 2019). The KSZ and ZSZ are cut by the NPDS, active between ca. 12.2 and 9 Ma (Fig. 13). Garnet-muscovite leucogranite sills at Livada Bay on Tinos intruded between ca. 14.8–14.3 Ma and are cut by brittle normal faults. The granite crystallization ages therefore constrain the brittle normal faulting to be younger than ca. 14.3 Ma. This is consistent with evidence for a switch in stress regime in the core of the Naxos migmatite dome where NNE–SSW horizontally boudinaged S-type leucogranite dykes are dated at ca. 15–14 Ma, (vertically orientated σ_1 and NNE–SSW orientated σ_3) suggesting horizontal extensional strains affected the ACM after ca. 15 Ma.

DOI:10.1130/B36489.1

5. The switch from compression to extension at ca. 15 Ma may also be compatible with increased heat flow through the base of the crust, resulting in granulite facies metamorphism and partial melting of the Cyclades lower crust between ca. 15 Ma and 10 Ma following a prolonged period of crustal thickening. The limited geographic extent of granitoids and high-grade metamorphism also suggests that crustal magmatism was localized to the ACM, and not related to the Hellenic subduction zone. The switch from a compressional to extensional stress field could be due to either a twofold decrease in convergence rate between Nubia and Eurasia at 18–13 Ma (DeMets et al., 2015), or removal of the lithospheric mantle (Fig. 14b), but not necessarily involving slab rollback of the Hellenic subduction zone.

ACKNOWLEDGEMENTS

This work forms part of T.N. Lamont’s doctorate funded by the Natural Environment Research Council (NE/L0021612/1). Analytical work was funded by NIGFSC grant IP-1597–1115. We would like to thank Steve Wyatt and Adrian Wood for help with sample preparation, Stanley Mertzman for XRF analyses, and Gren Turner, Jeremy Rushton and Jon Wade for analytical assistance. Philip England, Peter Molnar, Jon Wade, Dave Waters, Laurence Robb, Tony Watts, Paul Savage and Will Hutchinson are also thanked for thought-provoking and critical discussion. Sotirios Kokkalas and Jesse Walters are thanked for providing critical and helpful reviews and comments that substantially improved the quality of the manuscript and Mihai Ducea and Kathryn Cutts are thanked for their careful editorial handling.

REFERENCES CITED

Altherr, R., and Siebel, W., 2002, I-type plutonism in a continental back-arc setting: Miocene granitoids and monzonites from the central Aegean Sea, Greece: Contributions to Mineralogy and Petrology, v. 143, p. 397, https://doi.org/10.1007/s00410-002-0352-y.

Altherr, R., Kreuzer, H., Wendt, I., Lenz, H. and Wagner, G.A., 1982, A late Oligocene/early Miocene high temperature belt in the Attic-Cycladic crystalline complex (SE Pelagonian, Greece): Geologisches Jahrbuch. Reihe E, Geophysik, no. 23, p. 97–164.

Altherr, R., Henjes-Kunst, F., Matthews, A., Friedrichsen, H., and Hansen, B.T., 1988, O-Sr isotopic variations in Miocene granitoids from the Aegean: evidence for an origin by combined assimilation and fractional crystallization: Contributions to Mineralogy and Petrology, v. 100, no. 4, p. 528–541, https://doi.org/10.1007/BF00371381.

Andersen, T., 1997, Radiogenic isotope systematics of the Herefoss granite, South Norway: an indicator of Sveconorwegian (Grenvillian) crustal evolution in the Baltic Shield: Chemical Geology, v. 135, no. 1–2, p. 139–158, https://doi.org/10.1016/S0009-2541(96)00095-2.

Angelier, J., 1978, Tectonic evolution of the Hellenic Arc since the late Miocene: Tectonophysics, v. 49, no. 1–2, p. 23–36, https://doi.org/10.1016/0040-1951(78)90096-3.

Avigad, D., and Garfunkel, Z., 1989, Low-angle faults above and below a blueschist belt—Tinos Island, Cyclades, Greece: Terra Nova, v. 1, p. 182–187, https://doi.org/10.1111/j.1365-3121.1989.tb00350.x.

Avigad, D., and Garfunkel, Z., 1991, Uplift and exhumation of high-pressure metamorphic terrains: the example of the Cycladic blueschist belt (Aegean Sea): Tectonophysics, v. 188, p. 357–372, https://doi.org/10.1016/0040-1951(91)90464-4.

Avigad, D., Baer, G., and Heimann, A., 1998, Block rotations and continental extension in the central Aegean Sea: palaeomagnetic and structural evidence from Tinos and Mykonos: Earth and Planetary Science Letters, v. 157, p. 23–40, https://doi.org/10.1016/S0012-821X(98)00024-7.

Bailey, J.C., Jensen, E.S., Hansen, A., Kann, A.D.J., and Kann, K., 2009, Formation of heterogeneous magmatic series beneath North Santorini, South Aegean island arc: Lithos, v. 110, p. 20–36, https://doi.org/10.1016/j.lithos.2008.12.002.

Beaudoin, A., Augier, R., Laurent, V., Jolivet, L., Lahfid, A., Bossé, V., Arbaret, L., Rabillard, A., and Menant, A., 2015, The Ikaria high-temperature Metamorphic Core Complex (Cyclades, Greece): Geometry, kinematics and thermal structure: Journal of Geodynamics, v. 92, https://doi.org/10.1016/j.jog.2015.09.004.

Bolhar, R., Ring, U., and Allen, C.M., 2010, An integrated zircon geochronological and geochemical investigation into the Miocene plutonic evolution of the Cyclades, Aegean Sea, Greece: Part 1: Geochronology: Contributions to Mineralogy and Petrology, v. 160, p. 719–742, https://doi.org/10.1007/s00410-010-0504-4.

Bolhar, R., Ring, U., and Ireland, T.R., 2017, Zircon in amphibolites from Naxos, Aegean Sea, Greece: origin, significance and tectonic setting: Journal of Metamorphic Geology, v. 35, no. 4, p. 413–434, https://doi.org/10.1111/jmg.12238.

Bouvier, A., et al., 2008, The Lu–Hf and Sm–Nd isotopic composition of CHUR: Constraints from unequilibrated chondrites and implications for the bulk composition of terrestrial planets: Earth and Planetary Science Letters, v. 273, no. 1–2, p. 48–57, https://doi.org/10.1016/j.epsl.2008.06.010.

Boronkay, K., 1995. Geotectonic evolution of the Cyclades. Unpublished PhD, Univ. of Patras, 193 p.

Boronkay, K., and Doutsos, T., 1994, Transpression and transtension within different structural levels in the central Aegean region: Journal of Structural Geology, v. 16, no. 11, p. 1555–1573, https://doi.org/10.1016/0191-8141(94)90033-7.

Braschi, E., Francalanci, L., and Vougioukalakis, G.E., 2012, Inverse differentiation pathway by multiple mafic magma refilling in the last magmatic activity of Nisyros Volcano, Greece: Bulletin of Volcanology, v. 74, p. 1083–1100, https://doi.org/10.1007/s00445-012-0585-1.

Brichau, S., Ring, U., Carter, A., Monie, P., Bolhar, R., Stockli, D., and Brunel, M., 2007, Extensional faulting on Tinos Island, Aegean Sea, Greece: How many detachments?: Tectonics, v. 26, p. TC4009, https://doi.org/10.1029/2006TC001969.

Brichau, S., Ring, U., Carter, A., Bolhar, R., Monié, P., Stockli, D., and Brunel, M., 2008, Timing, slip rate, displacement and cooling history of the Mykonos detachment footwall, Cyclades, Greece, and implications for the opening of the Aegean Sea basin: Journal of the Geological Society, v. 165, p. 263–277, https://doi.org/10.1144/0016-76492006-145.

Briqueu, L., Javoy, M., Lancelot, J.R., and Tatsumoto, M., 1986, Isotope geochemistry of recent magmatism in the Aegean arc: Sr, Nd, Hf and O isotopic ratios in the lavas of Milos and Santorini-geodynamic implications: Earth and Planetary Science Letters, v. 80, p. 41–54, https://doi.org/10.1016/0012-821X(86)90018-X.

Bröcker, M., and Franz, L., 1994, The contact aureole on Tinos (Cyclades, Greece). Part I: field relationships, petrography and P-T conditions: Chemie der Erde, v. 54, p. 262–280.

Bröcker, M., and Franz, L., 1998, Rb–Sr isotope studies on Tinos Island (Cyclades, Greece): Additional time constraints for metamorphism, extent of infiltration-controlled overprinting and deformational activity: Geological Magazine, v. 135, p. 369–382, https://doi.org/10.1017/S0016756898008681.

Bröcker, M., and Franz, L., 2000, Contact metamorphism on Tinos (Cyclades, Greece): the importance of tourmaline, timing of the thermal overprint and Sr isotope characteristics: Mineralogy and Petrology, v. 70, p. 257–283.

Bröcker, M., Kreuzer, A., Matthews, A., and Okrusch, M., 1993, $^{40}Ar/^{39}Ar$ and oxygen isotope studies of poly-metamorphism from Tinos Island, Cycladic blueschist belt, Greece: Journal of Metamorphic Geology, v. 11, p. 223–240, https://doi.org/10.1111/j.1525-1314.1993.tb00144.x.

Bröcker, M., Bieling, D., Hacker, B., and Gans, P., 2004, High-Si phengite records the time of greenschist facies overprinting: Implications for models suggesting mega-detachments in the Aegean Sea: Journal of Metamorphic Geology, v. 22, p. 427–442, https://doi.org/10.1111/j.1525-1314.2004.00524.x.

Buettner, A., Kleinhanns, I.C., Rufer, D., Hunziker, J.C., and Villa, I.M., 2005, Magma generation at the easternmost section of the Hellenic arc: Hf, Nd, Pb and Sr isotope geochemistry of Nisyros and Yali volcanoes (Greece): Lithos, v. 83, no. 1–2, p. 29–46, https://doi.org/10.1016/j.lithos.2005.01.001.

Buick, I.S., 1991a, Mylonite fabric development on Naxos, Greece: Journal of Structural Geology, v. 13, p. 643–655, https://doi.org/10.1016/0191-8141(91)90027-G.

Buick, I.S., 1991b, The late Alpine evolution of an extensional shear zone, Naxos, Greece: Journal of the Geological Society, v. 148, p. 93–103, https://doi.org/10.1144/gsjgs.148.1.0093.

Buick, I.S., and Holland, T.J.B., 1989. The P-T-t path associated with crustal extension, in Daly, J.S., Cliff, R.A., and Yardley, W.D., eds., Evolution of Metamorphic Belts: Geological Society of London Special Publication v. 43, p. 365–369.

Bulle, F., Bröcker, M., Gärtner, C., and Keasling, A., 2010, Geochemistry and geochronology of HP mélanges from Tinos and Andros, Cycladic blueschist belt, Greece: Lithos, v. 117, no. 1–4, p. 61–81, https://doi.org/10.1016/j.lithos.2010.02.004.

Burchfiel, B. C., R. Nakov, N. Dumurdzanov, D. J. Papanikolaou, T. Z. Tzankov, T. Serafimovski, R. W. King, V. Kotsev, A. Todosov, and B. Nurce (2008), Evolution and dynamics of the Cenozoic tectonics of the South Balkan extensional system, Geosphere, 4, 919– 938, doi:10.1130/GES00169.1.

Caran, S., 2016, Mineralogy and petrology of leucite ankaratrites with affinities to kamafugites and carbonatites from the Kayıköy area, Isparta, SW Anatolia, Turkey: Implications for the influences of carbonatite metasomatism into the parental mantle sources of silica-undersaturated potassic magmas: Lithosphere, v. 256–257, p. 13–25, https://doi.org/10.1016/j.lithos.2016.03.024.

Cao, S., Neubauer, F., Bernroider, M., and Liu, J. 2013. The lateral boundary of a metamorphic core complex: The Moutsounas shear zone on Naxos, Cyclades, Greece. Journal of Structural Geology, v. 54, p. 103-128.

Chakrabarti, R., Basu, A.R. and Ghatak, A., 2012. Chemical geodynamics of western Anatolia. International Geology Review, v. 54(2), p. 227–248.

Chappell, B.W., 1984, Source rocks of I- and S-type granites in the Lachlan Fold Belt, southeastern Australia: Philosophical Transactions of the Royal Society of London. Series A, Mathematical and Physical Sciences, v. 310, p. 693–707.

Chappell, B.W., and Stephens, W.E., 1988, Origin of infracrustal (I-type) granite magmas: Transactions of the Royal Society of Edinburgh. Earth Sciences, v. 79, p. 71–86, https://doi.org/10.1017/S0263593300014139.

Chappell, B.W., and White, A.J.R., 1974, Two contrasting granite types: Pacific Geology, v. 8, p. 173–174.

Chappell, B.W., and White, A.J., 2001, Two contrasting granite types: 25 years later: Australian Journal of Earth Sciences, v. 48, no. 4, p. 489–499, https://doi.org/10.1046/j.1440-0952.2001.00882.x.

Chappell, B.W., and White, A.J.R., 1992, I-type and S-type granites in the Lachlan Fold Belt: Transactions of the Royal Society of Edinburgh. Earth Sciences, v. 83, p. 1–26, https://doi.org/10.1017/S0263593300007720.

Chew, D.M., Sylvester, P.J. and Tubrett, M.N., 2011. U–Pb and Th–Pb dating of apatite by LA-ICPMS. Chemical Geology, v. 280(1-2), p. 200-216.
Clemens, J.D., 2012, Granitic magmatism, from source to emplacement: a personal view: Transactions of the Institution of Mining and Metallurgy Section B. Applied Earth Science, v. 121, no. 3, p. 107–136, https://doi.org/10.1179/1743275813Y.0000000023.
Clemens, J.D., Helps, P.A., and Stevens, G., 2009, Chemical structure in granitic magmas–a signal from the source?: Earth and Environmental Science Transactions of the Royal Society of Edinburgh, v. 100, no. 1–2, p. 159–172, https://doi.org/10.1017/S1755691009016053.
Clemens, J.D., Stevens, G., and Bryan, S.E., 2020, Conditions during the formation of granitic magmas by crustal melting–hot or cold; drenched, damp or dry?: Earth-Science Reviews, v. 200, p. 102982, https://doi.org/10.1016/j.earscirev.2019.102982.
Collins, W.J., Huang, H.Q., Bowden, P., and Kemp, A.I.S., 2020a, Repeated S–I–A-type granite trilogy in the Lachlan Orogen and geochemical contrasts with A-type granites in Nigeria: implications for petrogenesis and tectonic discrimination: Geological Society of London, Special Publications, v. 491, no. 1, p. 53–76, https://doi.org/10.1144/SP491-2018-159.
Collins, W.J., Murphy, J.B., Johnson, T.E., and Huang, H.Q., 2020b, Critical role of water in the formation of continental crust: Nature Geoscience, v. 13, no. 5, p. 331–338, https://doi.org/10.1038/s41561-020-0573-6.
Dalmayrac, B., and Molnar, P., 1981, Parallel thrust and normal faulting in Peru and constraints on the state of stress: Earth and Planetary Science Letters, v. 55, p. 473–481, https://doi.org/10.1016/0012-821X(81)90174-6.
DeMets, C., Iaffaldano, G., and Merkouriev, S., 2015, High-resolution Neogene and Quaternary estimates of Nubia-Eurasia-North America Plate motion: Geophysical Journal International, v. 203, p. 416–427, https://doi.org/10.1093/gji/ggv277.
Denèle, Y., Lecomte, E., and Jolivet, L., Lacombe, Olivier., Labrousse, Loic et al. 2011, Granite intrusion in a metamorphic core complex: The example of the Mykonos laccolith (Cyclades, Greece): Tectonophysics, v. 501 (1–4), p.52–70. https://doi.org/10.1016/j.tecto.2011.01.013. insu-00563983.
Dermitzakis, M., Papanikolaou, D., Theodoridis, S., and Mirkou, R., 1979, The molasse of Paros Island, Aegean Sea: Annalen des Naturhistorischen Museums in Wien, v. 83, p. 59–71.
Dragovic, B., Samanta, L.M., Baxter, E.F., and Selverstone, J., 2012, Using garnet to constrain the duration and rate of water-releasing metamorphic reactions during subduction: An example from Sifnos, Greece: Chemical Geology, v. 314–317, p. 9–22, https://doi.org/10.1016/j.chemgeo.2012.04.016.
Dragovic, B., Baxter, E.F., and Caddick, M.J., 2015. Pulsed dehydration and garnet growth during subduction revealed by zoned garnet geochronology and thermodynamic modeling, Sifnos, Greece, *Earth and Planetary Science Letters*, v. 413, p. 111–122, ISSN 0012–821X, https://doi.org/https://doi.org/10.1016/j.epsl.2014.12.024.
Ducea, M.N., Saleeby, J.B., and Bergantz, G., 2015, The architecture, chemistry, and evolution of continental magmatic arcs: Annual Review of Earth and Planetary Sciences, v. 43, p. 299–331, https://doi.org/10.1146/annurev-earth-060614-105049.
Elburg, M.A., and Smet, I., 2020, Geochemistry of lavas from Aegina and Poros (Aegean Arc, Greece): Distinguishing upper crustal contamination and source contamination in the Saronic Gulf area: Lithos, v. 358–359, https://doi.org/10.1016/j.lithos.2020.105416.
England, P.C., and Houseman, G., 1989, Extension during continental convergence, with application to the Tibetan Plateau: Journal of Geophysical Research, v. 94, B12, p. 17,561–17,579, https://doi.org/10.1029/JB094iB12p17561.

England, P.C., and Jackson, J., 1987, Migration of the seismic-aseismic transition during uniform and non-uniform extension of the continental lithosphere: Geology, v. 15, p. 291–294, https://doi.org/10.1130/0091-7613(1987)15<291:MOTSTD>2.0.CO;2.

England, P.C., Houseman, G., and Nocquet, J.M., 2016, Constraints from GPS measurements on the dynamics of deformation in Anatolia and the Aegean: Journal of Geophysical Research. Solid Earth, v. 121, p. 8888–8916, https://doi.org/10.1002/2016JB013382.

Ersoy, E.Y. and Palmer, M.R., 2013. Eocene-Quaternary magmatic activity in the Aegean: Implications for mantle metasomatism and magma genesis in an evolving orogeny. Lithos, v. 180, p. 5–24.

Faucher, A., Gueydan, F., Jolivet, M., Alsaif, M., and Celerier, B., 2021, Dextral strike-slip and normal faulting during middle Miocene back-arc extension and westward Anatolia extrusion in Central Greece. *Tectonics*, v. 40 (6), pp.e2020TC006615. ff10.1029/2020TC006615ff. ffhal-03175867f

Faure, M., Bonneau, M., and Pons, J., 1991. Ductile deformation and syntectonic granite emplacement during the late Miocene extension of the Aegean (Greece): Bulletin de la Société Géologique de France, v. 162, p. 3–12.

Faure, M., M. Bonneau, and J. Pons, 1991, Ductile deformation and syntectonic granite emplacement during the late Miocene extension of the Aegea (Greece), Bulletin Societe Geologique France., v. 162, p. 3–11.

Flansburg, M.E., Stockli, D.F., Poulaki, E.M., and Soukis, K., 2019, Tectono-magmatic and stratigraphic evolution of the Cycladic Basement, Ios Island, Greece: Tectonics, v. 38, p. 2291–2316, https://doi.org/10.1029/2018TC005436.

Francalanci, L., Vougioukalakis, G.E., and Fytikas, M., 2007. Petrology and volcanology of Kimolos and Polyegos volcanoes within the context of the South Aegean arc, Greece, *in* Beccaluva, L., Bianchini, G., Wilson, M., Geological Society of America Special Paper, *Cenozoic Volcanism in the Mediterranean Area*, https://doi.org/10.1130/2007.2418(03)

Frost, B.R., Barnes, C.G., Collins, W.J., Arculus, R.J., Ellis, D.J. and Frost, C.D., 2001. A geochemical classification for granitic rocks. Journal of petrology, v. 42(11), p. 2033–2048.

Fytikas, M., Innocenti, F., Manetti, P., Peccerillo, A., Mazzuoli, R., and Villari, L., 1984, Tertiary to Quaternary evolution of volcanism in the Aegean region: Geological Society of London, Special Publications, v. 17, no. 1, p. 687–699, https://doi.org/10.1144/GSL.SP.1984.017.01.55.

Gerogiannis, N., Xypolias, P., Chatzaras, V., Aravadinou, E., and Papapavlou, K., 2019, Deformation within the Cycladic subduction–exhumation channel: new insights from the enigmatic Makrotantalo nappe (Andros, Aegean): International Journal of Earth Sciences, v. 108, p. 817–843, https://doi.org/10.1007/s00531-019-01680-3.

Gorce, J.S., Caddick, M.J., Baxter, E.F., Dragovic, B., Schumacher, J.C., Bodnar, R.J. and Kendall, J.F., 2021. Insight Into the Early Exhumation of the Cycladic Blueschist Unit, Syros, Greece: Combined Application of Zoned Garnet Geochronology, Thermodynamic Modeling, and Quartz Elastic Barometry: Geochemistry, Geophysics, Geosystems, v. 22(8), p.e2021GC009716.

Grasemann, B., Schneider, D.A., Stöckli, D.F., and Iglseder, C., 2012, Miocene bivergent crustal extension in the Aegean: Evidence from the western Cyclades (Greece): Lithosphere, v. 4, no. 1, p. 23–39, https://doi.org/10.1130/L164.1.

Hämmerli, J., Kemp, A., Shimura, T., Vervoort, J.D., EIMF, and Dunkley, D.J., 2018, Generation of I-type granitic rocks by melting of heterogeneous lower crust: Geology, v. 46, no. 10, p. 907–910, https://doi.org/10.1130/G45119.1.

Harris, N., and Massey, J., 1994, Decompression and anatexis of Himalayan metapelites: Tectonics, v. 13, p. 1537–1546, https://doi.org/10.1029/94TC01611.

DOI:10.1130/B36489.1

Healy, B., Collins, W.J., and Richards, S.W., 2004, A hybrid origin for Lachlan S-type granites: the Murrumbidgee Batholith example: Lithos, v. 78, no. 1–2, p. 197–216, https://doi.org/10.1016/j.lithos.2004.04.047.

Hejl, E., Riedl, H., and Weingartner, H., 2002, Post-plutonic unroofing and morphogenesis of the Attic–Cycladic complex (Aegea, Greece): Tectonophysics, v. 349, p. 37–56, https://doi.org/10.1016/S0040-1951(02)00045-8.

Hinsken, T., Bröcker, M., Strauss, H., and Bulle, F., 2017, Geochemical, isotopic and geochronological characterization of listvenite from the Upper Unit on Tinos, Cyclades, Greece: Lithos, v. 282–283, p. 281–297, https://doi.org/10.1016/j.lithos.2017.02.019.

Hopkinson, T., Harris, N.B.W., Warren, C.J., Spencer, C.J., Roberts, N.M.W., Horstwood, M.S.A., and Parrish, R.R., 2017, The identification and significance of pure sediment-derived granites: Earth and Planetary Science Letters, v. 467, p. 57–63, https://doi.org/10.1016/j.epsl.2017.03.018.

Houseman, G.A., and Molnar, P., 1997, Gravitational (Rayleigh–Taylor) instability of a layer with non-linear viscosity and convective thinning of continental lithosphere: Geophysical Journal International, v. 128, p. 125–150, https://doi.org/10.1111/j.1365-246X.1997.tb04075.x.

Iglseder, C., Grasemann, B., Schneider, D.A., Petrakakis, K., Miller, C., Klötzli, U.S., et al., 2009, I and S-type plutonism on Serifos (W-Cyclades, Greece): Tectonophysics, v. 473, no. 1–2, p. 69–83, https://doi.org/10.1016/j.tecto.2008.09.021.

Jansen, J.B.H., 1973. Geological map of Greece, Island of Naxos (1: 50,000). Institute for Geology and Mineral Resources, Athens.

Jansen, J.B.H., and Schuiling, R.D., 1976, Metamorphism on Naxos; petrology and geothermal gradients: American Journal of Science, v. 276, no. 10, p. 1225–1253, https://doi.org/10.2475/ajs.276.10.1225.

Jolivet, L., 2001. A comparison of geodetic and finite strain pattern in the Aegean, geodynamic implications. Earth and Planetary science letters, v. 187(1-2), p. 95-104.

Jolivet, L., and Brun, J.P., 2010, Cenozoic geodynamic evolution of the Aegean region: International Journal of Earth Sciences, v. 99, p. 109–138, https://doi.org/10.1007/s00531-008-0366-4.

Jolivet, L., Famin, V., Mehl, C., Parra, T., Aubourg, C., Hébert, R., Philippot, P., Whitney, D.L. and Teyssier, C., 2004. Strain localization during crustal-scale boudinage to form extensional metamorphic domes in the Aegean Sea. Special papers-Geological Society of America, pp.185-210.

Jolivet, L., Lecomte, E., Huet, B., Denèle, Y., Lacombe, O., Labrousse, L., Le Pourhiet, L., and Mehl, C., 2010, The north cycladic detachment system: Earth and Planetary Science Letters, v. 289, p. 87–104, https://doi.org/10.1016/j.epsl.2009.10.032.

Jolivet, L., Faccenna, C., Huet, B., Labrousse, L., Le Pourhiet, L., Lacombe, O., Lecomte, E., Burov, E., Denèle, Y., Brun, J.P. and Philippon, M., 2013. Aegean tectonics: Strain localisation, slab tearing and trench retreat. Tectonophysics, v. 597, p.1-33.

Jolivet, L. et al., 2015, The geological signature of a slab tear below the Aegean: Tectonophysics, v. 659, p. 166–182, https://doi.org/10.1016/j.tecto.2015.08.004.

Jolivet, L., Sautter, V., Moretti, I., Vettor, T., Papadopoulou, Z., Augier, R., Denèle, Y., and Arbaret, L., 2021, Anatomy and evolution of a migmatite-cored extensional metamorphic dome and interaction with syn-kinematic intrusions, the Mykonos-Delos-Rheneia MCC: Journal of Geodynamics, v. 144, p. 101824, https://doi.org/10.1016/j.jog.2021.101824.

Jung, S., and Pfänder, J.A., 2007, Source composition and melting temperatures of orogenic granitoids: constraints from CaO/Na_2O, Al_2O_3/TiO_2 and accessory mineral saturation thermometry: European Journal of Mineralogy, v. 19, no. 6, p. 859–870, https://doi.org/10.1127/0935-1221/2007/0019-1774.

Katzir, Y., Matthews, A., Garfunkel, Z., Schliestedt, M., and Avigad, D., 1996, The tectono-metamorphic evolution of a dismembered ophiolite (Tinos, Cyclades, Greece): Geological Magazine, v. 133, p. 237–254, https://doi.org/10.1017/S0016756800008992.

Keay, S., 1998. The geological evolution of the Cyclades, Greece: constraints from SHRIMP U–Pb geochronology. *Ph.D. thesis, Australian National University, Canberra*, 335 pp.

Keay, S., Collins, W.J., and McCulloch, M.T., 1997, A three-component Sr-Nd isotopic mixing model for granitoid genesis, Lachlan fold belt, eastern Australia: Geology, v. 25, no. 4, p. 307–310, https://doi.org/10.1130/0091-7613(1997)025<0307:ATCSNI>2.3.CO;2.

Keay, S., Lister, G., and Buick, I., 2001, The timing of partial melting, Barrovian metamorphism and granite intrusion in the Naxos metamorphic core complex, Cyclades, Aegean Sea, Greece: Tectonophysics, v. 342, p. 275–312, https://doi.org/10.1016/S0040-1951(01)00168-8.

Keiter, M., Ballhaus, C., and Tomaschek, F., 2011, A new geological map of the Island of Syros (Aegean Sea, Greece): Implications for lithostratigraphy and structural history of the Cycladic Blueschist Unit: Geological Society of America. Special Paper, v. 481, p. 1–43.

Kirchenbaur, M., Münker, C., Schuth, S., Garbe-Schönberg, D. and Marchev, P., 2012. Tectonomagmatic constraints on the sources of Eastern Mediterranean K-rich lavas. Journal of Petrology, v. 53(1), p. 27–65.

Kissel, C., and Laj, C., 1988, The Tertiary geodynamical evolution of the Aegean arc: A paleomagnetic reconstruction: Tectonophysics , v. 146, p. 183–201, doi:10.1016/0040-1951(88)90090-X.

Klaver, M., Carey, S., Nomikou, P., Smet, I., Godelitsas, A. and Vroon, P., 2016. A distinct source and differentiation history for Kolumbo submarine volcano, Santorini volcanic field, Aegean arc. Geochemistry, Geophysics, Geosystems, v. 17(8), p. 3254–3273.

Kruckenberg, S.C., Vanderhaeghe, O., Ferré, E.C., Teyssier, C., and Whitney, D.L., 2011, Flow of partially molten crust and the internal dynamics of a migmatite dome, Naxos, Greece: Tectonics, v. 30, p. TC3001, https://doi.org/10.1029/2010TC002751.

Kokkalas, S., and Aydin, A., 2013, Is there a link between faulting and magmatism in the south-central Aegean Sea?: Geological Magazine, v. 150, no. 2, p. 193–224, https://doi.org/10.1017/S0016756812000453.

Kokkalas, S., Xypolias, P., Koukouvelas, I., and Doutsos, T., 2006, Postcollisional contractional and extensional deformation in the Aegean region: Geological Society of America. Special Paper, v. 409, p. 97, https://doi.org/10.1130/0-8137-2409-0.97.

Koukouvelas, I.K., and Kokkalas, S., 2003, Emplacement of the Miocene west Naxos pluton (Aegean Sea, Greece): A structural study: Geological Magazine, v. 140, p. 45–61, https://doi.org/10.1017/S0016756802007094.

Koutsovitis, P., Soukis, K., Voudouris, P., Lozios, S., Ntaflos, T., Stouraiti, C., and Koukouzas, N., 2021, The Late Cretaceous magmatic arc of the south Aegean: Geodynamic implications from petrological and geochemical studies of granitoids from Anafi Island (Cyclades – Greece): International Geology Review, https://doi.org/10.1080/00206814.2021.1884906.

Kuhlemann, F., Frisch, W., Dunkl, I., Kázmér, M. and Schmiedl, G., 2004. Miocene siliciclastic deposits of Naxos Island: Geodynamic and environmental implications for the evolution of the southern Aegean Sea (Greece). In: Detrital Thermochronology – Provenance Analysis, Exhumation, and Landscape Evolution of Mountain Belts.

DOI:10.1130/B36489.1

Geological Society of America, Special Paper v. 378. Geological Society of America, Boulder, CO, p. 51–65.

Lagos, M., Scherer, E.E., Tomaschek, F., Munker, C., Keiter, M., et al., 2007, High precision Lu–Hf geochronology of Eocene eclogite-facies rocks from Syros, Cyclades, Greece: Chemical Geology, v. 243, p. 16–35, https://doi.org/10.1016/j.chemgeo.2007.04.008.

Lamont, T.N., 2018, Unravelling the structural, metamorphic and strain history of the "Aegean Orogeny", Southern Greece, with a combined structural, petrological and geochronological approach, *PhD thesis, University of Oxford, Oxford, UK.*

Lamont, T.N., Searle, M.P., Roberts, N.M.W., Waters, D.J., Palin, R.M., Smye, A.J., Dyck, B., Gopon, P., Weller, O.M., and St-Onge, M., 2019, Compressional origin to the Naxos metamorphic core complex: Structure, petrography and thermobarometry: Geological Society of America Bulletin, v. 132, p. 149–197, https://doi.org/10.1130/B31978.1.

Lamont, T. N., Roberts, N. M. W., Searle, M. P., Gopon, P., Waters, D. J., & Millar, I., 2020a. The age, origin and emplacement of the Tsiknias Ophiolite, Tinos, Greece: Tectonics, v. 39, e2019TC005677. https://doi.org/https://doi.org/10.1029/2019TC005677

Lamont, T. N., Searle, M. P., Gopon, P., Roberts, N. M. W., Wade, J., Palin, R. M., & Waters, D. J.,2020b. The Cycladic Blueschist Unit on Tinos, Greece: Cold NE subduction and SW directed extrusion of the Cycladic continental margin under the Tsiknias Ophiolite: Tectonics, v. 39, e2019TC005890. https://doi.org/10.1029/2019TC005890

Lamont, T. N., Smye, A. J., Roberts, N. M. W., Searle, M. P., Waters, D. J., and White, R. W., (In Press). Constraints on the thermal evolution of metamorphic core complexes from the timing of high-pressure metamorphism on Naxos, Greece: Geological Society of America Bulletin.

Laurent, V., Beaudoin, A., Jolivet, L., Arbaret, L., Augier, R., Rabillard, A. and Menant, A., 2015. Interrelations between extensional shear zones and synkinematic intrusions: The example of Ikaria Island (NE Cyclades, Greece). Tectonophysics, v. 651, p. 152-171.

Laurent, V., Jolivet, L., Roche, V., Augier, R., Scaillet, S., Cardello, G.L., et al., 2016, Strain localization in a fossilized subduction channel: Insights from the Cycladic Blueschist Unit (Syros, Greece): Tectonophysics, v. 672–673, p. 150–169, https://doi.org/10.1016/j.tecto.2016.01.036.

Law, R.D., Searle, M.P., and Godin, L., 2006, Channel flow, ductile extrusion and exhumation in continental collision zones: Geological Society of London, Special Publications, v. 268, https://doi.org/10.1144/GSL.SP.2006.268.01.28.

Le Fort, P., Cuney, M., Deniel, C., France-Lanord, C., Sheppard, S.M.F., Upreti, B.N., and Vidal, P., 1987, Crustal generation of the Himalayan leucogranites: Tectonophysics, v. 134, p. 39–57, https://doi.org/10.1016/0040-1951(87)90248-4.

Le Pichon, X., and Angelier, J., 1979, The Hellenic arc and trench system: A key to the neotectonic evolution of the Eastern Mediterranean area: Tectonophysics, v. 60, p. 1–42, https://doi.org/10.1016/0040-1951(79)90131-8.

Le Pichon, X., and Angelier, J., 1981, The Aegean Sea: Philosophical Transactions of the Royal Society of London, v. 300, p. 357–372, https://doi.org/10.1098/rsta.1981.0069.

Le Pichon, X., Lallemant, S.J., Chamot-Rooke, N., Lemeur, D., and Pascal, G., 2002, The Mediterranean Ridge backstop and the Hellenic nappes: Marine Geology, v. 186, no. 1–2, p. 111–125, https://doi.org/10.1016/S0025-3227(02)00175-5.

Lee, J., and Lister, G.S., 1992, Late Miocene ductile extension and detachment faulting, Mykonos, Greece: Geology, v. 20, no. 2, p. 121–124, https://doi.org/10.1130/0091-7613(1992)020<0121:LMDEAD>2.3.CO;2.

Lederer, G.W., Cottle, J.M., Jessup, M.J., Langille, J.M., and Ahmad, T., 2013, Timescales of partial melting in the Himalayan middle crust: insight from the Leo Pargil dome, northwest India: Contributions to Mineralogy and Petrology, v. 166, no. 5, p. 1415–1441, https://doi.org/10.1007/s00410-013-0935-9.

Liati, A., Skarpelis, N., and Pe-Piper, G., 2009, Late Miocene magmatic activity in the Attic-Cycladic Belt of the Aegean (Lavrion, SE Attica, Greece): implications for the geodynamic evolution and timing of ore deposition: Geological Magazine, v. 146, no. 5, p. 732–742, https://doi.org/10.1017/S0016756809006438.

Lister, G.S., Banga, G., and Feenstra, A., 1984, Metamorphic core complexes of cordilleran type in the Cyclades, Aegean Sea, Greece: Geology, v. 12, p. 221–225, https://doi.org/10.1130/0091-7613(1984)12<221:MCCOCT>2.0.CO;2.

London, D. 2016, Rare-element granitic pegmatites.

Loucks, R.R., 2021. Deep entrapment of buoyant magmas by orogenic tectonic stress: Its role in producing continental crust, adakites, and porphyry copper deposits. Earth-Science Reviews, 220, p.103744.

Ludwig, K.R., 2011, Isoplot: A Plotting and Regression Program for Radiogenic Isotope Data. Version 4.13-March 2011. US Geological Survey Open-File Report, 445.

Mancktelow, N., Zwingmann, H., and Mulch, A., 2016, Timing and conditions of clay fault gouge formation on the Naxos detachment (Cyclades, Greece): Tectonics, v. 35, p. 2334–2344, https://doi.org/10.1002/2016TC004251.

Martin, L., Duchêne, S., Deloule, E., and Vanderhaeghe, O., 2006, The isotopic composition of zircon and garnet: a record of the metamorphic history of Naxos, Greece: Lithos, v. 87, no. 3–4, p. 174–192, https://doi.org/10.1016/j.lithos.2005.06.016.

Mastrakas, N., and St. Seymour, K., 2000, Geochemistry of Tinos granite: A window to the Miocene microplate tectonics of the Aegean region: Neues Jahrbuch für Mineralogie. Abhandlungen, p. 295–315, https://doi.org/10.1127/njma/175/2000/295.

Matsuda, J., Senoh, K., Maruoka, T., Sato, H., and Mitropoulos, P., 1999, K-Ar ages of the Aegean volcanic rocks and their implication for the arc-trench system: Geochemical Journal, v. 33, p. 369–377, https://doi.org/10.2343/geochemj.33.369.

McGrath, A., Stouraiti, C., and Windley, B., 2017, Geochemistry of mylonitic gneisses from the Cycladic Basement Unit (Paros and Serifos, Aegean Sea): implications for protoliths of the high-grade gneisses [Geol Rundsch]: International Journal of Earth Sciences, v. 106, p. 2067–2089, https://doi.org/10.1007/s00531-016-1414-0.

Means, W.D., 1989, Stretching faults: Geology, v. 17, p. 893–896, https://doi.org/10.1130/0091-7613(1989)017<0893:SF>2.3.CO;2.

Mehl, C., Jolivet, L., and Lacombe, O., 2005, From ductile to brittle: Evolution and localization of deformation below a crustal detachment (Tinos, Cyclades, Greece): Tectonics, v. 24, no. 4, p. TC4017, https://doi.org/10.1029/2004TC001767.

Melidonis, N.G., 1980, The geological structure and mineral deposits of Tinos island (Cyclades, Greece): Geolical society of Greece, v. 13, p. 1–80.

Menant, A., Jolivet, L., Augier, R., and Skarpelis, N., 2013, The North Cycladic Detachment System and associated mineralization, Mykonos, Greece: Insights on the evolution of the Aegean domain: Tectonics, v. 32, p. 433–452, https://doi.org/10.1002/tect.20037.

Meulenkamp, J.E., Wortel, M.J.R., Van Wamel, W.A., Spakman, W., and Strating, E.H., 1988, On the Hellenic subduction zone and the geodynamic evolution of Crete since the late Middle Miocene: Tectonophysics, v. 146, no. 1–4, p. 203–215, https://doi.org/10.1016/0040-1951(88)90091-1.

Moyen, J.F., Janoušek, V., Laurent, O., Bachmann, O., Jacob, J.B., Farina, F., Fiannacca, P. and Villaros, A., 2021. Crustal melting vs. fractionation of basaltic magmas: Part 1, granites and paradigms. Lithos, v. 402, p.106291.

Orejana, D., Villaseca, C., Valverde-Vaquero, P., Belousova, E.A. and Armstrong, R.A., 2012. U–Pb geochronology and zircon composition of late Variscan S-and I-type

DOI:10.1130/B36489.1

granitoids from the Spanish Central System batholith. International Journal of Earth Sciences, v. 101(7), p.1789–1815.

Papanikolaou, D., 1984a, Three metamorphic belts of the Hellinides: a review and a kinematic interpretation: Geological Society of London Special Publication, v. 17, p. 551–556.

Papanikolaou, D., 1984b.Tectoic evolution of the Cycladic Blueschist belt (Aegean Sea, Greece): Chemical transport in metasomatic processes. P. 429–450.

Papanikolaou, D., 2013, Tectonostratigraphic models of the alpine terranes and subduction history of the Hellinides: Tectonophysics, v. 595–596, p. 1–24, https://doi.org/10.1016/j.tecto.2012.08.008.

Papanikolaou, D. and Vassilakis, E., 2010. Thrust faults and extensional detachment faults in Cretan tectono-stratigraphy: Implications for Middle Miocene extension. Tectonophysics, v. 488(1-4), p. 233–247.

Patiño Douce, A.E., 1997, Generation of metaluminous A-type granites by low-pressure melting of calc-alkaline granitoids: Geology, v. 25, no. 8, p. 743–746, https://doi.org/10.1130/0091-7613(1997)025<0743:GOMATG>2.3.CO;2.

Patiño Douce, A.E., and Johnston, A.D., 1991, Phase equilibria and melt productivity in the pelitic system: Implications for the origin of peraluminous granitoids and aluminous granulites: Contributions to Mineralogy and Petrology, v. 107, p. 202–218, https://doi.org/10.1007/BF00310707.

Patiño Douce, A.E., and Harris, N., 1998, Experimental Constraints on Himalayan Anatexis: Journal of Petrology, v. 39, p. 689–710, https://doi.org/10.1093/petroj/39.4.689.

Patiño Douce, A.E., and McCarthy, T.C., 1998. Melting of crustal rocks during continental collision and subduction, *in When continents collide: geodynamics and geochemistry of ultrahigh-pressure rocks*, edited by Nicolas, A., p. 27–55. Springer, Dordrecht, https://doi.org/10.1007/978-94-015-9050-1_2.

Patzak, M., Okrusch, M., and Kreuzer, H., 1994, The Akrotiri Unit on the island of Tinos, Cyclades, Greece: witness to a lost terrane of Late Cretaceous age: Neues Jahrbuch für Geologie und Paläontologie. Abhandlungen, v. 194, p. 211–252, https://doi.org/10.1127/njgpa/194/1994/211.

Pearson, D.G., Shirey, S.B., Carlson, R.W., Boyd, F.R., Pokhilenko, N.P., and Shimizu, N., 1995, Re-Os, Sm-Nd, and Rb-Sr isotope evidence for thick Archaean lithospheric mantle beneath the Siberian craton modified by multistage metasomatism: Geochimica et Cosmochimica Acta, v. 59, p. 959–977, https://doi.org/10.1016/0016-7037(95)00014-3.

Peillod, A., Ring, U., Glodny, J., and Skelton, A., 2017, An Eocene/Oligocene blueschist/greenschist-facies P-T loop from the Cycladic Blueschist Unit on Naxos Island, Greece: Deformation-related reequilibration vs thermal relaxation: Journal of Metamorphic Geology, v. 35, p. 805–830, https://doi.org/10.1111/jmg.12256.

Peillod, A., Majka, J., Ring, U., Drüppel, K., Patten, C., Karlsson, A., Włodek, A., and Tehler, E., 2021, Differences in decompression of a high-pressure unit: A case study from the Cycladic Blueschist Unit on Naxos Island, Greece: Lithos, v. 386-387, p. 106043, https://doi.org/10.1016/j.lithos.2021.106043.

Pe-Piper, G., 2000, Origin of S-type granites coeval with I-type granites in the Hellenic subduction system, Miocene of Naxos, Greece. *European Journal of Mineralogy*, v. 12 (4), p. 859–875.

Pe-piper, G. and Piper, D.J., 1989. Spatial and temporal variation in Late Cenozoic back-arc volcanic rocks, Aegean Sea region. Tectonophysics, v. 169(1-3), p.113–134.

Pe-Piper, G. and Piper, D.J.W., 1993. Revised stratigraphy of the Miocene volcanic rocks of Lesbos, Greece. Neues Jahrbuch für Geologie und Paläontologie-Monatshefte, p. 97–110.

Pe-Piper, G., and Hatzipanagiotou, K., 1997. The Pliocene volcanic rocks of Crommyonia, western Greece and their implications for the early evolution of the South Aegean arc: Geological Magazine, v. 134, no. 1, p. 55–66, https://doi.org/10.1017/S0016756897006390.

Pe-Piper, G., and Moulton, B., 2008, Magma evolution in the Pliocene–Pleistocene succession of Kos, Southern Aegean arc (Greece): Lithos, v. 106, p. 110–124, https://doi.org/10.1016/j.lithos.2008.07.002.

Pe-Piper, G., and Piper, D., 2005, The South Aegean active volcanic arc: Relationships between magmatism and tectonics: Dev. V. canol., v. 7, p. 113–133.

Pe-Piper, G., Kotopouli, C.N., and Piper, D.J.W., 1997, Granitoid rocks of Naxos, Greece: regional geology and petrology: Geological Journal, v. 32, p. 153–171, https://doi.org/10.1002/(SICI)1099-1034(199706)32:2<153::AID-GJ737>3.0.CO;2-1.

Pe-Piper, G., Piper, D.J.W., and Matarangas, D., 2002, Regional implications of geochemistry and style of emplacement of Miocene I-type diorite and granite, Delos, Cyclades, Greece: Lithos, v. 60, p. 47–66, https://doi.org/10.1016/S0024-4937(01)00068-8.

Pe-Piper, G., Zhang, Y., Piper, D.J. and Prelević, D., 2014. Relationship of Mediterranean type lamproites to large shoshonite volcanoes, Miocene of Lesbos, NE Aegean Sea. Lithos, v. 184, p. 281–299.

Philippon, M., Brun, J.P., Gueydan, F., and Sokoutis, D., 2014, The interaction between Aegean back-arc extension and Anatolia escape since Middle Miocene: Tectonophysics, v. 631, p. 176–188, https://doi.org/10.1016/j.tecto.2014.04.039.

Platt, J., and England, P., 1994, Convective removal of lithosphere beneath mountain belts – thermal and mechanical consequences: American Journal of Science, v. 294, no. 3, p. 307–336, https://doi.org/10.2475/ajs.294.3.307.

Rabillard, A., Jolivet, L., Arbaret, L., Bessiere, E., Laurent, V., Menant, A., et al., 2018, Synextensional granitoids and detachment systems within Cycladic metamorphic core complexes (Aegean Sea, Greece): Toward a regional tectonomagmatic model: Tectonics, v. 37, p. 2328–2362, https://doi.org/10.1029/2017TC004697.

Ring, U., Thomson, S.N., and Bröcker, M., 2003, Fast extension but little exhumation: the Vari detachment in the Cyclades, Greece: Geological Magazine, v. 140, no. 3, p. 245–252, https://doi.org/10.1017/S0016756803007799.

Ring, U., Glodny, J., Will, T. and Thomson, S., 2010. The Hellenic subduction system: high-pressure metamorphism, exhumation, normal faulting, and large-scale extension. Annual Review of Earth and Planetary Sciences, v. 38(1), p. 45–76.

Ring, U., Glodny, J., Peillod, A., and Skelton, A., 2018. The timing of high-temperature conditions and ductile shearing in the footwall of the Naxos extensional fault system, Aegean Sea, Greece: Tectonophysics, v. 745, p. 366–381, https://doi.org/10.1016/j.tecto.2018.09.001.

Roberts, N.M.W., Thomas, R.J., and Jacobs, J., 2016, Geochronological constraints on the metamorphic sole of the Semail ophiolite in the United Arab Emirates: Geoscience Frontiers, v. 7, p. 609–619, https://doi.org/10.1016/j.gsf.2015.12.003.

Rosenberg, C.L., and Handy, M.R., 2005, Experimental deformation of partially melted granite revisited: implications for the continental crust: Journal of Metamorphic Geology, v. 23, no. 1, p. 19–28, https://doi.org/10.1111/j.1525-1314.2005.00555.x.

Royden, L.H., 1993. Evolution of retreating subduction boundaries formed during continental collision. Tectonics, v. 12(3), p. 629–638.

Royden, L.H. and Papanikolaou, D.J., 2011. Slab segmentation and late Cenozoic disruption of the Hellenic arc. Geochemistry, Geophysics, Geosystems, v. 12(3).

DOI:10.1130/B36489.1

Rudnick, R. L., Gao, S., Holland, H. D., and Turekian, K. K., 2003. Composition of the continental crust: Treatise on geochemistry, The crust, v. 3, p. 1–64.

Schellart, W.P., Lister, G.S., Sussman, A.J. and Weil, A.B., 2004. Tectonic models for the formation of arc-shaped convergent zones and backarc basins. Orogenic curvature: integrating paleomagnetic and structural analyses, v. 383, p. 237–258.

Searle, M.P., 2010. Low-angle normal faults in the compressional Himalayan orogen; Evidence from the Annapurna–Dhaulagiri Himalaya, Nepal. Geosphere, v. 6(4), p. 296–315.

Searle, M.P., and Lamont, T.N., 2019, Compressional metamorphic core complexes, low-angle normal faults and extensional fabrics in compressional tectonic settings: Geological Magazine, v. 157 , p. 101–118.

Searle, M.P., and Lamont, T.N., 2022, Compressional origin of the Aegean Orogeny, Greece: Geoscience Frontiers, v. 13, p. 101049, https://doi.org/10.1016/j.gsf.2020.07.008.

Seward, D., Vanderhaeghe, O., Siebenaller, L., Thomson, S., Hibsch, C., Zingg, A., Holzner, P., Ring, U. and Duchêne, S., 2009. Cenozoic tectonic evolution of Naxos Island through a multi-faceted approach of fission-track analysis. Geological Society, London, Special Publications, v. 321(1), p.179-196.

Smithies, R.H., Champion, D.C., and Van Kranendonk, M.J., 2009, Formation of Paleoarchean continental crust through infracrustal melting of enriched basalt: Earth and Planetary Science Letters, v. 281, p. 298–306, https://doi.org/10.1016/j.epsl.2009.03.003.

Soder, C., Altherr, R., and Romer, R.L., 2016, Mantle Metasomatism at the Edge of a Retreating Subduction Zone: Late Neogene Lamprophyres from the Island of Kos, Greece: Journal of Petrology, v. 57, p. 1705–1728, https://doi.org/10.1093/petrology/egw054.

Stacey, J.T. and Kramers, 1., 1975. Approximation of terrestrial lead isotope evolution by a two-stage model. Earth and planetary science letters, v. 26(2), p. 207–221.

Stouraiti, C., Mitropoulos, P., Tarney, J., Barreiro, B., McGrath, A.M., and Baltatzis, E., 2010, Geochemistry and petrogenesis of late Miocene granitoids, Cyclades, southern Aegean: nature of source components: Lithos, v. 114, no. 3–4, p. 337–352, https://doi.org/10.1016/j.lithos.2009.09.010.

Stouraiti, C., Baziotis, I., Asimow, P.D., and Downes, H., 2018. Geochemistry of the Serifos calc-alkaline granodiorite pluton, Greece: constraining the crust and mantle contributions to I-type granitoids [Geol Rundsch]: International Journal of Earth Sciences, v. 107, p. 1657–1688, https://doi.org/10.1007/s00531-017-1565-7.

Sun, S.S., and McDonough, W.F., 1989. Chemical and isotopic systematics of oceanic basalts: implications for mantle composition and process. In: Saunders, A. D. and Norry, J. M. (eds) Magmatism in the Ocean Basins: Geological Society of London Special Publication, v. 42, p. 313–345, https://doi.org/10.1144/GSL.SP.1989.042.01.19.

Sylvester, P.J., 1998, Post-collisional strongly peraluminous granites: Lithos, v. 45, no. 1–4, p. 29–44, https://doi.org/10.1016/S0024-4937(98)00024-3.

Taylor, S.R. and McLennan, S.M., 1985. The continental crust: its composition and evolution.

Tomaschek, F., Kennedy, A.K., Villa, I.M., Lagos, M., and Ballhaus, C., 2003, Zircons from Syros, Cyclades, Greece—Recrystallization and mobilization of zircon during high-pressure metamorphism: Journal of Petrology, v. 44, p. 1977–2002, https://doi.org/10.1093/petrology/egg067.

Tual, L., Smit, M., Cutts, J., Kooijman, E., Kielman-Schmitt, M., Majka, J., and Foulds, I., 2022, Rapid, paced metamorphism of blueschists (Syros, Greece) from laser-based zoned Lu-Hf garnet chronology and LA-ICPMS trace element mapping: Chemical Geology, v. 607, p. 121003, https://doi.org/10.1016/j.chemgeo.2022.121003.

Urai, J.L., Schuiling, R.D., and Jansen, J.B.H., 1990, Alpine deformation on Naxos (Greece), *in* Knipe, R.J., and Rutter, E.H., eds., Deformation Mechanisms, Rheology and Tectonics: Geological Society of London Special Publication, v. 54, p. 509–522.

Vanderhaeghe, O., 2004, Structural development of the Naxos migmatite dome, *in* Whitney, D.L., Teyssier, C., and Siddoway, C.S., eds., *Gneiss Domes in Orogeny:* Geological Society of America Special Paper, v. 380, p. 211–227, https://doi.org/10.1130/0-8137-2380-9.211.

van Hinsbergen, D. J. J., and Schmid, S. M., 2012, Map view restoration of Aegean–West Anatolian accretion and extension since the Eocene, Tectonics, v. 31, TC5005, doi:10.1029/2012TC003132.

Vermeesch, P., 2018, IsoplotR: a free and open toolbox for geochronology: Geoscience Frontiers, v. 9, p. 1479–1493, https://doi.org/10.1016/j.gsf.2018.04.001.

Villa, I.M., Holden, N.E., Possolo, A., Ickert, R.B., Hibbert, D.B., and Renne, P.R., 2020, IUPAC-IUGS recommendation on the half-lives of 147Sm and 146Sm: Geochimica et Cosmochimica Acta, v. 285, p. 70–77, https://doi.org/10.1016/j.gca.2020.06.022.

Virgo, S., von Hagke, C., and Urai, J.L., 2018, 2018, Multiphase boudinage: A case study of amphibolites in marble in the Naxos migmatite core: Solid Earth, v. 9, p. 91–113, https://doi.org/10.5194/se-9-91-2018.

Von Hagke, C., Bamberg, B., Virgo, S., and Urai, J.L., 2018, Outcrop-scale tomography: Insights into the 3D structure of multiphase boudins: Journal of Structural Geology, v. 115, p. 311–317, https://doi.org/10.1016/j.jsg.2018.02.014.

Wijbrans, J.R., and McDougall, I., 1988, Metamorphic evolution of the Attic Cycladic Metamorphic Belt on Naxos (Cyclades, Greece) utilizing 40Ar/39Ar age spectrum measurements: Journal of Metamorphic Geology, v. 6, no. 5, p. 571–594, https://doi.org/10.1111/j.1525-1314.1988.tb00441.x.

Yang, L., Liu, X.C., Wang, J.M., and Wu, F.U., 2019, Is Himalayan leucogranite a product by in situ partial melting of the Greater Himalayan Crystalline? A comparative study of leucosome and leucogranite from Nyalam, southern Tibet: Lithos, v. 342–343, p. 542–556, https://doi.org/10.1016/j.lithos.2019.06.007.

Zeffren, S., Avigad, D., Heimann, A., and Gvirtzman, Z., 2005, Age resetting of hanging wall rocks above a low-angle detachment fault: Tinos Island (Aegean Sea): Tectonophysics, v. 400, p. 1–25, https://doi.org/10.1016/j.tecto.2005.01.003.

Figure 1. A) Summary tectonic map of the Aegean region showing the major structures and tectono-stratigraphic units. B) Location map summarizing the reported U–Pb ages of Cycladic granites and volcanics with new ages from this study; NCDS = North Cycladic Detachment System, NPDS = Naxos-Paros Detachment System and WCDS = West Cycladic Detachment System. References: (1) Bolhar et al., (2010); (2) Brichau et al., (2008); (3) Keay et al., (2001); (4) Brichau et al., (2007); (5) Iglseder et al., (2009); (6) Matsuda et al., (1999; Ar–Ar volcanics), (7) Beauodin et al., 2015; (9) Lamont, (2018).

Figure 2. Geological map of Tinos with sample locations and U–Pb ages and Cross-section showing the cross-cutting relationships of the granites and the NCDS and field photographs. Cross-cutting relations of Tinos Granites: A and B) Domino normal faults at Livada Bay that cross-cut the garnet bearing leucogranite sills (N37.612165, E25.242085)

Figure 3. Outcrop photographs and cross-cutting relationships of the Tinos granitoids: A) 17TL05 dacite dyke intruding Kionnia Bay (N37.553493, E25.134870), B) Dacite dyke weakly deformed east of Kolimpithra Bay (N37.628227, E25.164213), C) 17TL36 undeformed dacite dyke intruding the Tsiknias Ophiolite (N37.580870, E25.234811). D) Tinos Monzogranite intruding into the amphibolites of the metamorphic sole, foliation in amphibolites shows top-to-SW shear (N37.609699, E25.238379), E) Undeformed Tinos monzogranite pluton in center of the island. F) 17TL100 cross-cutting leucogranite through

DOI:10.1130/B36489.1

the Tinos monzogranite pluton (N37.610454, E25.236740). G) Western edge of the Tinos monzogranite pluton (N37.577060, E25.167255). H) 17TL36 cross polarized thin section photomicrograph of dacite dyke with rounded plagioclase phenocrysts. I) TLTN34 deformed monzogranite (N37.582920, E25.175475). J) TLTN34 deformed monzogranite with dynamic recrystallization of quartz. K and L) Livada Bay normal faults showing possible faulting during leucogranite crystallization (N37.613040, E25.244052). M) TLTN13 plane polarized photomicrograph showing the garnet plagioclase muscovite assemblage, with fractured garnet associated with brittle deformation.

Figure 4. Geological map of Mykonos and Delos with sample locations, cross section and field photographs of leucogranites and low angle normal faults after Menant et al., (2013) and our own mapping. A) Mykonos Detachment and Livada Detachment at Cape Evros (N37.471922, E25.460290). The Mykonos Detachment places silicified sediments onto metamorphic sole amphibolites, whereas the structurally deeper Livada Detachment cuts the top of the Mykonos granite and is associated with solid state mylonitization of the granite. B) Delos S-type leucogranite sill intrusing sillimanite grade gneisses. C) The Livada Detchment at Fokos Bay, Mykonos (N37.483252, E25.406609) dipping ~10° to the NE placing the metamorphic sole amphibolites onto mylonitised Mykonos Granite. D) Outcrop photograph of sample 17TL95 Delos Tourmaline-biotite leucogranite on Delos (N37.406523, E25.266933).

Figure 5. Geological map of Naxos and cross sections after Lamont et al., (2019); Kruckenberg et al., (2011); Jansen and Schuiling, (1976) showing leucogranite sample locations and the geometries of the Koronos Shear Zone (KSZ), Zas Shear Zone (ZSZ) folded about the migmatite dome and cut by the Naxos-Paros Detachment (NPDS), particularly on the western margin of the core complex.

Figure 6. Outcrop photographs of Naxos cross-cutting granites and ductile shear zones. A) Sample TL72 leucogranite sheared into alignment with the Naxos-Paros Detachment System on the NW coast of Naxos, also note the sheared ultramafic lense downthrown from the overlying thrust sheet (N37.183593, E25.506738), B) Sample TLN8 from a vertically orientated leucogranite from the Core High Strain Zone (CHSZ) at the center of the migmatite dome/Core Unit, affected by vertical boudinage (N37.106069, E25.482802). C) TL63 from a steeply dipping dyke (190/80 W) along the western margin of the migmatite dome that cross-cuts shearing on the Koronos Shear Zone but is aligned into the steeply dipping Naxos-Paros Detachment near the village of Kourounochori (N37.094362, E25.443100). D) Sample 17TL106 from a folded aplite in the West Naxos Granodiorite near the village of Glinado (N37.075359, E25.399717) fold trending NNE-SSW. E) Sample TLN10 (N37.106169, E25.482779) leucogranite intruding marble and amphibolite trending NNE-SSW affected by horizontal NNE-SSW boudinage. F) S–C' mylonites in the Variscan orthogneiss basement from the Koronos Shear Zone on the south east margin of the migmatite dome (N37.048814, E25.455936). G) Sample TL58 leucogranite dyke cross cutting the top-to-NNE shear fabrics on the Koronos Shear Zone on the eastern margin of the migmatite dome (N37.118726 E25.527931).

Figure 7. Granite classification diagrams after Frost, (2001). A) QAPF diagram for siliceous igneous rocks, B) Aluminum saturation index (ASI) vs A/NK, C) Modified alkaline lime index (MALI) vs SiO_2 (Wt %) D) Fe# vs SiO_2 (wt %), E) K_2O (wt %) vs Na_2O (wt %), F) K_2O (wt %) vs SiO_2 (wt %). E) Rb/Sr vs Rb/Ba diagram for strongly peraluminous granitoids modified from Sylvester (1998). Shaded fields, discontinuous line, and calculated melt are from of Sylvester (1998). F) CaO/Na_2O vs Al_2O_3/TiO_2 diagram with calculated pelite derived melt and basalt derived melts and mixing curve from Patiňo-Dounce and Harris (1998). 'S-type' granites in yellow, with field shaped yellow, 'I-type' granites in red, with field shaded red. Literature data from: Pe-Piper and Piper, (2000) (Naxos), (2002) (Delos); Stouraiti et al.,

DOI:10.1130/B36489.1

(2010) (Lavrion, Serifos, Tinos, Mykonos, Ikaria, Naxos, Paros, Basement), (2018) (Serifos); Altherr and Siebel, 2002 (Lavrion, Kos, Ikaria, Mykonos, Naxos, Paros, Tinos, Basement); Mastrakas and Seymour, (2000) (Tinos), Bolhar et al., (2017) (Basement).

Figure 8. A-J) Maficity vs oxide weight percent plots for all I- and S-type granites. Literature data from: Pe-Piper and Piper, 2000 (Naxos), 2002 (Delos); Stouraiti et al., 2010 (Lavrion, Serifos, Tinos, Mykonos, Ikaria, Naxos, Paros, Basement), 2017 (Serifos); Altherr and Siebel, 2002 (Lavrion, Kos, Ikaria, Mykonos, Naxos, Paros, Tinos, Basement); Mastrakas and Seymour, 2000 (Tinos), Bolhar et al., 2017 (Basement).

Figure 9. A) Spider diagrams of all trace elements arranged in order of incompatibility normalized to primitive mantle (Sun and McDonough, 1989), B) Spider diagrams of all trace elements arranged in order of incompatibility normalized to chondrite (Sun and McDonough, 1989)), C) Spider diagrams of HFSE's normalized to chrondrite (Sun and McDonough, 1989). Yellow lines represent 'S-type' granites and red lines represent 'I-type' granites.

Figure 10. Summary of U–Pb geochronology results for 'I- and S-type' granites. A) U–Pb age distributions for 'I-type' granite samples from Tinos (TLT64, 17TL05, 17TL36, 17TL34, TLTN36, TLT13) and Naxos aplite (17TL106). B) U–Pb age distributions for 'S-type' granites from Tinos (TLTN13, TLTN15, 17TL100), Delos (17TL95), Naxos orthogneiss basement (TL57) and S-type granites (TL58, TL63, TL69, TL72, TLN8, TLN10). B) Approximate distribution of known tectono-magmatic events recorded in the Cycladic basement based on data from this study and Flansburg et al., (2019); Keay et al., (2001); Martin et al., (2006); Bolhar et al., (2017), Bulle et al., (2010), Hinsken et al., (2017); Lamont et al., (2020a). C) Kernel density estimate (KDE) plot of best inherited zircon ages with Cyclades granites filtered for discordance. Red represents I-type granites (N = 15) Yellow is S-type granites (N = 137). Frequency-age histogram in background represents the total distribution of inherited ages in this study N = 174.

Figure 11. A) Initial $^{87}Sr/^{86}Sr$ vs εNd(t) isotope plot for Cyclades 'I-type' granites, 'S-type' granites, basement, recent Hellenic arc, old Hellenic Arc and Lamprophyres.; B) Calculated two stage Sm–Nd Model ages for Cyclades 'I- and S-type' granites using a crustal evolution $^{147}Sm/^{144}Nd = 0.09$ (Taylor and McCleanann, 1985). 'I- and S-type' literature data from Stouraiti et al., (2010; 2018); Pe-Piper, (2000); Altherr and Siebel., (2002); Pe-Piper et al., (2002). Basement literature data from Stouraiti et al., (2010, 2018); Pe-Piper, (2000); McGrath et al., (2017); Altherr and Siebel., (2002); Pe-Piper et al., (2002); Naxos Amphibolites from Bolhar et al., (2017); Basement and CBU from Briqueu et al., (1986). Lamprophyres from Soder et al., (2016); current Hellenic volcanic arc from Briqueu et al., (1986). Additional Hellenic arc data from Buettner et al., (2005); Alıcı et al. (2002), Chakrabarti et al. (2012); and Ersoy and Palmer., (2013). Data for Lesbos from Pe-Piper et al. (2014) and Pe-Piper and Piper, (1993) for Santorini from Bailey et al. (2009) and Kirchenbaur et al., (2012). Nisyros data from Buettner et al., (2005), Braschi et al. (2012) and Klaver et al., (2016). Old Hellenic arc active between ca. 5–2 Ma (Milos; Sacronic gulf, Aegina, Methana and Poros and Cromyonia) data from Francalanci et al., (2007); Pe-Piper and Hatzipanagiotou, (1997), Elburg and Smet, (2020).

Figure 12. Time chart showing the relative timing of granite genesis and intrusion, metamorphism and deformation on various structures on Tinos, Naxos, Mykonos (NCDS, KSZ, ZSZ, NCDS) bracketing the timing of granite intrusion, metamorphic thermal climax and the onset of rapid exhumation and normal faulting at ca. 15 Ma, interpreted to be the timing of NE-SW extension.

Figure 13. Tectonic model for the genesis of 'I- and S-type granites' in the ACM and shear zone development coinciding with a switch in tectonic regime and the onset of extension at ca. 15 Ma.

DOI:10.1130/B36489.1

Figure 14. Geodynamic models to explain the Cenozoic tectonic and magmatic evolution of the Aegean. Top panel, tectonic configuration of the Aegean at ca. 50 Ma involving NE dipping subduction causing closure of the Vardar/Pindos Ocean and production of Late Cretaceous arc (e.g., Anafi). A) Single slab rollback model requires continual subduction Greater Adria continental lithosphere, with accretion of Greater Adria Crust to the Upper Plate. This potentially predicts southward migration of the Volcanic arc and Barrovian metamorphism in the ACM due to back arc extension between ca. 30 Ma to Present. B) Two subduction zone model, involving Late Cretaceous to Eocene subduction zone leading to continental collision between Greater Adria and Eurasia, resulting in crustal thickening, Barrovian metamorphism between ca. 50–15 Ma. This is followed by initiation of the new Hellenic subduction zone during Miocene to explain Cretan Blueschists, and possibly associated with a decrease in convergence rate or convective removal of lithospheric mantle at ca. 15 Ma leading to onset of extension at ca. 15 Ma, intrusion of lamprophyres and ultra-potassic magmas in Western Turkey. The Hellenic arc only develops at ca. 5 Ma and is active until present.

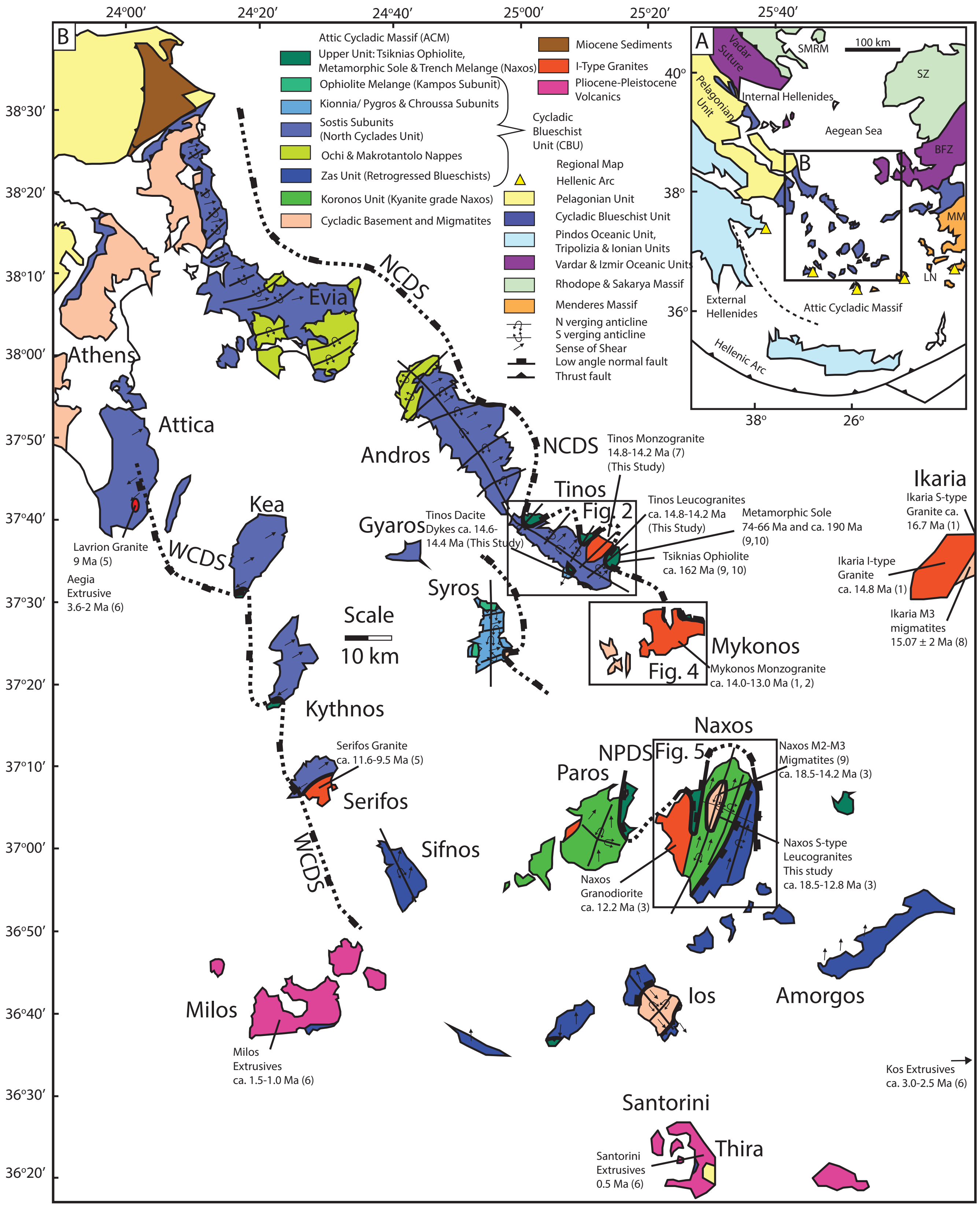
24°00′
24°20′
24°40′
25°00′
25°20′
25°40′
38°30′
38°20′
38°10′
38°00′
37°50′
37°40′
37°30′
37°20′
37°10′
37°00′
36°50′
36°40′
36°30′
36°20′
B
Attic Cycladic Massif (ACM)
Upper Unit: Tsiknias Ophiolite, Metamorphic Sole & Trench Melange (Naxos)
Ophiolite Melange (Kampos Subunit)
Kionnia/ Pygros & Chroussa Subunits
Sostis Subunits (North Cyclades Unit)
Ochi & Makrotantolo Nappes
Zas Unit (Retrogressed Blueschists)
Koronos Unit (Kyanite grade Naxos)
Cycladic Basement and Migmatites
Cycladic Blueschist Unit (CBU)
Miocene Sediments
I-Type Granites
Pliocene-Pleistocene Volcanics
Regional Map
Hellenic Arc
Pelagonian Unit
Cycladic Blueschist Unit
Pindos Oceanic Unit, Tripolizia & Ionian Units
Vardar & Izmir Oceanic Units
Rhodope & Sakarya Massif
Menderes Massif
N verging anticline
S verging anticline
Sense of Shear
Low angle normal fault
Thrust fault
A
Vadar Suture
SMRM
100 km
SZ
40°
Pelagonian Unit
Internal Hellenides
Aegean Sea
BFZ
38°
MM
LN
External Hellenides
Attic Cycladic Massif
36°
Hellenic Arc
38°
26°
Athens
Evia
NCDS
Attica
Andros
NCDS
Tinos Monzogranite 14.8-14.2 Ma (7) (This Study)
Tinos
Fig. 2
Tinos Leucogranites ca. 14.8-14.2 Ma (This Study)
Metamorphic Sole 74-66 Ma and ca. 190 Ma (9,10)
Tsiknias Ophiolite ca. 162 Ma (9, 10)
Ikaria
Ikaria S-type Granite ca. 16.7 Ma (1)
Ikaria I-type Granite ca. 14.8 Ma (1)
Ikaria M3 migmatites 15.07 ± 2 Ma (8)
Kea
Gyaros
Tinos Dacite Dykes ca. 14.6-14.4 Ma (This Study)
Lavrion Granite 9 Ma (5)
WCDS
Aegia Extrusive 3.6-2 Ma (6)
Syros
Scale
10 km
Mykonos
Fig. 4
Mykonos Monzogranite ca. 14.0-13.0 Ma (1, 2)
Kythnos
Naxos
NPDS
Fig. 5
Naxos M2-M3 Migmatites (9) ca. 18.5-14.2 Ma (3)
Serifos Granite ca. 11.6-9.5 Ma (5)
Paros
Serifos
Naxos S-type Leucogranites This study ca. 18.5-12.8 Ma (3)
WCDS
Sifnos
Naxos Granodiorite ca. 12.2 Ma (3)
Milos
Ios
Amorgos
Milos Extrusives ca. 1.5-1.0 Ma (6)
Kos Extrusives ca. 3.0-2.5 Ma (6)
Santorini
Thira
Santorini Extrusives 0.5 Ma (6)

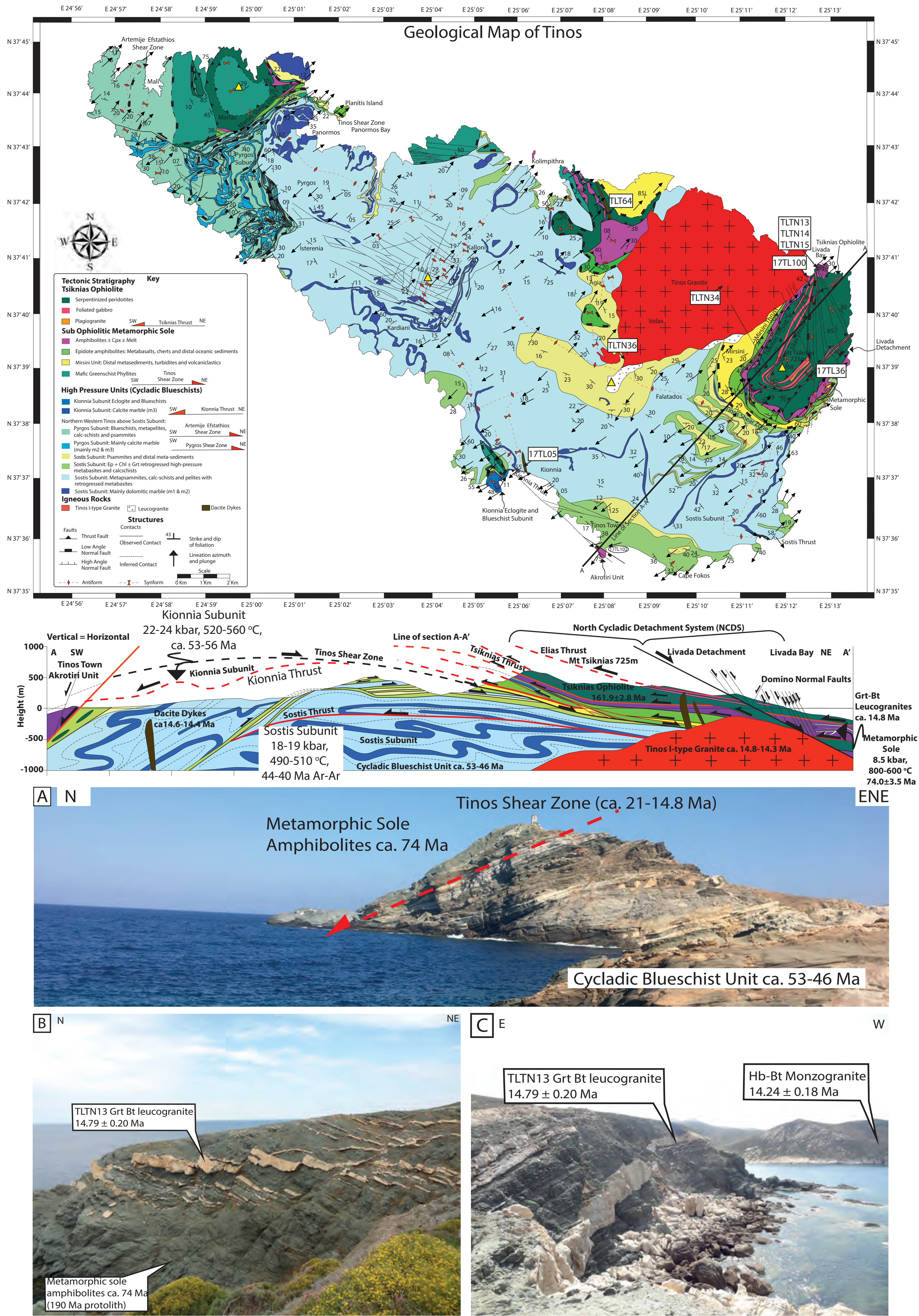

Geological Map of Tinos
Tectonic Stratigraphy
Tsiknias Ophiolite
Key
Serpentinized peridotites
Foliated gabbro
Plagiogranite
SW Tsiknias Thrust NE
Sub Ophiolitic Metamorphic Sole
Amphibolites ± Cpx ± Melt
Epidote amphibolites: Metabasalts, cherts and distal oceanic sediments
Mirsini Unit: Distal metasediments, turbidites and volcaniclastics
Mafic Greenschist Phyllites
SW Tinos Shear Zone NE
High Pressure Units (Cycladic Blueschists)
Kionnia Subunit Eclogite and Blueschists
Kionnia Subunit: Calcite marble (m3)
SW Kionnia Thrust NE
Northern Western Tinos above Sostis Subunit:
Pyrgos Subunit: Blueschists, metapelites, calc-schists and psammites
SW Artemije Efstathios Shear Zone NE
Pyrgos Subunit: Mainly calcite marble (mainly m2 & m3)
SW Pygros Shear Zone NE
Sostis Subunit: Psammites and distal meta-sediments
Sostis Subunit: Ep + Chl ± Grt retrogressed high-pressure metabasites and calcschists
Sostis Subunit: Metapsammites, calc-schists and pelites with retrogressed metabasites
Sostis Subunit: Mainly dolomitic marble (m1 & m2)
Igneous Rocks
Tinos I-type Granite
Leucogranite
Dacite Dykes
Structures
Faults
Thrust Fault
Low Angle Normal Fault
High Angle Normal Fault
Contacts
Observed Contact
Inferred Contact
Strike and dip of foliation
Lineation azimuth and plunge
Scale
0 Km 1 Km 2 Km
Antiform
Synform
Artemije Efstathios Shear Zone
Planitis Island
Tinos Shear Zone
Panormos Bay
Panormos
Pyrgos Subunit
Pyrgos
Isterenia
Kalloni
Kardiani
Kolimpithra
Agia
Tinos Granite
Volax
Mirsini
Falatados
Mt Tsiknias 725m
Tsiknias Ophiolite
Livada Bay
Livada Detachment
Metamorphic Sole
Kionnia
Kionnia Thrust
Kionnia Eclogite and Blueschist Subunit
Tinos Town
Line of Section A-A'
Akrotiri Unit
Cape Fokos
Sostis Subunit
Sostis Thrust
TLT64
TLTN13
TLTN14
TLTN15
17TL100
TLTN34
TLTN36
17TL36
17TL05
Kionnia Subunit
22-24 kbar, 520-560 °C,
ca. 53-56 Ma
Vertical = Horizontal
A SW
Tinos Town
Akrotiri Unit
Height (m)
Tinos Shear Zone
Kionnia Subunit
Kionnia Thrust
Line of section A-A'
North Cycladic Detachment System (NCDS)
Tsiknias Thrust
Elias Thrust
Mt Tsiknias 725m
Livada Detachment
Livada Bay NE A'
Domino Normal Faults
Tsiknias Ophiolite
161.9±2.8 Ma
Grt-Bt Leucogranites ca. 14.8 Ma
Metamorphic Sole
8.5 kbar,
800-600 °C
74.0±3.5 Ma
Dacite Dykes
ca14.6-14.4 Ma
Sostis Thrust
Sostis Subunit
18-19 kbar,
490-510 °C,
44-40 Ma Ar-Ar
Sostis Subunit
Tinos I-type Granite ca. 14.8-14.3 Ma
Cycladic Blueschist Unit ca. 53-46 Ma
A N
ENE
Tinos Shear Zone (ca. 21-14.8 Ma)
Metamorphic Sole
Amphibolites ca. 74 Ma
Cycladic Blueschist Unit ca. 53-46 Ma
B N
NE
TLTN13 Grt Bt leucogranite
14.79 ± 0.20 Ma
Metamorphic sole
amphibolites ca. 74 Ma
(190 Ma protolith)
C E
W
TLTN13 Grt Bt leucogranite
14.79 ± 0.20 Ma
Hb-Bt Monzogranite
14.24 ± 0.18 Ma


A NW
NE
Sostis Unit blueschists ca. 46.4 Ma
17TL05 Dacite dyke 14.43 ± 0.15 Ma
B N
S
TLT64 Dacite dyke 14.43 ± 0.19 Ma
C
Tsiknias Ophiolite ca. 162 Ma
17TL36 Dacite dyke 14.51 ± 0.19 Ma
D E
W
Hb-Bt Monzogranite 14.24 ± 0.18 Ma
Metamorphic sole amphibolites ca. 74 Ma (190 Ma protolith)
S2b obduction top-to-SW fabric
E
Hb-Bt Monzogranite 14.24 ± 0.18 Ma
F
17TL100 Bt cross-cutting leucogranite 14.33 ± 0.13 Ma
Tinos Hb-Bt Monzogranite
G NW
NE
Tinos Hb-Bt Monzogranite 14.24 ± 0.18 Ma
Tsiknias Ophiolite ca. 162 Ma
Livada Bay
Metamorphic Sole ca. 74 Ma (190 Ma protolith)
100 m
H
17TL36
Bt
Zr
Pl Phenocrst
Ep
Pl
200 um
I
NE
TLTN34 Deformed monzogranite 14.84 ± 0.11 Ma
J
TLTN34
Qtz
Pl
500 um
K N
E
TLTN15 Grt-Bt leucogranite 14.23 ± 0.89 Ma
Curvature towards normal fault
L
TLTN15 Grt-Bt leucogranite 14.23 ± 0.89 Ma
Little offset from normal fault
M
TLTN13
Pl
Grt
Qtz
200 um

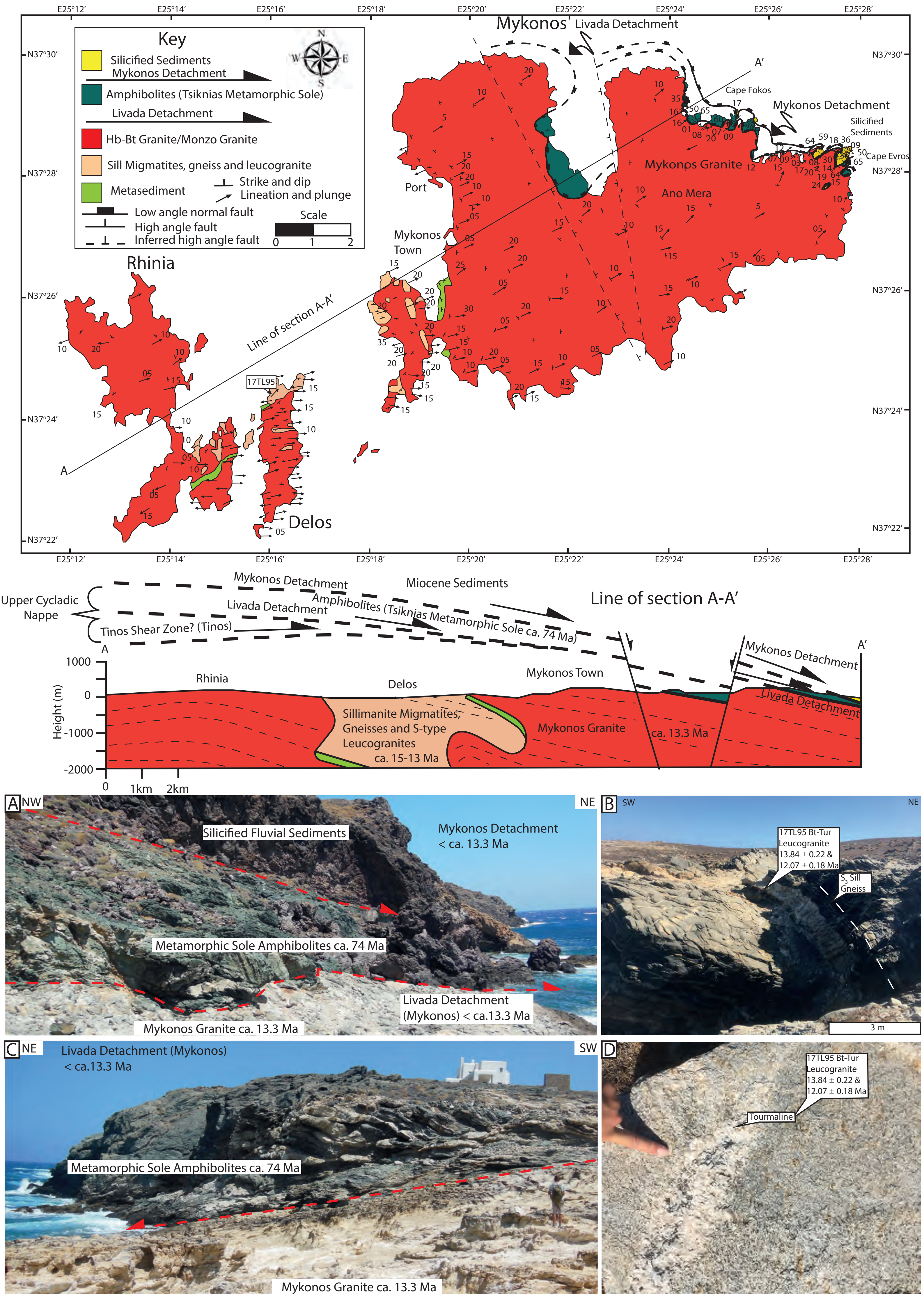

E25°12′
E25°14′
E25°16′
E25°18′
E25°20′
E25°22′
E25°24′
E25°26′
E25°28′
N37°30′
N37°28′
N37°26′
N37°24′
N37°22′
Key
Silicified Sediments
Mykonos Detachment
Amphibolites (Tsiknias Metamorphic Sole)
Livada Detachment
Hb-Bt Granite/Monzo Granite
Sill Migmatites, gneiss and leucogranite
Metasediment
Strike and dip
Lineation and plunge
Low angle normal fault
High angle fault
Inferred high angle fault
Scale
0 1 2
Mykonos
Livada Detachment
Cape Fokos
Mykonos Detachment
Silicified Sediments
Cape Evros
Mykonos Granite
Ano Mera
Port
Mykonos Town
Rhinia
Line of section A-A′
17TL95
Delos
A
A′
Mykonos Detachment
Miocene Sediments
Line of section A-A′
Upper Cycladic Nappe
Livada Detachment
Amphibolites (Tsiknias Metamorphic Sole ca. 74 Ma)
Tinos Shear Zone? (Tinos)
1000
0
-1000
-2000
Height (m)
Rhinia
Delos
Mykonos Town
Mykonos Detachment
Livada Detachment
Sillimanite Migmatites, Gneisses and S-type Leucogranites ca. 15-13 Ma
Mykonos Granite
ca. 13.3 Ma
0 1km 2km
A
NW
NE
Silicified Fluvial Sediments
Mykonos Detachment < ca. 13.3 Ma
Metamorphic Sole Amphibolites ca. 74 Ma
Livada Detachment (Mykonos) < ca.13.3 Ma
Mykonos Granite ca. 13.3 Ma
B
SW
NE
17TL95 Bt-Tur Leucogranite 13.84 ± 0.22 & 12.07 ± 0.18 Ma
S_3 Sill Gneiss
3 m
C
NE
SW
Livada Detachment (Mykonos) < ca.13.3 Ma
Metamorphic Sole Amphibolites ca. 74 Ma
Mykonos Granite ca. 13.3 Ma
D
17TL95 Bt-Tur Leucogranite 13.84 ± 0.22 & 12.07 ± 0.18 Ma
Tourmaline

Geological Map of Naxos

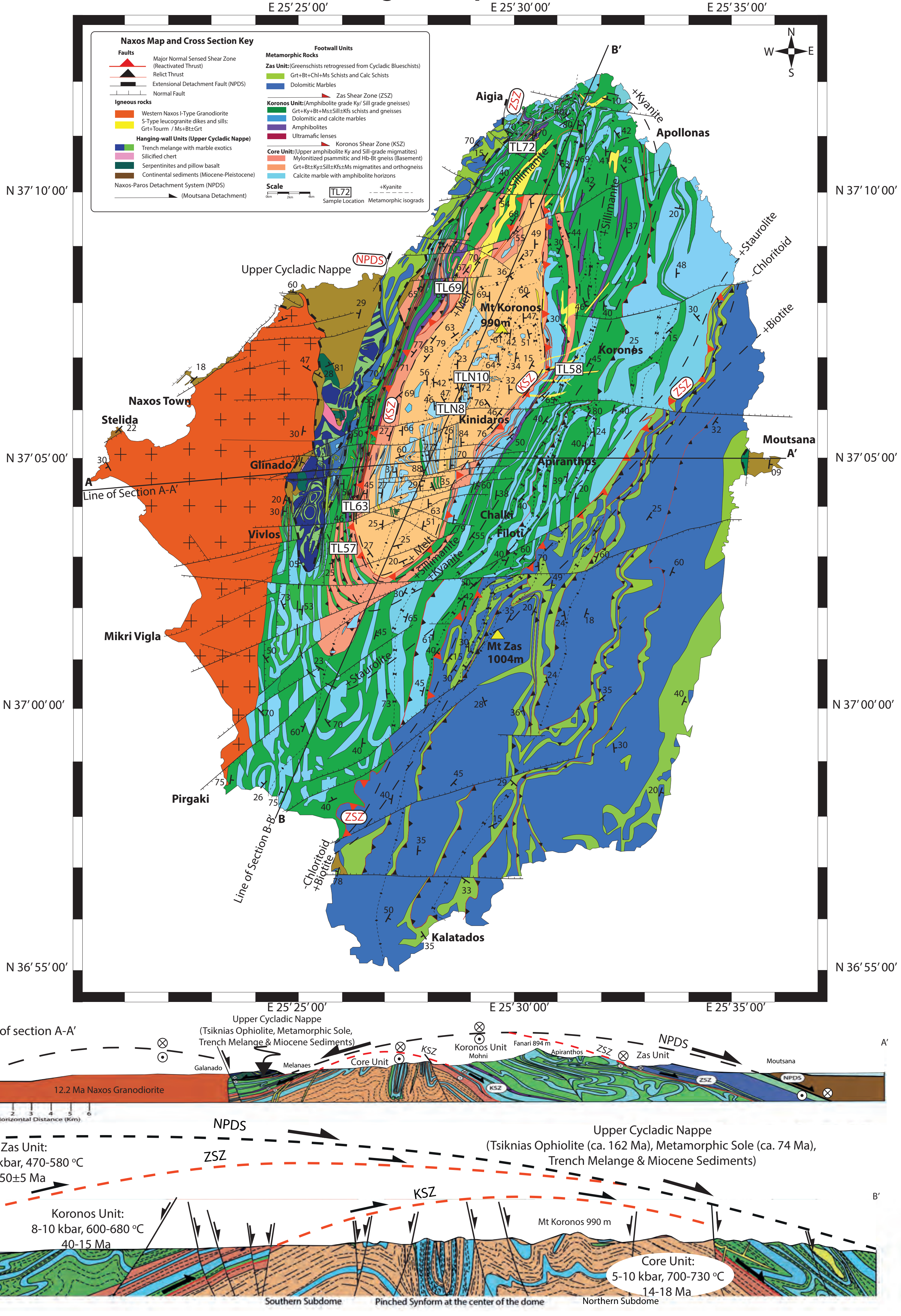

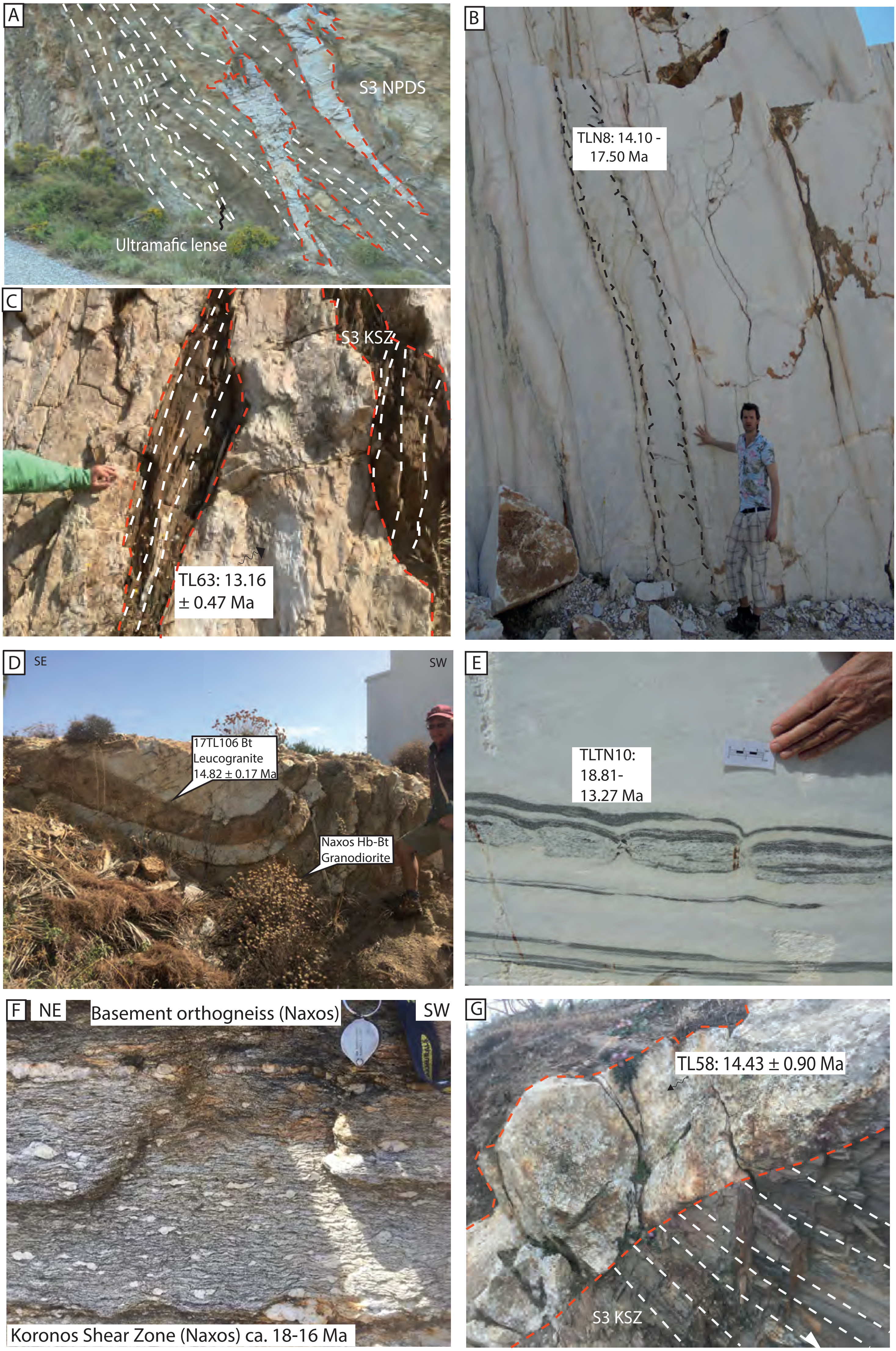
A
S3 NPDS
Ultramafic lense
B
TLN8: 14.10 - 17.50 Ma
C
S3 KSZ
TL63: 13.16 ± 0.47 Ma
D
SE
SW
17TL106 Bt Leucogranite 14.82 ± 0.17 Ma
Naxos Hb-Bt Granodiorite
E
TLTN10: 18.81-13.27 Ma
F
NE
Basement orthogneiss (Naxos)
SW
Koronos Shear Zone (Naxos) ca. 18-16 Ma
G
TL58: 14.43 ± 0.90 Ma
S3 KSZ

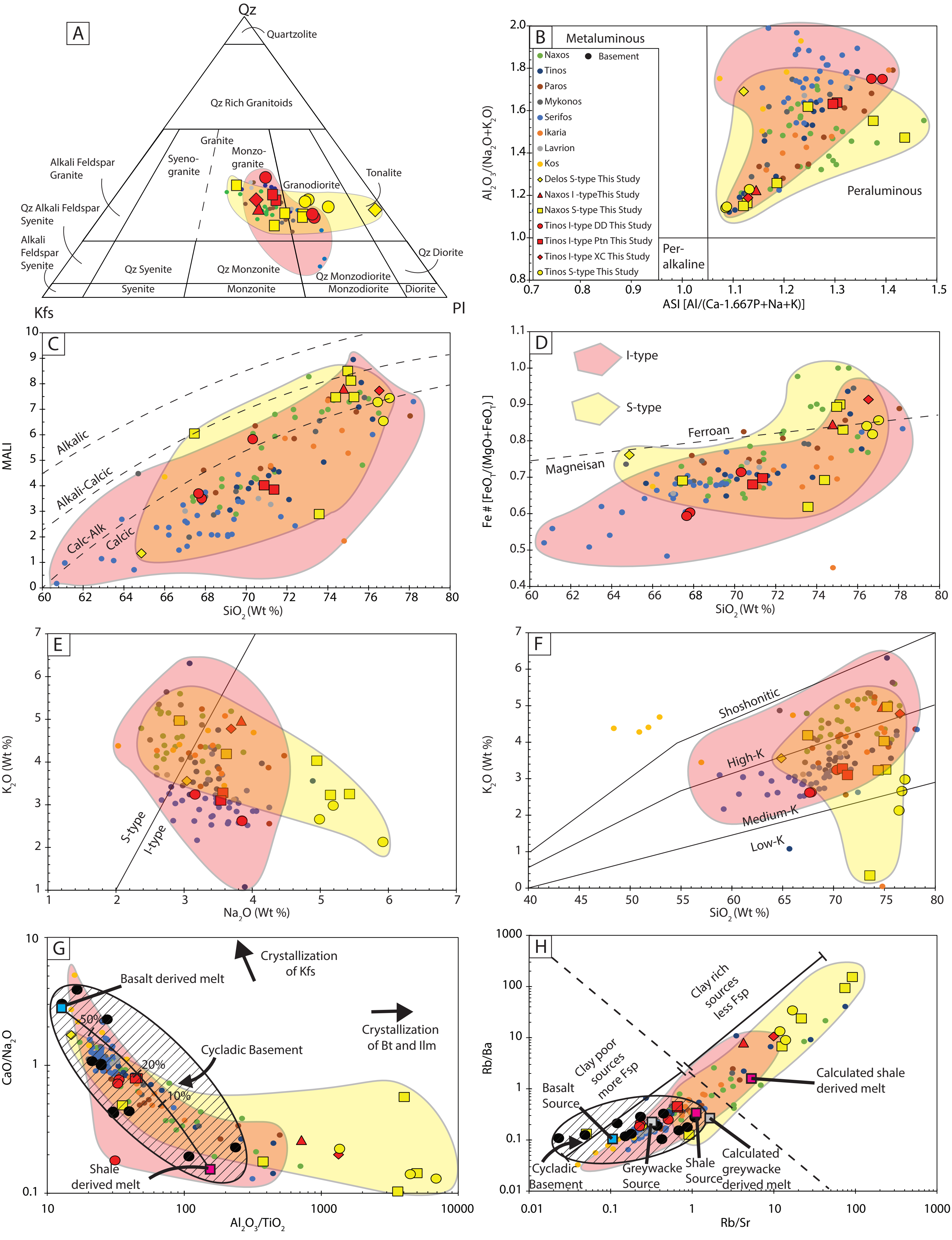
A
Qz
Quartzolite
Qz Rich Granitoids
Granite
Syeno-granite
Monzo-granite
Granodiorite
Tonalite
Alkali Feldspar Granite
Qz Alkali Feldspar Syenite
Alkali Feldspar Syenite
Qz Syenite
Qz Monzonite
Qz Monzodiorite
Qz Diorite
Syenite
Monzonite
Monzodiorite
Diorite
Kfs
Pl
B
Metaluminous
Naxos
Basement
Tinos
Paros
Mykonos
Serifos
Ikaria
Lavrion
Kos
Delos S-type This Study
Naxos I -typeThis Study
Naxos S-type This Study
Tinos I-type DD This Study
Tinos I-type Ptn This Study
Tinos I-type XC This Study
Tinos S-type This Study
Peraluminous
Per-alkaline
ASI [Al/(Ca-1.667P+Na+K)]
C
MALI
Alkalic
Alkali-Calcic
Calc-Alk
Calcic
SiO2 (Wt %)
D
I-type
S-type
Ferroan
Magneisan
Fe # [FeOT/(MgO+FeOT)]
E
K2O (Wt %)
S-type
I-type
Na2O (Wt %)
F
Shoshonitic
High-K
Medium-K
Low-K
G
CaO/Na2O
Crystallization of Kfs
Basalt derived melt
Crystallization of Bt and Ilm
Cycladic Basement
50%
20%
10%
Shale derived melt
Al2O3/TiO2
H
Rb/Ba
Clay rich sources less Fsp
Clay poor sources more Fsp
Basalt Source
Calculated shale derived melt
Cycladic Basement
Greywacke Source
Shale Source
Calculated greywacke derived melt
Rb/Sr

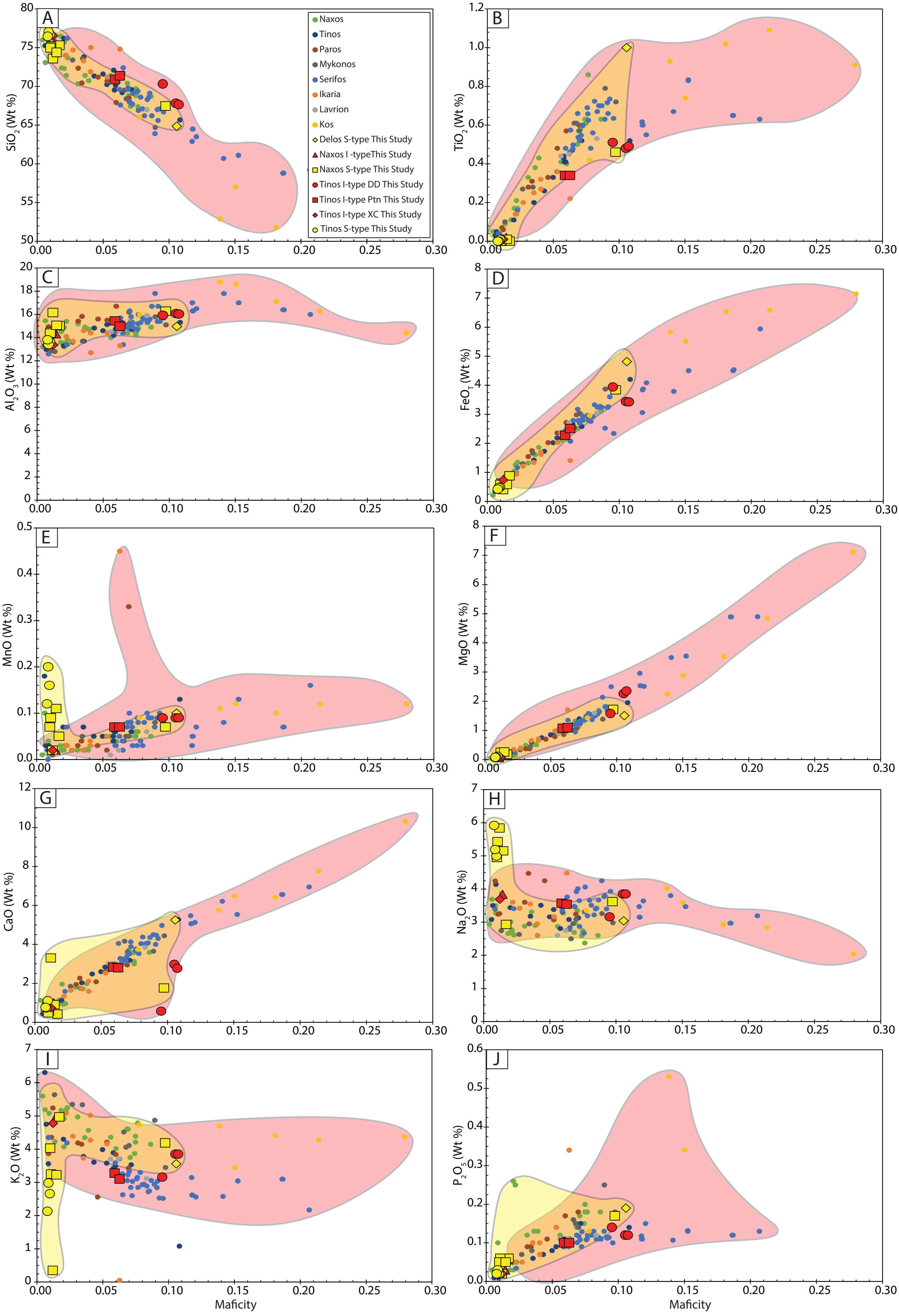

A
B
C
D
E
F
G
H
I
J
Naxos
Tinos
Paros
Mykonos
Serifos
Ikaria
Lavrion
Kos
Delos S-type This Study
Naxos I -typeThis Study
Naxos S-type This Study
Tinos I-type DD This Study
Tinos I-type Ptn This Study
Tinos I-type XC This Study
Tinos S-type This Study
SiO2 (Wt %)
TiO2 (Wt %)
Al2O3 (Wt %)
FeOT (Wt %)
MnO (Wt %)
MgO (Wt %)
CaO (Wt %)
Na2O (Wt %)
K2O (Wt %)
P2O5 (Wt %)
Maficity
Maficity

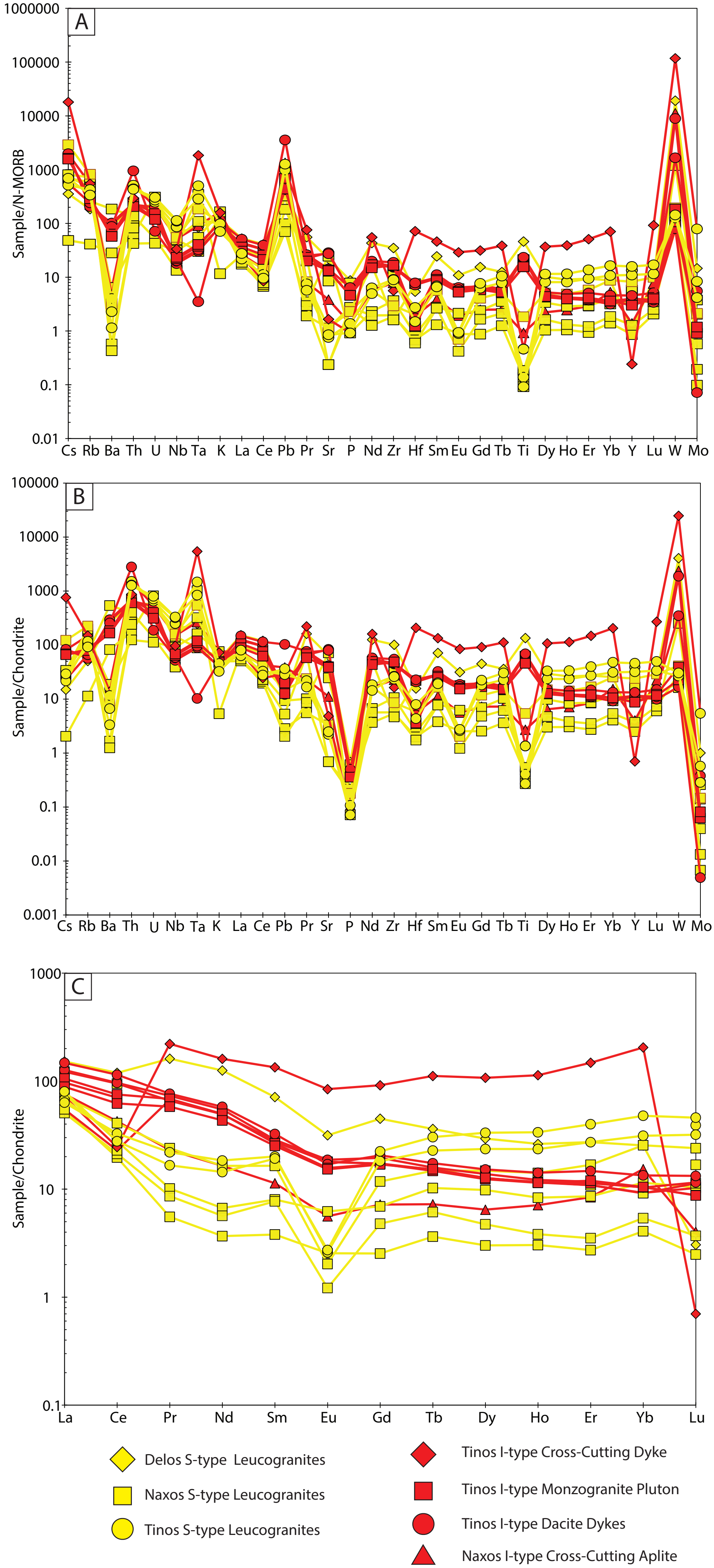

A
Sample/N-MORB
1000000
100000
10000
1000
100
10
1
0.1
0.01
Cs Rb Ba Th U Nb Ta K La Ce Pb Pr Sr P Nd Zr Hf Sm Eu Gd Tb Ti Dy Ho Er Yb Y Lu W Mo
B
Sample/Chondrite
100000
10000
1000
100
10
1
0.1
0.01
0.001
Cs Rb Ba Th U Nb Ta K La Ce Pb Pr Sr P Nd Zr Hf Sm Eu Gd Tb Ti Dy Ho Er Yb Y Lu W Mo
C
Sample/Chondrite
1000
100
10
1
0.1
La Ce Pr Nd Sm Eu Gd Tb Dy Ho Er Yb Lu
Delos S-type Leucogranites
Naxos S-type Leucogranites
Tinos S-type Leucogranites
Tinos I-type Cross-Cutting Dyke
Tinos I-type Monzogranite Pluton
Tinos I-type Dacite Dykes
Naxos I-type Cross-Cutting Aplite

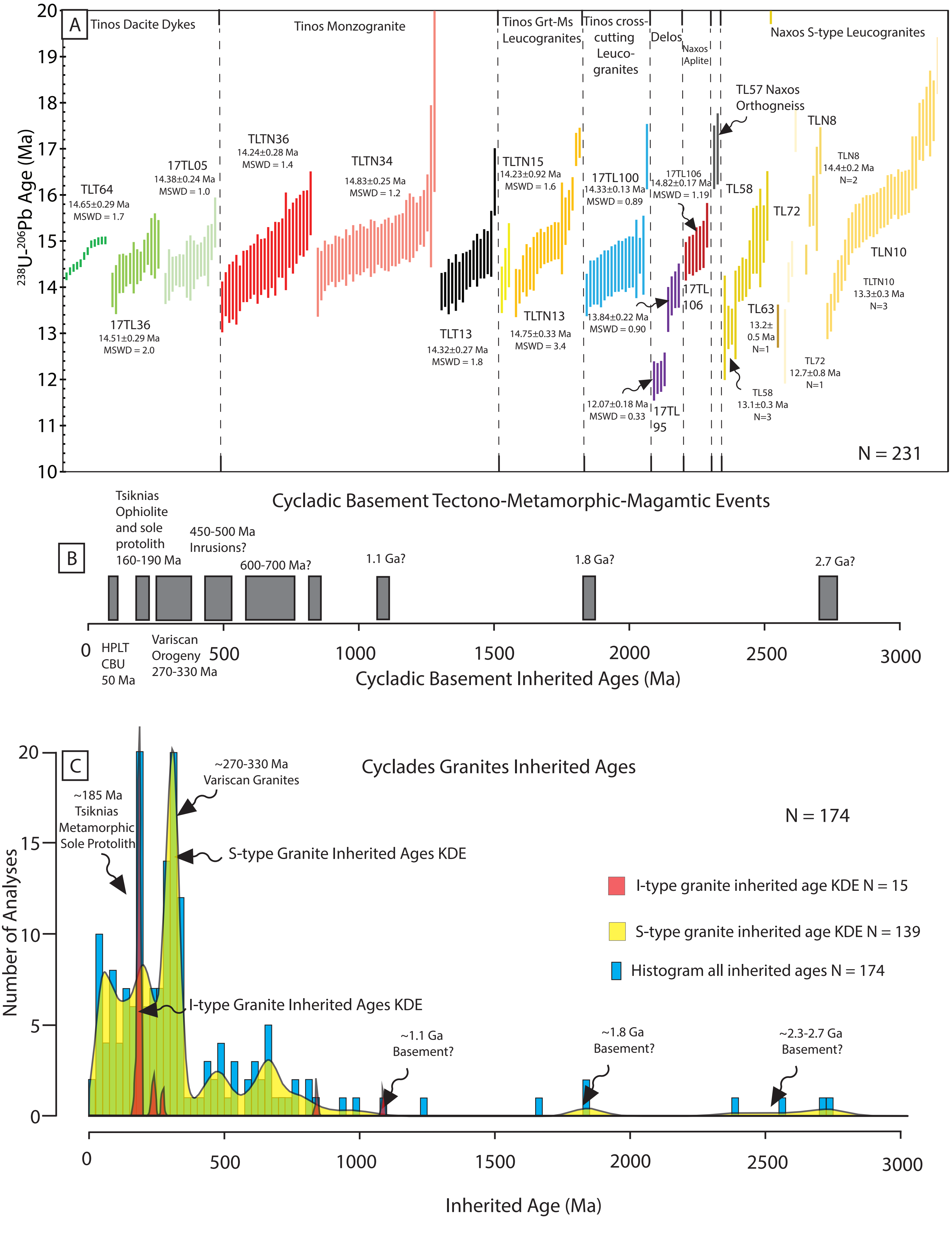

A
Tinos Dacite Dykes
Tinos Monzogranite
Tinos Grt-Ms Leucogranites
Tinos cross-cutting Leuco-granites
Delos
Naxos Aplite
Naxos S-type Leucogranites
$^{238}U-^{206}Pb$ Age (Ma)
TLT64 14.65±0.29 Ma MSWD = 1.7
17TL36 14.51±0.29 Ma MSWD = 2.0
17TL05 14.38±0.24 Ma MSWD = 1.0
TLTN36 14.24±0.28 Ma MSWD = 1.4
TLTN34 14.83±0.25 Ma MSWD = 1.2
TLT13 14.32±0.27 Ma MSWD = 1.8
TLTN15 14.23±0.92 Ma MSWD = 1.6
TLTN13 14.75±0.33 Ma MSWD = 3.4
17TL100 14.33±0.13 Ma MSWD = 0.89
13.84±0.22 Ma MSWD = 0.90
12.07±0.18 Ma MSWD = 0.33
17TL 95
17TL106 14.82±0.17 Ma MSWD = 1.19
17TL 106
TL57 Naxos Orthogneiss
TL58
TL72
TLN8
TLN8 14.4±0.2 Ma N=2
TLN10
TLTN10 13.3±0.3 Ma N=3
TL63 13.2± 0.5 Ma N=1
TL72 12.7±0.8 Ma N=1
TL58 13.1±0.3 Ma N=3
N = 231
Cycladic Basement Tectono-Metamorphic-Magamtic Events
B
Tsiknias Ophiolite and sole protolith 160-190 Ma
450-500 Ma Inrusions?
600-700 Ma?
1.1 Ga?
1.8 Ga?
2.7 Ga?
HPLT CBU 50 Ma
Variscan Orogeny 270-330 Ma
Cycladic Basement Inherited Ages (Ma)
C
Cyclades Granites Inherited Ages
~185 Ma Tsiknias Metamorphic Sole Protolith
~270-330 Ma Variscan Granites
S-type Granite Inherited Ages KDE
I-type Granite Inherited Ages KDE
N = 174
I-type granite inherited age KDE N = 15
S-type granite inherited age KDE N = 139
Histogram all inherited ages N = 174
~1.1 Ga Basement?
~1.8 Ga Basement?
~2.3-2.7 Ga Basement?
Number of Analyses
Inherited Age (Ma)

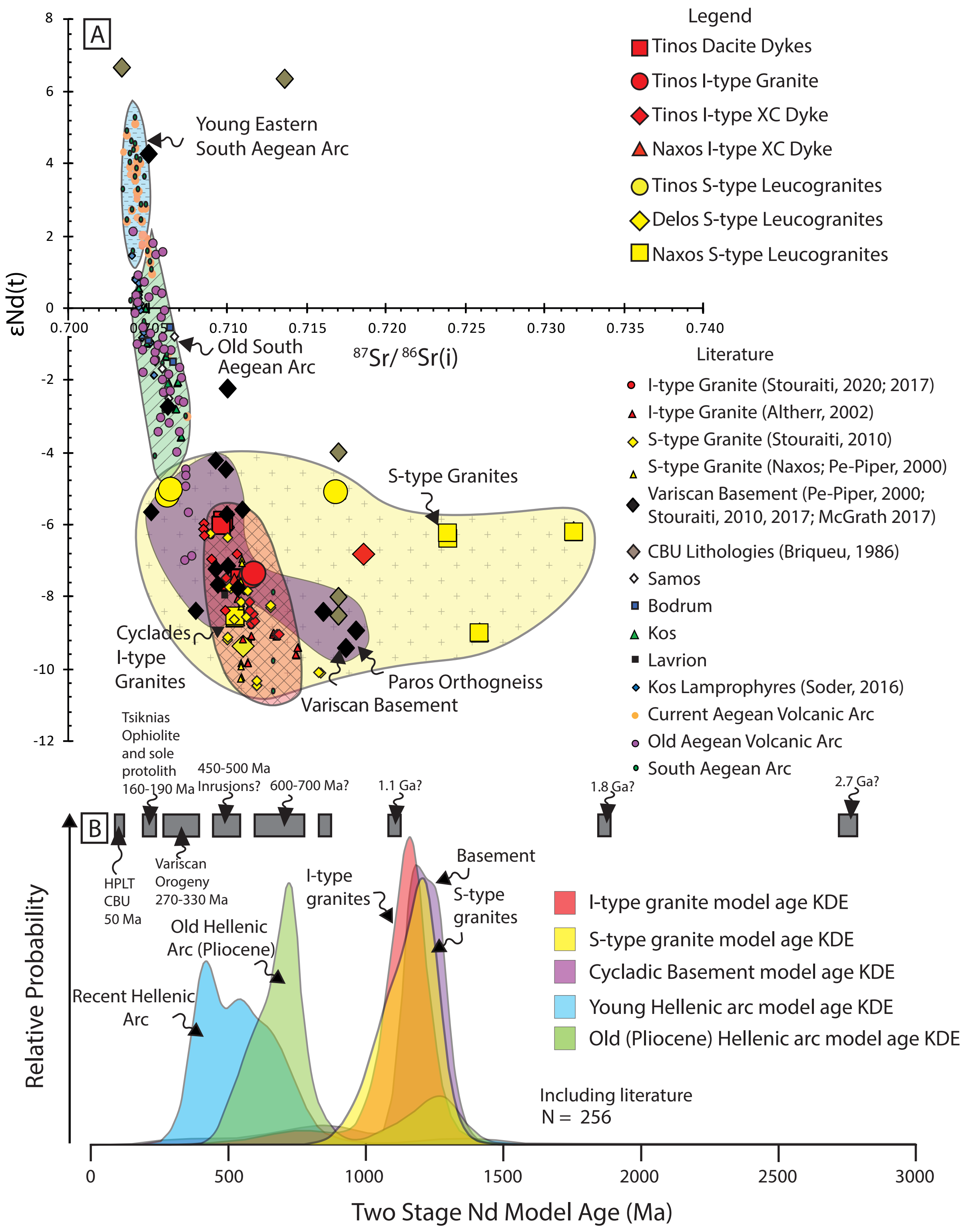

A
Legend
Tinos Dacite Dykes
Tinos I-type Granite
Tinos I-type XC Dyke
Naxos I-type XC Dyke
Tinos S-type Leucogranites
Delos S-type Leucogranites
Naxos S-type Leucogranites
Young Eastern South Aegean Arc
Old South Aegean Arc
S-type Granites
Cyclades I-type Granites
Paros Orthogneiss
Variscan Basement
εNd(t)
$^{87}Sr/^{86}Sr(i)$
Literature
I-type Granite (Stouraiti, 2020; 2017)
I-type Granite (Altherr, 2002)
S-type Granite (Stouraiti, 2010)
S-type Granite (Naxos; Pe-Piper, 2000)
Variscan Basement (Pe-Piper, 2000; Stouraiti, 2010, 2017; McGrath 2017)
CBU Lithologies (Briqueu, 1986)
Samos
Bodrum
Kos
Lavrion
Kos Lamprophyres (Soder, 2016)
Current Aegean Volcanic Arc
Old Aegean Volcanic Arc
South Aegean Arc
B
Tsiknias Ophiolite and sole protolith 160-190 Ma
450-500 Ma Inrusions?
600-700 Ma?
1.1 Ga?
1.8 Ga?
2.7 Ga?
HPLT CBU 50 Ma
Variscan Orogeny 270-330 Ma
Basement
I-type granites
S-type granites
Old Hellenic Arc (Pliocene)
Recent Hellenic Arc
I-type granite model age KDE
S-type granite model age KDE
Cycladic Basement model age KDE
Young Hellenic arc model age KDE
Old (Pliocene) Hellenic arc model age KDE
Including literature N = 256
Relative Probability
Two Stage Nd Model Age (Ma)

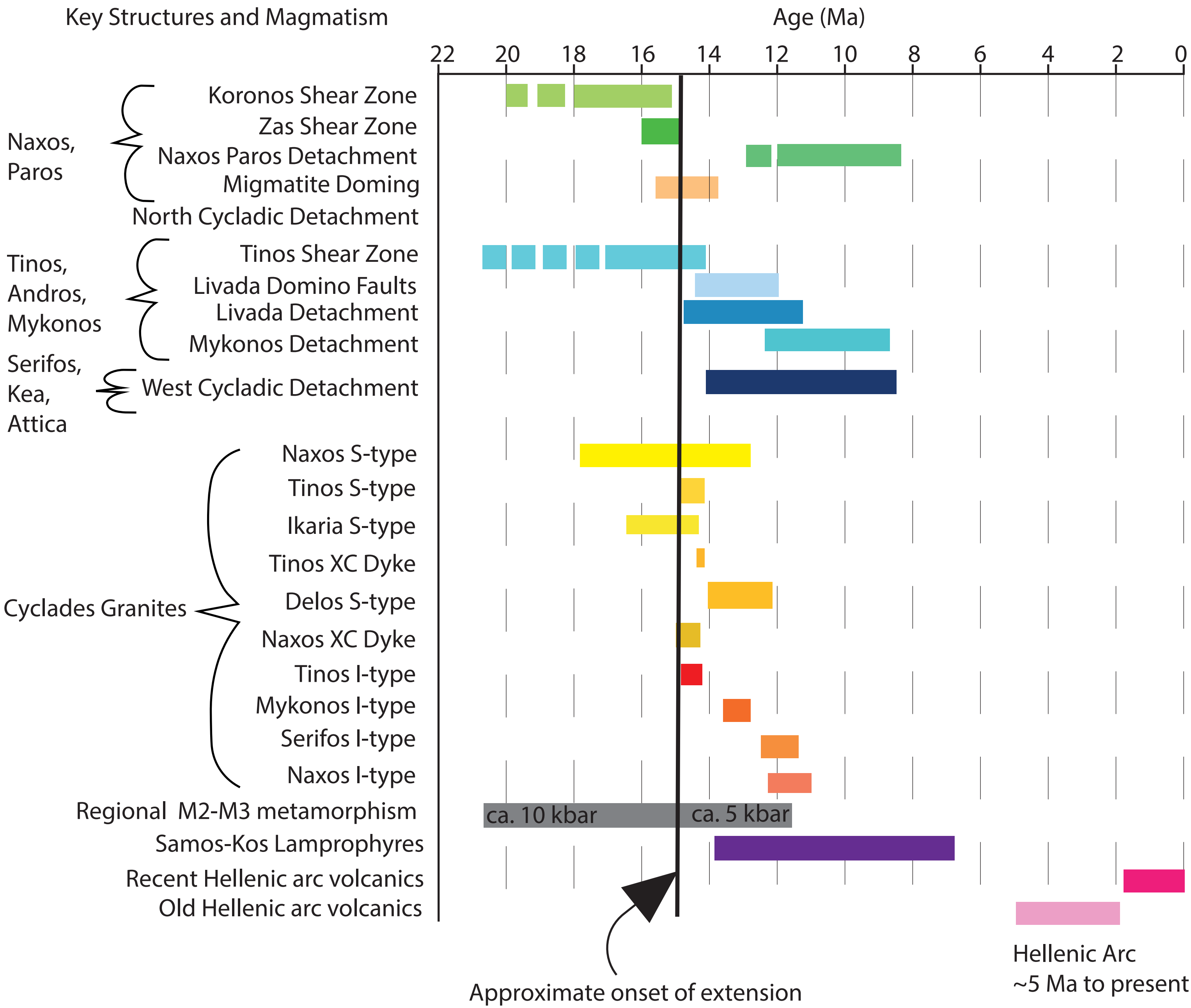
Key Structures and Magmatism
Age (Ma)
22
20
18
16
14
12
10
8
6
4
2
0
Naxos, Paros
Koronos Shear Zone
Zas Shear Zone
Naxos Paros Detachment
Migmatite Doming
North Cycladic Detachment
Tinos, Andros, Mykonos
Tinos Shear Zone
Livada Domino Faults
Livada Detachment
Mykonos Detachment
Serifos, Kea, Attica
West Cycladic Detachment
Cyclades Granites
Naxos S-type
Tinos S-type
Ikaria S-type
Tinos XC Dyke
Delos S-type
Naxos XC Dyke
Tinos I-type
Mykonos I-type
Serifos I-type
Naxos I-type
Regional M2-M3 metamorphism
ca. 10 kbar
ca. 5 kbar
Samos-Kos Lamprophyres
Recent Hellenic arc volcanics
Old Hellenic arc volcanics
Approximate onset of extension
Hellenic Arc
~5 Ma to present

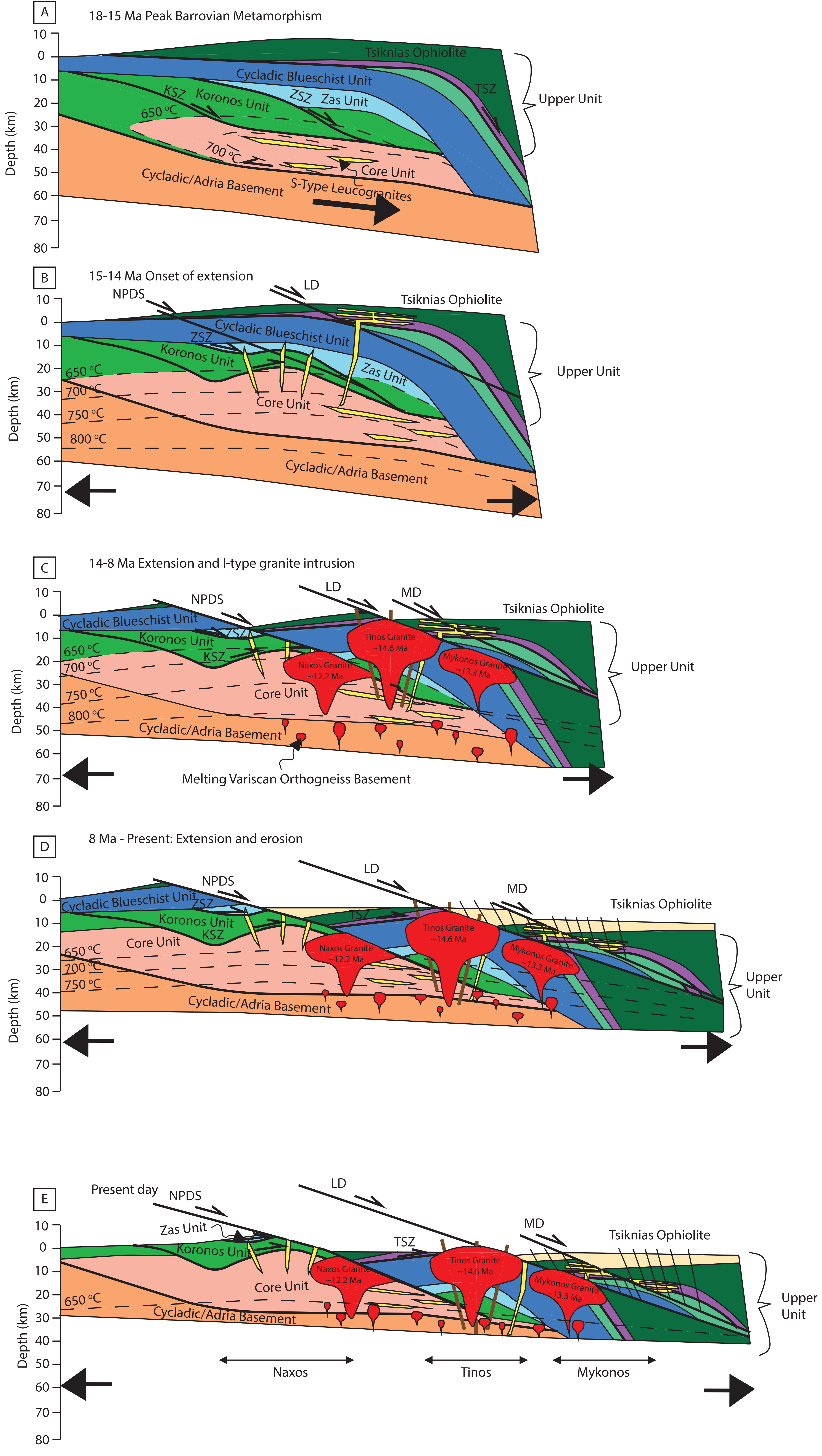

A
18-15 Ma Peak Barrovian Metamorphism
Tsiknias Ophiolite
Cycladic Blueschist Unit
TSZ
Upper Unit
KSZ
Koronos Unit
ZSZ
Zas Unit
650 °C
700 °C
Core Unit
Cycladic/Adria Basement
S-Type Leucogranites
Depth (km)
B
15-14 Ma Onset of extension
NPDS
LD
Tsiknias Ophiolite
Cycladic Blueschist Unit
ZSZ
Koronos Unit
Zas Unit
Upper Unit
650 °C
700 °C
750 °C
800 °C
Core Unit
Cycladic/Adria Basement
C
14-8 Ma Extension and I-type granite intrusion
LD
MD
NPDS
Tsiknias Ophiolite
Cycladic Blueschist Unit
Koronos Unit
KSZ
Tinos Granite
~14.6 Ma
Naxos Granite
~12.2 Ma
Mykonos Granite
~13.3 Ma
Upper Unit
Core Unit
Cycladic/Adria Basement
Melting Variscan Orthogneiss Basement
D
8 Ma - Present: Extension and erosion
LD
NPDS
MD
Tsiknias Ophiolite
Cycladic Blueschist Unit
ZSZ
TSZ
Koronos Unit
KSZ
Core Unit
Upper Unit
Cycladic/Adria Basement
E
Present day
NPDS
LD
Zas Unit
Koronos Unit
TSZ
MD
Tsiknias Ophiolite
Core Unit
Cycladic/Adria Basement
Naxos
Tinos
Mykonos

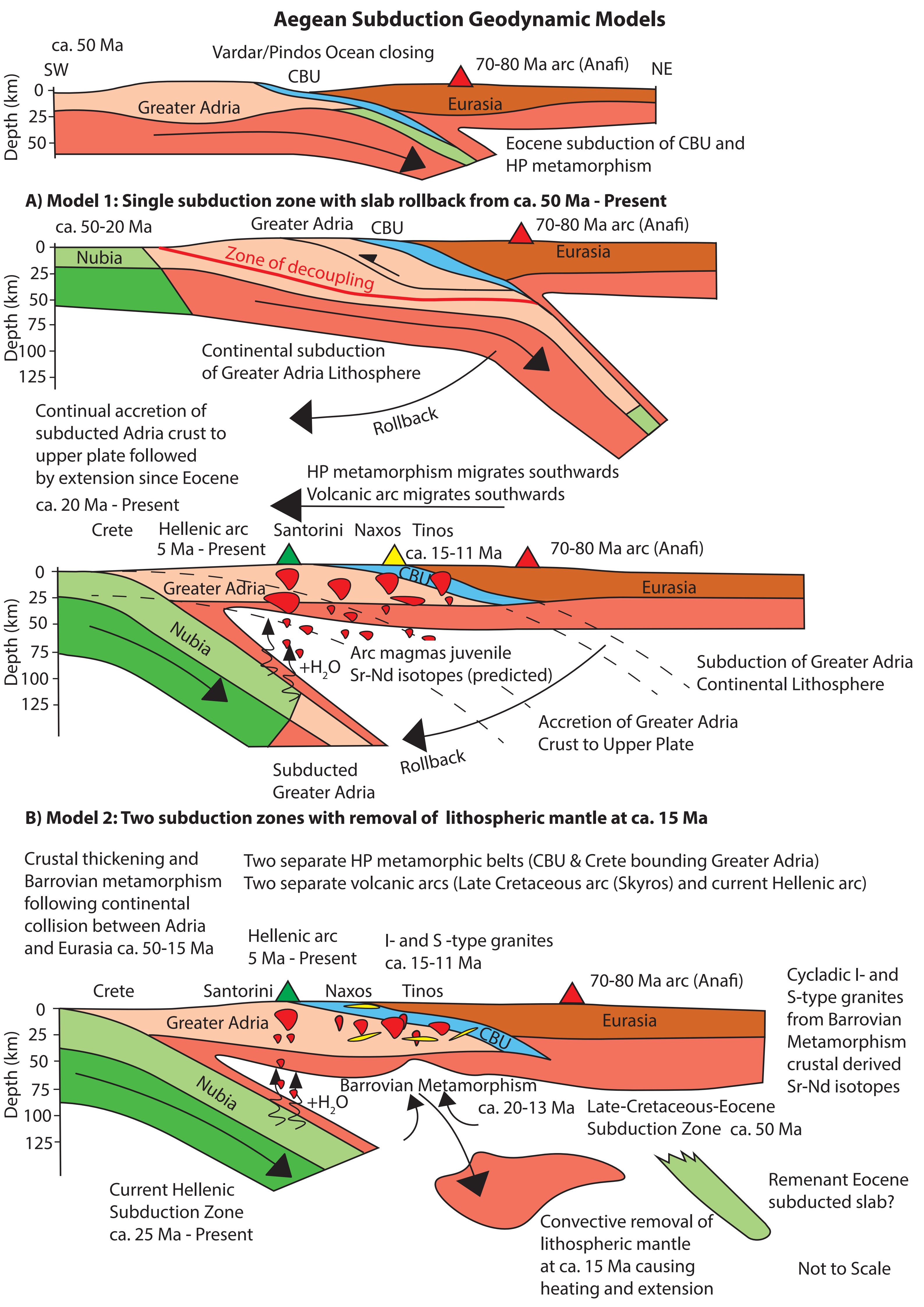
Aegean Subduction Geodynamic Models
ca. 50 Ma
SW
Vardar/Pindos Ocean closing
CBU
70-80 Ma arc (Anafi)
NE
Greater Adria
Eurasia
Depth (km)
0
25
50
Eocene subduction of CBU and
HP metamorphism
A) Model 1: Single subduction zone with slab rollback from ca. 50 Ma - Present
ca. 50-20 Ma
Greater Adria
CBU
70-80 Ma arc (Anafi)
Nubia
Zone of decoupling
Eurasia
0
25
50
75
100
125
Continental subduction
of Greater Adria Lithosphere
Continual accretion of
subducted Adria crust to
upper plate followed
by extension since Eocene
Rollback
HP metamorphism migrates southwards
Volcanic arc migrates southwards
ca. 20 Ma - Present
Crete
Hellenic arc
5 Ma - Present
Santorini
Naxos
Tinos
ca. 15-11 Ma
70-80 Ma arc (Anafi)
Greater Adria
CBU
Eurasia
Nubia
$+H_2O$
Arc magmas juvenile
Sr-Nd isotopes (predicted)
Subduction of Greater Adria
Continental Lithosphere
Accretion of Greater Adria
Crust to Upper Plate
Subducted
Greater Adria
Rollback
B) Model 2: Two subduction zones with removal of lithospheric mantle at ca. 15 Ma
Crustal thickening and
Barrovian metamorphism
following continental
collision between Adria
and Eurasia ca. 50-15 Ma
Two separate HP metamorphic belts (CBU & Crete bounding Greater Adria)
Two separate volcanic arcs (Late Cretaceous arc (Skyros) and current Hellenic arc)
Hellenic arc
5 Ma - Present
I- and S -type granites
ca. 15-11 Ma
Crete
Santorini
Naxos
Tinos
70-80 Ma arc (Anafi)
Cycladic I- and
S-type granites
from Barrovian
Metamorphism
crustal derived
Sr-Nd isotopes
Greater Adria
Eurasia
CBU
Nubia
$+H_2O$
Barrovian Metamorphism
ca. 20-13 Ma
Late-Cretaceous-Eocene
Subduction Zone ca. 50 Ma
Current Hellenic
Subduction Zone
ca. 25 Ma - Present
Convective removal of
lithospheric mantle
at ca. 15 Ma causing
heating and extension
Remenant Eocene
subducted slab?
Not to Scale

Table 1: Summary of Granitoid Field Relations

Sample Name	Rock Type	Island	GPS Location	Granitoid Classification	Mineralogy
TLT64	Dacite Dyke	Tinos	N37.628196, E25.164215	I-type	Hb-Bt-Fsp-Qz-Ap-Sph
17TL36	Dacite Dyke	Tinos	N37.580526, E25.23496	I-type	Hb-Bt-Fsp-Qz-Ap-Sph
17TL05	Dacite Dyke	Tinos	N37.553558, E25.134661	I-type	Hb-Bt-Fsp-Qz-Ap-Sph
TLTN34	Deformed Monzogranite	Tinos	N37.582732, E25.175706	I-type	Hb-Fsp-Qz-Kfs-Bt-Sph-Ap
TLTN36	Undeformed Monzogranite	Tinos	N37.596171, E25.197489	I-type	Hb-Fsp-Qz-Kfs-Bt-Sph-Ap
TLT13	Aplite Vein	Tinos	N37.583181, E25.20910	I-type	Fsp-Hb-Qz
TLTN13 and TLTN14	Grt-Ms Leucogranite	Tinos	N37.612741, E25.242176	S-type	Grt-Ms-Fsp-Qz
TLTN15	Grt-Ms Leucogranite	Tinos	N37.613210, E25.244438	S-type	Grt-Ms-Fsp-Qz
17TL100	Cross-cutting Leucogranite	Tinos	N37.610512, E25.236602	I-type	Bt-Fsp-Kfs-Qz
17TL95	Delos Bt-Tur Leucogranite	Delos	N37.406523, E25.266933	S-type	Bt-Tur-Fsp-Qz-Kfs

TL57	Orthogneiss Basement	Naxos	N37.06696 E25.44710	Basement I-type	Bt-Fsp-Kfs-Qz-Sill-Ilm-Hb
TL58	Grt-Bt Leucogranite dyke	Naxos	N37.118726 E25.527931	S-type	Grt-Bt-Fsp-Qz-Kfs
TL63 and TL64	Grt-Tur-Ms Leucogranite	Naxos	N37.094362, E25.443100	S-type	Grt-Turm-Ms-Fsp-Qz-Kfs
TL69	Grt-Tur-Ms Leucogranite	Naxos	N37.13789 E25.46937	S-type	Grt-Turm-Ms-Fsp-Qz-Kfs
TL72	Deformed Grt-Tur Leucogranite	Naxos	N37.183593, E25.506738	S-type	Grt-Tur-Bt-Fsp-Kfs-Qz
TLN8	Bt-Tur Leucogranite	Naxos	N37.106069, E25.482802	S-type	Bt-Tur-Ms-Fsp-Qz-Ca
TLN10	Bt-Ms Leucogranite in core high strain zone	Naxos	N37.106169, E25.482779	S-type	Bt-Ms-Fsp-Kfs-Qz
TLN37	Bt-Tur Leucogranite	Naxos	N37.18367, E25.50667	S-type	Bt-Tur-Ms-Fsp-Qz
17TL106	Aplite within Granodiorite	Naxos	N37.074694, E25.399604	I-type	Bt-Fsp-Qz

Description	Deformation/ Cross-Cuting Relationships
Partially recrystallized dyke intruding Upper Unit NE of Kolimpithra.	Cross-cuts top-to-NE foliation associated with TSZ, but is internally recrystallized suggesting intuded syn-tectonic with respect to TSZ.
Undeformed dyke intruding gabbros and periodotites of the Tsiknias Ophiolite on the eastern Mt Tsiknias. Fine grained groundmass with subangular to rounded plagioclase phenocysts and little quartz.	Coarse grained, undeformed, intrudes thought TSZ into the Tsiknias Ophiolite Moho Transition Zone.
Slightly more evolved and undeformed dacite dyke with more plagioclase in the groundmass, approximately 10 m wide.	Coarse granied and undeformed, cross cuts blueschist facies top-to-SW shear fabrics (Kionnia Thrust). Strikes ~360 dipping ~30° East.
Deformed south margin of the Tinos I-type granite pluton, at road cutting, hornblende defines lineation plunging ~040/10.	Deformed southern margin of pluton, affected by top-to-NE shear and NE plunging lineation 10° assumed related to TSZ
Undeformed Monzogranite granite within the interior of the pluton, coarsely crystalline.	Undeformed, magmatic fabrics and coarse grained. Cross-cuts TSZ Post dates to-to-NE shearing.
Leucocratic aplite vein ~3 cm wide intruding into Mirsini Unit (sub ophiolitic sole pelagic rocks), with dominantly plagioclase and quartz and minor hornblende.	Cross-cuts TSZ to intrude into the Mirsini unit in the Upper Unit.
Fine grained leucogranite sill, dominantly plagioclase with garnet up to 1-2 mm in diameter and fine grained muscovite approximately 2 m wide intruding amphibolites from Tsiknias metamorphic sole at Livada Bay and cross-cut by high angle normal faults.	1-2 m offset of leucogranite sills by brittle high angle domino-style normal faults. Sills pre-date normal faulting above Livada Detachment.
Another garnet-muscovite leucogranite sill further along the same outcrop at Livada Bay with almost identical composition to TLTN13 but appears to rotate slightly into alignment with normal faults.	1-2 m offset of leucogranite with normal fault, but partially rotates into alignment with the fault, suggestng faulting immediately post-dates intrusion. Normal faults cross cutting strike ~330 dipping ~60 ° to ENE..
Biotite leucogranite vein swarm approximately 2-10 cm wide, striking ~109 ° and orientated subvertical on the eastern margin of Tinos I-type pluton at Livada Beach.	Cross-cuts and intrudes through Tinos Monzogranite. Post-dates shearing on TSZ.
Leucogranite sill, within biotite- sillimanite gneisses in north west Delos. Sill aligned subparallel to foliation, and possible evidence for magma mixing with an adjacent I-type Hb-Bt intrusion.	Overall the sill is aligned subparallel to gneissic foliation but cross-cuts the sillimanite grade fabrics in places. No evidence for necking or boudinage, but is crosscut by a later I-type intrusion, which cross-cuts the gneissic fabrics.

Banded biotite gneiss, including k-feldspar, plagioclase, quartz, minor sillimanite, ilmenite.	Deformed with top-to-NNE sillimanite grade shear fabrics associated with KSZ, grain boundary migration in quartz suggesting deformation temperatures >600 °C.
Undeformed leucogranite on eastern side of migmatite dome, cross-cutting top-to-NNE fabrics associated with KSZ.	Undeformed and cross-cuts KSZ top-to-NNE shearing. Orientated dipping west into migmatite dome. Post tectonic with respect to KSZ but pre-tectonic with respect to migmatite doming.
Steeply dipping branching leucogranite dyke~ ~3 m wide with branching 1-2 m dykes cross-cutting steep metamorphic foliation.	Post-tectonic with respect to KSZ and cross-cuts top-to-NNE shear fabrics. Mild post crystallization solid state deformation affecting quartz, General dyke geometry however subparallel to the NPDS metamorphic foliation striking ~190°/80° to west. Syntectonic with respect to NPDS.
Deformed leucogranite, aligned with steep fabrics dipping ~50 ° to west associated with NPDS.	Deformed with NPDS deformation fabrics and top-to-NNE shear. Dips ~50 ° to west on the western margin of the migmatite, pretectonic with respect to NPDS, syn-tectonic with respect to KSZ.
Deformed and boudinaged leucogranite sill in NPDS shear zone, aligned with NPDS shear fabrics and adjacent with sheared serpentitized peridotite lense.	Sheared and boudinaged leucogranite, aligned sub-parellel to NPDS foliation.The solid state deformation suggests it intruded prior to top-to-NNE shearing and steep doming on the NPDS.
Horizontally boudinaged leucogranite dyke within calcite marbles in the core-high-strain zone at the center of the Naxos migmatite dome.	Horizontally boudinaged vertical dyke striking 010° suggesting post crystallization σ3 orientated NNE-SSW. Tremolite and diopside marbles deform around the boudinaged pieces, suggesting NNE-SSW extensional deformation occurred at >600 °C. Amphibolite layers within marble also affected by brittle domino type NNE-SSW boundinage.
Vertically boudinaged Leucogranite dyke within the core high strain zone at the center of the Naxos migmatite dome. The dyke intrudes calcite marbles.	Vertical leucogranite dyke trends 010° affected by vertical boudinage and recrystallization, with necking implying it was deformed during crystallization. Suggesting σ3 was orientated vertically during intrusion.
Vertically orientated leucogranite dyke intruding KSZ amphibolites in NW Naxos.	Leucogranite dyke cross-cutting KSZ top-to-NE shear fabric, trending 190° dipping 72° to the west
Folded leucocratic aplite, dominantly plagioclase and qurtz with minor biotite ~50 cm wide within the west Naxos Granodiorite pluton within 600 m of the eastern margin of the pluton, in the village of Glinado to the east of the main road entering the village.	Uprightly folded aplite with host granodirite in an open synform. The fold axes strikes ~170°, dipping sub vertically. Unaffected by top-to-NNE shear associated with NPDS.

Table 2: Summary of Granitoid U-Pb and Sr-Nd Isotope Results

Sample Name	Rock Type	Island	GPS Location	Granitoid Classification	U-Pb Age (Ma)	87Sr/86Sr (t)	143Nd/144Nd (t)	εNd (t)
TLT64	Dacite Dyke	Tinos	N37.628196, E25.164215	I-type	14.65 ± 0.29 Ma MSWD = 1.7	0.70966	0.512278	-6.5
17TL36	Dacite Dyke	Tinos	N37.580526, E25.23496	I-type	14.51 ± 0.29 Ma MSWD = 2.0	0.70956	0.512274	-6.6
17TL05	Dacite Dyke	Tinos	N37.553558, E25.134661	I-type	14.38 ± 0.24 Ma MSWD = 1.0	0.71078	0.512198	-8.1
TLTN34	Deformed Monzogranite	Tinos	N37.582732, E25.175706	I-type	14.83 ± 0.25 Ma MSWD = 1.2	0.71136	0.512203	-8.0
TLTN36	Undeformed Monzogranite	Tinos	N37.596171, E25.197489	I-type	14.24± 0.28 Ma MSWD = 1.4	0.71136	0.512202	-8.0
TLT13	Aplite Vein	Tinos	N37.583181, E25.20910	I-type	14.32 ± 0.27 Ma MSWD = 1.8	-	-	-
TLTN13	Grt-Ms Leucogranite	Tinos	N37.612741, E25.242176	S-type	14.75 ± 0.33 Ma MSWD = 3.4	0.71692	0.512324	-5.6
TLTN15	Grt-Ms Leucogranite	Tinos	N37.613210, E25.244438	S-type	14.23 ± 0.92 Ma MSWD = 1.6	0.70621	0.512321	-5.7

17TL100	Cross-cutting leucogranite	Tinos	N37.610512, E25.236602	I-type	14.33 ± 0.13 Ma MSWD = 0.89	0.71147	0.512238	-7.3
17TL95	Delos Bt-Tur Leucogranite	Delos	N37.406523, E25.266933	S-type	13.84 ± 0.22 Ma, MSWD = 0.90 12.07 ± 0.18 Ma, MSWD = 0.33	0.71096	0.512136	-9.3
TL57	Orthogneiss Basement	Naxos	N37.06696 E25.44710	Basement I-type	16.8 -17.0 ± 0.7 Ma, N = 2	-	-	-
TL58	Grt-Bt Leucogranite dyke	Naxos	N37.118726 E25.527931	S-type	13.1 ± 0.3 Ma, N = 3	0.72593	0.512119	-9.6
TL63	Grt-Tur-Ms Leucogranite	Naxos	N37.094362, E25.443100	S-type	13.2 ± 0.5 Ma, N = 1	0.73180	0.512263	-6.8
TL69	Grt-Tur-Ms Leucogranite	Naxos	N37.13789 E25.46937	S-type	Inherited ages	-	-	-
TL72	Deformed Grt-Tur Leucogranite	Naxos	N37.183593, E25.506738	S-type	12.7 ± 0.8 Ma, N = 1	0.72390	0.512259	-6.9

TLTN8	Bt-Tur Leucogranite	Naxos	N37.106069, E25.482802	S-type	14.4 ± 0.2 Ma, N = 2	0.71049	0.512141	-9.2
TLTN10	Bt-Ms Leucogranite in core high strain zone	Naxos	N37.106169, E25.482779	S-type	13.3 ± 0.3 Ma, N = 3	-	-	-
17TL106	Aplite within Granodiorite	Naxos	N37.074694, E25.399604	I-type	14.82 ± 0.17 Ma, MSWD = 1.19	0.71096	0.512204	-8.0

Model Age (Ma) (147Sm/143Nd=0.09)	Interpretation
1061	Syntectonic with respect to TSZ, pre-dates island scale doming at 14.6 Ma, derived from same source as Tinos monzogranite pluton.
1066	Post-tectonic with respet to TSZ at 14.5 Ma, pre-dates island scale doming, derived from same source as Tinos monzogranite pluton.
1160	Pre-dates island scale doming (post 14.4 Ma), derived from same source as Tinos monzogranite pluton.
1153	Syntectonic with respect to TSZ, first phase of intrusion of Tinos monzogranite at 14.8 Ma, same spurce as dacite dykes.
1156	Post-tectonic with respect to TSZ at 14.2 Ma, same source as the dacite dykes.
-	Post-tectonic with respect to TSZ at 14.3 Ma, derived from same source as Tinos monzogranite pluton.
1017.8	Pre-tectonic with respect to domino normal faulting above the Livada Detachment at 14.8 Ma. Constrains upper crust extension to younger than 14.8 Ma. Derived from basement metasediment.
990.4	Pre/syn-tectonic with respect to domino normal faulting above the Livada Detachment at 14.2 Ma. Constrains upper crust extension to younger than 14.2 Ma. Derived from baement metasediment

1103.8	Post-tectonic with respect to TSZ and post-dates Tinos monzogranite pluton. TSZ must be older than 14.3 Ma. Derived from basement metasediment melting.
1237.1	Syn-tectonic with respect to shearing, anatexis and deformation/ metamorphism on Delos.Derived from Bt paragneiss basement. Bimodal U-Pb ages suggest some 2 pulses of magmatism with early S-type magmatism at 13.8 Ma and later I-type mixing at 12.1 Ma.
-	Variscan basement, affected by top-to-NNE shearing on KSZ. Sillimate grade conditions and anatexis at ca. 16 Ma coeval with KSZ shearing.
1236	Post-tectonic with respect to KSZ top-to-NNE shearing, constrains shearing KSZ to older than 13.1 Ma. Sourced from metapelite in migmatite.
1080	Post tectonic with respect to KSZ and Syntectoectic with respect to NPDS, constrains KSZ to be older than 13.2 Ma, but shearing on NPDS must have commenced around 13.2 Ma.
-	Dyke deformed with NPDS but intrusion predates shearing. No useful age constraints, but sourced from metapelite in migmatite dome.
1073	Pre-tectonic with respect to top-to-NNE shearing on NPDS, but post dates KSZ as intrudes to structurally high levels. Constrains NPDS shearing to younger than 12.7 Ma

1242	Vertical dyke intrudes at ca. 14.4 Ma and is pre-tectonic with respect to NNE-SSW extension, (i.e ductile NNE-SSW extension is younger than 14.4 Ma). Melt derived from adjacent metasedimentay migmatites and some marble to explain carbonate.
-	Intrudes syn-tectonic to horizontal constrction and vertical stretching at ca. 13.3 Ma, derived from metasedimentary migmatites and some marble.
1151	An enclave of an earlier leucogranite from adjacent metamorphic core complex within the Naxos Granodiorite. 14.8 Ma age pre-dates the Naxos Granodiorite (12.2 Ma) but constrains timing of E-W shortening to post-14.8 Ma.